UNIVERSIDADE
BEIRA INTERIOR

Thermal properties of electrical arc furnace slag based materials obtained by accelerated carbonation

.

Luciana Sucupira Cristino

Tese para obtenção do Grau de Doutor em
Engenharia Civil
(3º ciclo de estudos)

Orientador: Prof. Doutor João Paulo Castro Gomes

October de 2024

Thermal properties of electrical arc furnace slag based materials obtained by accelerated carbonation.

Luciana Sucupira Cristino

Tese para obtenção do Grau de Doutor em
Engenharia Civil
(3º ciclo de estudos)

Orientador: Prof. Doutor João Paulo de Castro Gomes

Provas públicas realizadas a 10 de setembro de 2024

Júri:

Presidente:

Professor Doutor Joaquim Mateus Paulo Serra

Vogais:

Prof. Doutor Jorge Tiago Queirós da Silva Pinto

Doutor Emiliano Borri

Doutor Naim Sedira

Prof. Doutor João Carlos Gonçalves Lanzinha

Prof. Doutor João Paulo de Castro Gomes

October de 2024

Declaração de Integridade

Eu, Luciana Sucupira Cristino, que abaixo assino, estudante com o número de inscrição D2647 de Engenharia civil da Faculdade de Engenharias, declaro ter desenvolvido o presente trabalho e elaborado o presente texto em total consonância com o **Código de Integridades da Universidade da Beira Interior**.

Mais concretamente afirmo não ter incorrido em qualquer das variedades de Fraude Académica, e que aqui declaro conhecer, que em particular atendi à exigida referenciação de frases, extratos, imagens e outras formas de trabalho intelectual, e assumindo assim na íntegra as responsabilidades da autoria.

Universidade da Beira Interior, Covilhã 21 /03 /2024

(assinatura conforme Cartão de Cidadão ou preferencialmente
assinatura digital no documento original se naquele mesmo formato)

Dedication

I dedicate my thesis to my parents, Lúcia Maria Sucupira Cristino and Francisco Rogério Cristino, as without them I would not have been able to complete my doctorate.

Acknowledgment

To my supervisor, Professor João Castro Gomes, for his guidance and support, always dedicated to helping me achieve the best possible work, constantly contributing ideas and various solutions to enhance the research.
To my parents, Lúcia Maria Sucupira Cristino, Francisco Rogério Cristino, and Eliene Leocardio, for these 10 years of support and encouragement in my studies.
To my husband, Walber Lins, for all his support and partnership throughout these years of study.
To my friends, Giselle Pinto, Amanda Marques, Mariana Teixeira, Letícia Amora, Ana Patrícia Souza, Olivia Duarte, Letícia Lenz, Fernanda Veiga, and Marina Rolim, for supporting me and listening to me when I needed it.
To my friends in Portugal, Keila Veneroso, Paulo Julio, Lorena Cutelo, Bernardo Rainha, Ariana Rainha, Tatiana Rainha, Miguel Vaz, Ruben Nascimento, Manuel Conceição, Ana Mateus, Joana Mota, Alexandra Noite, and Cris Ribeiro, for supporting me during my stay in Portugal.

Abstract

Reducing dependence on fossil fuels and harnessing renewable energy are imperative to facing the current climate emergency and mitigating problems related to pollutants. This thesis focuses on the analysis of the microstructure and thermal properties of mortars manufactured with 100% electric arc furnace slag (EAF-slag) for passive solar energy capture, aiming to contribute to sustainable energy solutions.

The first phase involved a comprehensive review of recent civil engineering research on solar thermal energy storage, highlighting the potential of energy harvesting devices. In addition, it delved deeper into the investigation of accelerated carbonation materials used both in research environments and in the construction sector.

The subsequent step evaluated the thermal capacity of the EAF-slag through differential scanning calorimetry (DSC). The results indicated that the EAF-slag binders exhibited consistent and minimal changes in heat flux responses at various temperature rates, contrasting with the irregular and more significant variations observed in the Portland cement-based binders. The DSC results emphasized the potential of EAF-slag in developing materials with thermal properties.

The third stage analyzed the thermal properties, microstructure and compressive strength of 100% EAF-slag mortars, with and without biochar. The incorporation of biochar led to a reduction in the thermal conductivity of the specimens. However, all EAF-slag specimens obtained results that surpass conventional Portland cement specimens in thermal conductivity. EAF-slag mortars demonstrated favorable thermal properties in all tests carried out. The thermal expansion of EAF-slag mortars was slightly more than twice that of Portland cement (PC) mortars. The EAF-slag mortar sample maintained a higher temperature than the PC mortar sample.

The material with particle size composition ranging from 1 mm to 2 mm and 100% EAF slag without biochar showed the most promising results of all tests of passive solar energy utilization in the construction industry.

These findings highlight a potential for 100% EAF-slag materials in passive solar thermal applications. Their superior thermal conductivity, substantial thermal capacitance, gradual heat absorption and heat release characteristics, and resilience to

the effects of thermal energy position them as materials that perform well in maintaining mechanical stability even under extreme summer conditions.

This research highlights the feasibility of 100% EAF-slag carbonated materials for construction, offering a sustainable solution that mitigates the environmental impacts associated with waste and conventional passive solar thermal energy storage.

This study represents an advancement toward innovative and sustainable practices in civil engineering and construction. The analyzed material can be applied to facades, roofs, and pavements in areas with high solar exposure and elevated temperatures.

Keywords

Thermal properties; microstructure, EAF-slag; carboneted materials; passive solar energy; construction industry.

Resumo

Reduzir a dependência de combustíveis fósseis e aproveitar a energia renovável é imperativo para enfrentar a atual emergência climática e mitigar problemas relacionados à poluição. Esta tese foca na análise da microestrutura e propriedades térmicas de argamassas fabricadas com 100% de escória de forno elétrico a arco (EAF-slag) para captura passiva de energia solar, com o objetivo de contribuir para soluções energéticas sustentáveis.

A primeira fase envolveu uma revisão abrangente da pesquisa recente em engenharia civil sobre geração de energia solar e térmica, destacando o potencial dos dispositivos de colheita de energia. Além disso, aprofundou-se na investigação de materiais de carbonatação acelerada usados tanto em ambientes de pesquisa quanto no setor da construção.

O próximo passo avaliou a capacidade térmica da escória EAF através de calorimetria diferencial de varredura (DSC). Os resultados indicaram que os ligantes de escória EAF apresentaram mudanças consistentes e mínimas nas respostas de fluxo de calor em diferentes taxas de temperatura, contrastando com as variações irregulares e mais significativas observadas nos ligantes à base de cimento Portland. Os resultados do DSC enfatizaram o potencial da escória EAF no desenvolvimento de materiais com propriedades térmicas.

A terceira etapa analisou as propriedades térmicas, microestrutura e resistência à compressão de argamassas de 100% de escória EAF, com e sem biocarvão. A incorporação de biocarvão levou a uma redução na condutividade térmica das amostras. No entanto, todas as amostras de escória EAF obtiveram resultados que superaram as amostras de cimento Portland convencionais em condutividade térmica. As argamassas de escória EAF demonstraram propriedades térmicas favoráveis em todos os testes realizados. A expansão térmica das argamassas de escória EAF foi ligeiramente mais do que o dobro das argamassas de cimento Portland (CP). A amostra de argamassa de escória EAF manteve uma temperatura mais alta do que a amostra de argamassa de CP.

A amostra com composição de tamanho de partícula variando de 1 mm a 2 mm e 100% de escória EAF sem biocarvão mostrou os resultados mais promissores de todos os testes de utilização de energia solar passiva na indústria da construção.

Essas descobertas destacam um potencial para materiais de 100% de escória EAF em aplicações térmicas solares passivos. Sua condutividade térmica superior, capacidade térmica substancial, características de absorção de calor gradual e liberação de calor, e resistência aos efeitos da energia térmica os posicionam como materiais que se saem bem na manutenção da estabilidade mecânica mesmo sob condições extremas de verão.

Esta pesquisa destaca a viabilidade de materiais carbonatados 100% a partir de escória de forno a arco elétrico (EAF) para construção, oferecendo uma solução sustentável que mitiga os impactos ambientais associados aos resíduos e ao armazenamento de energia térmica solar passiva convencional.

Este estudo representa um avanço em direção a práticas inovadoras e sustentáveis na engenharia civil e construção. O material analisado pode ser aplicado em fachadas, telhados e pavimentos em áreas com alta exposição solar e temperaturas elevadas. Este estudo é um passo importante em direção a práticas inovadoras e sustentáveis na engenharia civil e construção.

Palavras-chaves

Propriedades térmicas; microestrutura; EAF-escória; materiais carbonatados ;energia solar passiva; indústria da construção.

Resumo Alargado

Atualmente, estamos vivendo uma importante transição no setor de geração de energia, com a crescente adoção de fontes de energia limpa. A energia solar, por exemplo, tem se tornado cada vez mais comum na construção civil, sendo incorporada em fachadas, pavimentos e coberturas.

Em resposta às preocupações ambientais, tem-se buscado alternativas ao uso do cimento Portland, com o intuito de desenvolver novos materiais que contribuam para o armazenamento de energia solar térmica. Uma dessas alternativas envolve a produção de materiais cimentícios à base de resíduos, com propriedades térmicas elevadas e capacidade de armazenar CO_2 por meio da mineralização. Entre essas opções, destaca-se a escória de forno elétrico a arco (EAF-slag), que apresenta características relevantes para esse fim, como sua coloração escura e o alto teor de elementos metálicos, em especial o óxido de ferro, que contribuem para suas propriedades térmicas aprimoradas.

Esse tipo de cimento alternativo ao Portland tem o potencial de reduzir significativamente a pegada de carbono na indústria da construção, além de ser aplicado em fachadas, coberturas e pavimentos para otimizar a captação e armazenamento de energia solar passiva. Embora existam muitas pesquisas sobre métodos de armazenamento de energia solar passiva em edificações, o estudo do uso de resíduos com esse propósito ainda é bastante limitado.

O objetivo geral desta pesquisa é desenvolver um material 100% reciclado e carbonatado, inovador, com elevadas propriedades térmicas, visando melhorar o desempenho na captação de energia solar passiva. Busca-se integrar preocupações de sustentabilidade, baseando-se na reutilização de resíduos para minimizar tanto a energia incorporada quanto as emissões de CO_2.

Os objetivos específicos da pesquisa incluíram os seguintes aspetos:

-Investigar e sistematizar a reutilização de resíduos com potencial para o desenvolvimento de materiais sustentáveis, com propriedades térmicas aprimoradas;

-Explorar métodos e tecnologias já existentes para reutilizar materiais residuais no desenvolvimento de materiais sustentáveis com características térmicas desejáveis;

-Revisar a literatura e as pesquisas em andamento sobre metodologias de medição e caracterização de propriedades térmicas de materiais;

-Avaliar as vantagens e as aplicações potenciais de materiais com propriedades térmicas melhoradas;

-Utilizar técnicas para identificar e quantificar a composição química dos resíduos;

-Analisar o impacto de diferentes tamanhos ou dimensões de agregados nas propriedades térmicas dos materiais desenvolvidos;

-Estudar as propriedades térmicas de misturas que utilizem 100% de escória de forno elétrico a arco.

A metodologia deste estudo foi dividida em três fases. A primeira fase consistiu em uma revisão de literatura sobre o uso de coletores de energia solar na construção civil, com foco especial na energia solar passiva.

Essa revisão incluiu o estudo de diversos métodos de armazenamento de energia solar, como células fotovoltaicas, piroeletricidade, geradores termoelétricos e materiais térmicos. Foram identificadas várias vantagens do uso de materiais térmicos no armazenamento de energia solar passiva. Além disso, foi realizada uma análise das empresas que utilizam carbonatação acelerada na fabricação de materiais de construção civil. A pesquisa revelou que vários países estão investindo em materiais produzidos por carbonatação acelerada para aplicação na indústria da construção.

Na segunda fase, foi conduzido um estudo preliminar das propriedades térmicas do pó de escória de forno elétrico a arco (EAF) e de sua composição química. O principal ensaio realizado foi a Calorimetria Diferencial de Varredura (DSC), que permitiu avaliar o comportamento térmico do material.

Nesta fase, foram realizadas cinco amostras diferentes de ligante, utilizando cimento Portland e escória de alto forno. Três dessas amostras, contendo cimento Portland, foram submetidas à cura por hidratação, enquanto as outras duas, com escória EAF, passaram pelo processo de carbonatação acelerada.

O processo de carbonatação acelerada foi conduzido no laboratório da Universidade da Beira Interior (UBI), seguindo o seguinte esquema: mistura, compactação estática e

câmara de carbonatação. As amostras permaneceram na câmara de carbonatação por 24 horas, durante as quais ocorreu a absorção de CO2 pelas amostras.

Após o processo de cura, o material foi fragmentado em partículas menores que 63 micrômetros. O ensaio térmico envolveu três diferentes taxas de aquecimento: 2°C/min, 4°C/min e 6°C/min. O procedimento foi dividido em três etapas:

-Um período isotérmico inicial a 5°C, mantido por 5 minutos;

-Aquecimento dinâmico até 40°C, nas taxas de aquecimento especificadas;

-Estabilização térmica a 40°C, mantida por 5 minutos.

Esse protocolo permitiu uma análise detalhada das propriedades térmicas e da reação à carbonatação acelerada, facilitando a compreensão do comportamento do material sob diferentes condições de aquecimento.

A terceira fase do estudo focou na investigação das propriedades térmicas de argamassas confeccionadas com escória de forno elétrico a arco (EAF). Foram realizados ensaios com argamassas contendo diferentes granulometrias: (0,5 a 1 mm), (1 a 2 mm) e (2 a 4 mm). Os materiais utilizados nesta fase incluíram escória, agregado de escória, areia de rio e Biochar.

Os seguintes ensaios foram realizados na 3ª fase: resistência à compressão, análise termogravimétrica (TGA), porosimetria por intrusão de mercúrio (MIP), condutividade térmica, análise de transmitância térmica, capacidade de armazenamento de calor e dinâmica- utilizando o equipamento Test Box, expansão térmica e armazenamento de calor.

Esses ensaios forneceram uma compreensão detalhada das propriedades térmicas das argamassas, avaliando a sua viabilidade como material de construção, especialmente no que se refere à eficiência energética e sustentabilidade.

Os ensaios de condutividade térmica e a análise com o equipamento Test Box foram realizados na Universidade de Lleida, em Espanha. O Test Box foi desenvolvido por essa instituição para analisar o comportamento térmico de materiais.

O analisador térmico, conhecido como Test Box, aquece ou resfria as amostras utilizando um sistema de banho-maria conectado a cada compartimento. Dois sensores de temperatura e um sensor de fluxo de calor são posicionados próximos às superfícies

da amostra. Dependendo do perfil de temperatura aplicado a cada banho de água, a amostra pode ser submetida a um gradiente de temperatura constante, aquecida em ambas as superfícies ou submetida a variações de temperatura em apenas um lado.

Esse dispositivo permite calcular a transmitância térmica, a capacidade térmica específica e analisar a resposta térmica dinâmica da amostra, proporcionando uma análise detalhada do comportamento térmico do material em condições variáveis

Os resultados do estudo preliminar indicam que a amostra CE apresentou uma variação estável e menos pronunciada no fluxo de calor, com poucos picos endotérmicos e exotérmicos, sugerindo maior estabilidade térmica em comparação com as outras amostras. A amostra CEC exibiu variações mais acentuadas, com um número maior de picos endotérmicos e exotérmicos do que o espécime CE. Já as amostras HCE e HC12 mostraram variações ainda mais intensas, com mais picos endotérmicos e exotérmicos, enquanto a amostra HC15 apresentou um pico exotérmico elevado. A maior variação observada nas amostras com cimento Portland é provavelmente atribuída à sua composição.

Nos ensaios de resistência à compressão, foi constatado que as amostras com granulometria intermediária (1 a 2 mm) apresentaram a maior resistência à compressão. Em especial, as amostras compostas por 100% de escória com granulometria de 1 a 2 mm demonstraram um desempenho superior. A adição de Biochar não resultou em uma diferença significativa na resistência à compressão dessas amostras.

Os resultados do TGA indicaram que as amostras 100% escória com Biochar apresentaram a maior absorção de CO_2, com destaque para as granulometrias de 2 a 4 mm e 1 a 2 mm. No entanto, a adição de Biochar não aumentou significativamente a absorção de CO_2. Em geral, todas as amostras 100% escória demonstraram boa capacidade de absorção de CO_2 em diferentes granulometrias.

Os resultados da análise da microestrutura mostraram que a maior porosidade, de 33,18%, foi encontrada na amostra 4A, composta por 100% escória e Biochar com a menor granulometria. Por outro lado, a menor porosidade, de 16,09%, foi registrada na amostra 2B, feita de escória, areia de rio e Biochar com maior granulometria. Esses resultados sugerem que a porosidade não está diretamente relacionada à granulometria do agregado, mas sim que a maior granulometria favoreceu a entrada de CO_2 no processo de carbonatação acelerada.

Os resultados da condutividade térmica estão de acordo com os dados de porosidade: quanto maior a porosidade, menor a condutividade térmica. As amostras com granulometria B apresentaram a menor porosidade e a maior condutividade térmica, enquanto as amostras com menor granulometria (A) mostraram maior porosidade e menor condutividade térmica. Estudos anteriores indicam que a adição de Biochar reduz a condutividade térmica, o que foi confirmado pelas nossas análises.

De forma semelhante à condutividade térmica, as amostras com maior granulometria (B) exibiram os valores mais elevados de transmitância térmica. A amostra 1B, composta por escória e areia de rio com maior granulometria, apresentou um valor de transmitância térmica de 30,14 W/m²K. No entanto, todas as amostras mostraram transmitância térmica adequada para aplicações em geração de energia solar passiva.

A análise com o Test Box revelou que a amostra com maior capacidade térmica foi a 4C, composta por 100% de escória EAF, Biochar e granulometria de 1 a 2 mm. Esta amostra mostrou uma maior capacidade de absorver calor em comparação com as outras, embora todos os corpos de prova tenham apresentado valores similares.

O ensaio de atraso térmico indicou que a amostra 3C teve o maior tempo de atraso térmico, absorvendo e liberando calor mais lentamente. Por outro lado, a amostra 1A apresentou o menor tempo de atraso térmico. O atraso térmico mede o tempo necessário para a onda de calor atravessar o material, o que é essencial para avaliar o desempenho em condições extremas de temperatura.

As amostras 1B e 2B apresentaram o maior coeficiente de estabilidade térmica, enquanto a amostra 4A teve o menor coeficiente. A estabilidade térmica inferior a 1,0 é importante para a geração de energia, pois indica uma maior capacidade de manter as propriedades mecânicas sob variação de temperatura.

Os resultados do ensaio de expansão térmica mostraram que as argamassas feitas com escória EAF têm uma expansão térmica significativamente maior do que as argamassas de cimento Portland, chegando a mais do que o dobro da expansão observada nas argamassas de cimento Portland. O coeficiente de expansão térmica foi consistentemente maior para as amostras de escória.

As amostras 100% escória apresentaram temperaturas mais elevadas ao longo do ensaio de armazenamento de calor. A temperatura da amostra 100% escória, ao ser retirada da estufa, estava próxima a 60°C, valor semelhante ao da própria estufa, indicando que a escória possui uma excelente capacidade de retenção de calor.

Com base em uma análise abrangente dos dados, a amostra com as melhores características para o uso em energia solar passiva na construção civil foi a de granulometria entre 1 mm e 2 mm, composta por 100% de escória EAF sem Biochar (3C). Essa composição apresentou condutividade térmica superior, alta capacitância térmica, característicos graduais de absorção e liberação de calor, além de excelente resiliência mecânica sob condições extremas, como no verão.

Este estudo demonstra a viabilidade de utilizar argamassas 100% recicladas para a construção civil, oferecendo uma solução sustentável e eficiente para o armazenamento de energia solar passiva em pavimentos, fachadas e coberturas

Contents

List of figures

List of tables

List of acronyms

C-MADE - Centre for Materials and Building Technologies

DSC - Differential Scanning Calorimetry (DSC)

EAF slag - Electric Arc Furnace Slag

EDX - Energy Dispersive X-ray Spectroscopy

HR - Relative Humidity

MIC - Micrometers

MIP - Mercury Intrusion Porosimetry

PC - Portland Cement

RCD - Construction and Demolition Waste

SEM - Scanning Electron Microscopy (SEM)

TGA - Thermogravimetric Analysis

UBI - University of Beira Interior

List of chemical compounds

Al - Aluminum

Al_2O_3 - Aluminum Oxide

Ca - Calcium

$CaCO_3$ - Calcite Calcination

CaO - Calcium Oxide

$Ca(OH)_2$ - Calcium Hydroxide

CO_2 - Carbon Dioxide

Fe - Iron

Fe2O3 - Iron Oxide

H2O - Water

K - Potassium

K2O - Potassium Oxide

Mg - Magnesium

MgCO3 - Magnesium Carbonate

MgO - Magnesium Oxide

O - Oxygen

Si - Silicon

SiO2 - Silicon Dioxide

S - Sulfur

SO3 - Sulfur Trioxide

Chapter 1- Introduction

The main focus of this study was to obtain a sustainable cementitious material distinguished by its thermal properties, specifically designed to harness passive solar energy. This study is a direct response to the economic and environmental concerns arising from the overproduction of waste and the environmental impact of traditional passive solar thermal energy storage methods.

Steel slag, a by-product generated on a large scale, often finds limited applications, mainly in road aggregates and railway infrastructure. However, disposing of electric arc furnace (EAF) slag, a subtype of steelmaking slag, in landfills is not only costly, but also results in the immobilization of valuable land resources and poses potential environmental risks.

The research explores the potential of using steel slag as a viable replacement for traditional binders in passive solar energy applications. This investigation involves several fundamental steps: first, grinding the steel slag to a fine consistency; then sieve and separate the finely ground slag; then mix the sifted powder with water and aggregates; followed by molding and compacting the mixture; and finally, subjecting the newly molded specimens to specific curing conditions, carbonation for hardening.

This research shows significant academic importance, as it contributes to the knowledge of thermal properties of EAF-slag materials obtained by carbonation hardening process. It serves as a guide for academia, emphasizing the importance of these properties in sustainable construction practices and their potential impact on passive solar passive solar thermal energy storage.

1.1 Research objectives

This research work aimed to develop carbonated materials with high passive solar energy absorption to increase the yield of solar energy captured. In particular, electric-arc steel furnace slag materials with a high metal content were developed and compared with Portland cement-based materials.

Specifically, it was intended to study the microstructure of cementitious materials obtained with electric arc furnace slag and by-products in the first phase. Their thermal properties in thermal capacitance and thermal conductivity was studied, enhancing them. It was also designed to develop experimental knowledge by analyzing the performance of specimens related to microstructure and thermal properties, particularly their thermal response to solar incidence.

Thus, it was intended to identify the critical parameters of the microstructure of "slag-cement" or "metal-cement" that increase its thermal properties without reducing the mechanical properties, aiming to develop constructive solutions that improve the absorption of passive solar energy in buildings and infrastructure.

It was intended to develop an innovative carbonated material with a high thermal property to conceive a higher passive energy harvesting performance. It was sought that this material integrates sustainability concerns, namely based on the reuse of waste, aiming to minimize embodied energy and CO_2 emissions.

Thus, the specific objectives of the PhD are as follows:

I) Research and systematize the reuse of waste and the potential to develop sustainable materials with thermal properties and characteristics from waste:

- Analyze solutions under development:

Investigate existing methods and technologies used for reusing waste materials to develop sustainable materials with desirable thermal properties.

- Research processing and production methods:

Study various processing and production techniques employed in transforming waste materials into usable sustainable materials, focusing on thermal properties enhancement.

- Research studies on methods for determining thermal properties and the benefits of these systems:

Review literature and ongoing research on methodologies for measuring and characterizing thermal properties of materials. Evaluate the advantages and potential applications of materials with improved thermal properties.

II) Collect, characterize and analyze ways of processing different types of waste:

- Determine the chemical composition by energy dispersive spectrometry (SEM/EDS):

Utilize SEM/EDS techniques to identify and quantify the chemical composition of of the waste (EAF-slag)

- Study different types of aggregate dimensions, analyzing their possible thermal properties:

Investigate how different sizes or dimensions of aggregates affect the thermal properties of resulting materials.

- Analyze the addition of biochar to the mixtures and check if it occurs changes in their microstructure and analyze thermal properties:

Experiment with adding biochar to waste mixtures and evaluate any alterations in microstructure and thermal properties.

- Analyze a 100% EAF-slag mixture:

Examine the thermal properties and characteristics of a mixture containing 100% Electric Arc Furnace (EAF) slag.

III) Study physical (thermal) and mechanical properties of mixtures:

- Analyze the results of thermogravimetric analysis (TGA):

Interpret data obtained from TGA experiments to understand the thermal stability and decomposition behavior of materials.

- Determine the compressive strength of specimens:

Analyze the compressive strength of the specimens formed from waste mixtures to assess its mechanical properties.

- Analyze mercury intrusion porosimetry (MIP):

Utilize MIP to study the pore structure and distribution within the materials, which can influence their thermal and mechanical properties.

- Analysis of thermal expansion:

Investigate how materials derived from waste (EAF-slag) respond to changes in temperature through thermal expansion analysis.

- Analyze thermal conductivity, thermal capacitance, and response to thermal inertia:

Evaluate the thermal conductivity and thermal capacitance of materials and their ability to resist changes in temperature over time.

IV) To write the final document of the thesis:

It was necessary to bring together all the results, analyzes and conclusions of all articles published in this research into a comprehensive document following the guidelines and requirements of a doctoral thesis.

Each of these steps represents a critical aspect of the research process that aims to develop sustainable materials from EAF slag and understand their thermal properties and characteristics.

1.2 Thesis structure

This doctoral thesis was divided into seven distinct chapters that present and discuss:

Chapter 1: Introduction:

- Provide an overview of the study, outlining its objectives and significance in addressing sustainability challenges.
- Justify the relevance of investigating EAF-slag reuse for sustainable material development with enhanced thermal properties.
- Highlight the broader implications of the research within the context of sustainable construction and environmental conservation.

Chapter 2: State of the Art of Solar Energy in Buildings

- Review current literature and advancements in solar energy utilization within building structures.
- Discuss various solar energy technologies, their applications, and integration methods in architectural design.
- Analyze the benefits and challenges associated with implementing solar energy systems in buildings, considering factors such as efficiency, cost, and environmental impact.

Chapter 3: State of the Art of EAF Slag and Accelerated Carbonation

- Explore existing research on electric arc furnace (EAF) slag and its potential for sustainable reuse.
- Analyzes accelerated carbonation techniques and how the chemical reaction occurs in this process.
- It addresses the various research and industries that manufacture construction materials through carbonation processes.

Chapter 4: Experimental Procedure

- Provide a detailed overview of the experimental setup and methodologies employed in the research.
- Describe the specific procedures followed to investigate the thermal properties and characteristics of EAF-slag materials.
- Discuss any challenges encountered during experimentation and how they were addressed

Chapter 5: Materials and Methods

- Characterize the materials used in the study, including waste sources, aggregates, binders, and additives.

- Highlight the experimental conditions, such as mixing ratios, curing processes, and testing protocols.

Chapter 6: Results and Discussion

- Present the findings of the research, including data analysis and interpretation of experimental results.
- Discuss the implications of the findings in relation to the study's objectives and hypotheses.
- Compare and contrast the performance of EAF-slag materials with traditional counterparts, enhancing thermal properties and sustainability aspects.

Chapter 7: Conclusion

- Summarize the key findings and contributions of the research.
- Discuss the implications of the research in advancing sustainable construction practices and waste management strategies.
- Suggest avenues for future research, particularly focusing on further investigations into EAF-slags and their carbonation-induced thermal properties.

1.3 List of Publication

The following publications constitute the core of this thesis, distributed across Chapters 2 to 7.

- Luciana Sucupira and João Castro-Gomes ,(2021). Review of Energy Harvesting for Buildings Based on Solar Energy and Thermal Materials, CivilEng. https://doi.org/10.3390/civileng2040046.

- Luciana Sucupira and João Castro-Gomes ,Preliminary study of heat flow response of electric-arc furnace slag binders aiming generation of passive solar energy in buildings (The document is under review atInternational Journal of Sustainable Engineering)

- Luciana Sucupira and João Castro-Gomes, (2024). Thermal Expansion/Energy Storage Characteristics of EAF-Slag Mortars for Passive Solar Energy. In: Lanzinha, J.C.G., Qualharini, E.L. (eds) Proceedings of CIRMARE 2023. CIRMARE 2023. Lecture Notes in Civil Engineering, vol 444. Springer, Cham.
  https://doi.org/10.1007/978-3-031-48461-2_19

- Luciana Sucupira, Gabriel Zsembinszki, Sara Risco Amigó, João Castro-Gomes and Luisa F. Cabeza. Thermal properties and porosities of 100% electric arc furnace-slag mortars for passive solar energy applications in the construction industry.
  (The document is under review at Case Studies in Construction Materials)

Chapter 2- Review of solar energy and thermal materials

2.1 Preface

This chapter discusses the state of the art of passive solar energy harvesters using the thermal properties of materials, highlighting previous research that has been conducted in the area, highlighting the main results, discoveries and opportunities for future research.

The chapter is based on the publication:

Luciana Sucupira and João Castro-Gomes,(2021). Review of Energy Harvesting for Buildings Based on Solar Energy and Thermal Materials, CivilEng. https://doi.org/10.3390/civileng2040046.

2.2 Introduction

In November 2018, the agreements between the Council of Ministers, the European Parliament, and the European Commission were established in the form of new critical objectives to be followed by the European Union. Compared to 1990 levels, the new targets aim to reduce pollutant gas emissions by at least 40%. Also, there was a greater incentive of at least 32% of renewable energies and an improvement of at least 32.5% in energy efficiency, concerning the 2007 goals. To achieve the proposed plans, collective efforts must be applied to reducing carbon and generating renewable energy, thus decarbonizing the environment [1].

The European Commission also presented the 2030 Energy and Climate Package, through which Member States should develop integrated national plans that address energy advancement and climate improvement. The idea is to contribute to a low carbon economy's progress and develop an energy system that guarantees energy availability to the entire population. The energy transition is based on complete decarbonization with electricity production from renewable sources [2].

Each Member State has a strategy to consolidate this Plan, thus aiming at a more competitive economy. The system developed in Portugal foresees that the potential of the available renewable resources, such as water, wind, biomass, geothermal, and the sun, is used. The main bet is currently solar energy, as it is a solution and a source of energy capable of continuing energy transition [3].

Considering the definition of a smart city, the European Commission has proposals to help design or retrofit buildings to reduce energy bills and the incidence of carbon dioxide (CO_2) and obtain the building's thermal conditioning by using thermal materials. As a result, cities will be energy efficient and oriented towards using cutting-edge technologies to meet the aims of a

smart city, namely, decrease energy consumption, increase the capture of renewable energy and reduce the carbon footprint [4].

There are already several methods to capture energy sustainably. In this document, solar energy and thermal materials will be analyzed. These methods use sunlight and temperature which are non-polluting and daily accessible sources of energy. With the development of cities, which are becoming larger and larger, it is increasingly necessary to obtain solutions for their growth without affecting the environment, for example, using buildings to get energy. The capture of solar energy through photovoltaic and thermal materials is a means of obtaining this energy and has been studied by several researchers worldwide.

2.3 Types of energy harvesting

When analyzing the various articles focused on different harvesting energy methods, it was observed that people are becoming aware of the harm that the incidence of CO_2 brings to the environment. There are currently several types of energy harvesting (electromagnetic, piezoelectric, thermoelectric, solar and pyroelectric) which are applied in various areas of civil engineering. Many of these energy sources use the sun, the earth or chemical compounds. They can also use vehicles or wind loads' mechanical energy to capture renewable energy [13,14].

In recent years, several studies have been carried out proving that energy can be harvested from the sun and high temperatures, thus contributing to value other methods of obtaining energy and improving the urban environment and reducing pollutants' incidence. Considering recent developments in the technology for capturing solar energy, it is essential to identify how each type of model works: thermoelectric generator (TEG), photovoltaic cells, thermoelectric materials, and pyroelectric, Figure 1.

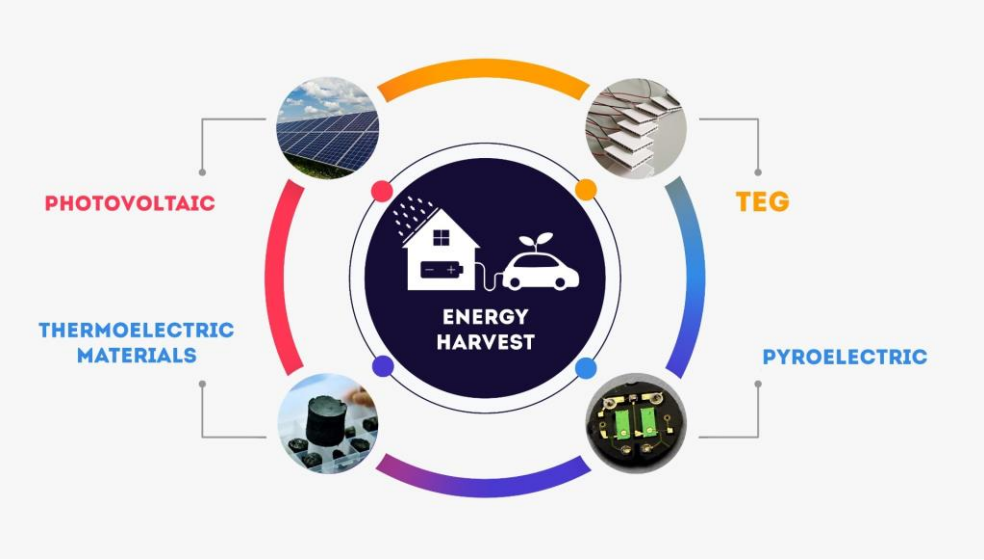

Figure 1: Types of solar energy addressed in this research

TEG works with the electrical voltage performed by two heterogeneous semiconductors joined at one end. This is due to the temperature difference, where the electrons stir and pass to the colder side, thus generating energy. Also, thermoelectric materials use the material's high temperature to obtain energy or thermal comfort in the environment [13–18].

Pyroelectric is a method of obtaining energy that uses the conversion of a small amount of heat to electricity, often using chemical compositions [13]. The photovoltaic cell gets energy through solar radiation on the cells' surface, called the photoelectric effect, absorbing photons and releasing electrons, thus generating electric current [14].

2.4 Uses in civil engineering

2.4.1 Facades

The facades are the part of the buildings that are exposed to a high incidence of sunlight. In this scope, there are several types of research focused on obtaining energy using this high incidence and natural light. Various types of research use smart windows and ceramics that capture energy, as well as the fabrics that are used in curtains or flags to generate energy.

Windows are parts of the building that provide a lot of sunlight. Solar cells in window glass use a bifacial light collection technology, an effective strategy to increase the production of energy using photovoltaic devices. The transparent electrode is essential to determine the efficiency of energy conversion. Bi-tandem carbon quantum dots are used to adapt the transparent CoSe to a bifacial electrode in solar cells sensitized with dye, thus achieving an energy conversion efficiency of 8.54% in the front and an efficiency of 6.55% in the rear in comparison with 7.87% and 5.03% in non-carbon devices [5,17–21].

A new smart blind system uses thin-layer photovoltaic cells attached to the blinds to capture energy. The process occurs because the excess of heat, absorbed by the solar cells, gets dissipated by a coating with porosity at a temperature 9% higher [15]. Moreover, a transparent device has been developed to collect energy from both sides of the material. The material is a synthesis of transparent ternary alloys and economy (CoM) 0.85 Se (M = Ni, Ru, Fe) through a soft solutions method and used as bifacial materials. The efficiency of 9.16%, 8.09%, 7.58% for frontal irradiation and 3.86%, 3.31%, 3.51% for rear irradiation is shown [18].

A smart window device with nanofabricated material which comprises a semitransparent perovskite solar cell and an aperiodic multi-layer nanophotonic coating, with different angles from large to large (0°, 15°, 30°, 45°, and 60°) was also used. Based on the data analyzed, the calculations were performed on EnergyPlus, projecting an annual energy savings of 13% in a 2-story residential building located in Arizona [17].

A new window was also designed using glass in prismatic gratings filled with water to absorb solar radiation to capture energy, Fugure 2. The spectral model has seven bands to investigate solar radiation under various solar conditions and in different locations. The shutter has a dual purpose: energy capture and natural lighting. Using calculations, the device obtained an absorption of 87-88% of the energy of ultraviolet radiation and 81-82% of infrared radiation and transmitting about 76% of visible light. The total efficiency of solar energy absorption reaches 53-56% [10].

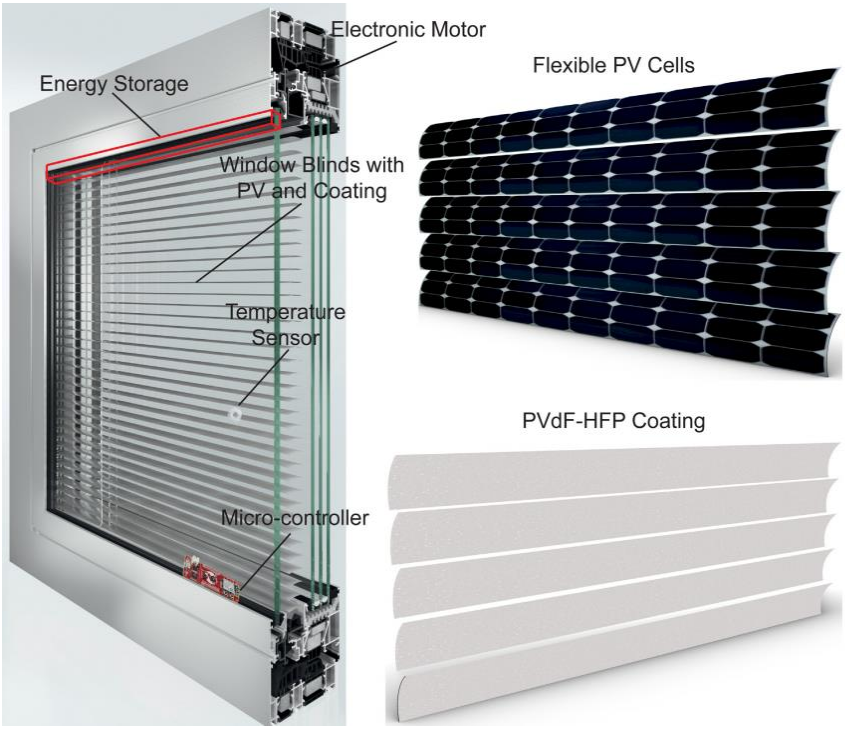

Figure 2: Smart window and louver blades [15].

In an existing 20-story commercial building in Lahore, Pakistan, where the climate is hot and humid, origami-shaped glass facades have been placed and are able to control heat loss and provide access to daylight by continuously adapting to varying weather conditions. The origami shape of this facade allows the plant to intercept additional sunlight and align itself to increase the light received, varying its position according to changing sun angles. The shading devices of the proposed facade fold into horizontal and vertical positions, providing solar shading throughout the day. With the origami shaped glass facade in Pakistan, the existing energy load of the building can be reduced by up to 32% when compared to the previous facade, thus being a great option to decrease the energy costs of the building and to mitigate the CO2 incidence in the passive solar thermal energy storage [23].

The facades produce energy from microalgae that are grown inside glass elements. The building is almost entirely covered with green, shutter-like glass modules where the green microalgae are grown. This facade cannot only be used to produce energy but can also control light and provide

shade. The BIQ House in Hamburg, for example, which contains the world's first "bioreactive" facade known as SolarLeaf, can generate heat, biofuel, and shade, as well as decrease CO2 emissions. It is the first building to have a facade with bioreactors [24,25].

The BIQ facade in Hamburg contains glass slides with algae immersed in water. When the algae reproduce, they emit heat, thus heating the water. This water then runs through the pipes heating environments and the water used in the bathrooms and the kitchen. The algae are removed weekly and then taken to places where they are processed to produce fuels such as methane and hydrogen [24,25].

The Hanwa Group manufactures solar panels and other sustainable technologies. It has built a tall tower facade that provides a greater amount of electricity to the building. The building has not only one of the largest solar photovoltaic facades in the world but also an illuminated LED system that makes an attractive animated display at night. In addition, in Portugal, the Solar XXI building, a low-energy office building, uses active and passive solar strategies that have been applied to reduce energy use [26,27].

A team of researchers from the Fraunhofer Center for Photovoltaic Technology, CSP, in the German city of Halle, together with architects from the Leipzig University of Applied Sciences (HTWK Leipzig, Germany) presented a solar facade in the SOLAR.SHELL project. According to experiments, the photovoltaic elements integrated into this facade provide up to 50 percent more solar energy than modules mounted perpendicularly on building facades. The German researchers analyzed how photovoltaic elements can be best mounted on this type of carbon concrete facade, i.e. how to achieve the best result by combining this innovative concrete with solar energy production [28].

Ceramics is another material used in most of the facades which are highly exposed to the sun. TiO 3-based ceramics (Bi 0.5 Na 0.5) is one of the most attractive pyroelectrics, lead-free, due to its high polarization. The reason for carrying out the high energy harvest is due to the addition of Aluminum Nitride (AlN), which can decrease the matrix conductivity, thus resulting in low resistance to rupture (BDS) that allows the application of high electric fields in the polarization, which varies with temperature change [29].

The elements O, Na, Bl, and Ti are contained equally in all the materials. In contrast, the Al is concentrated in the material's external parts, consistent with the scattering diffraction mapping. The microstructure proved to be dense and compact; when the AlN content increases by 0.25% by weight, the materials become denser with a grain size increase. When increasing the weight of AlN from 0% to 25%, there is an increase in the polarization saturation from 32 μC/cm2 to 41 μC/cm2, as well as an increase in the low breaking strength (BDS) of 160 kV/cm to 260 kV/cm, being beneficial for obtaining a high energy capture performance with a greater electric field. The data observed showed an increase of 0.3% in AlN results with a decrease in BDS, thus obtaining a value of 190 kV/cm; this is due to a reduction in density [15].

The capture of thermal energy with high-performance new models of pyroelectric ceramics has heat transfer and high-temperature variation. This was verified with a hexagonal boron nitride (hBN) pyroelectric ceramic with a 0.1% weight of PMN-POM-PZT with ceramic matrix. To obtain a more. detailed comparison of energy consumption, specimens were made in cylinders with the same dimension 310 μm thick and 8.5 mm in diameter. Also, 0.1% of hBN was derived in one sample, and 0.3% hBN in another sample. The hot and cold flow temperature was monitored simultaneously with two regulated type K thermocouples with fan and heat sink. The heating process took place at a temperature of 600 ºC for 25 minutes [17].

The temperature behavior of the relative permissiveness for each addition increased to 213º C and then decreased with increasing temperature, this temperature being comparable to a transition phase. The actual thermal conductivity (K) occurs with an increase in temperature for each sample. In the sample with the addition of 0.1% hBN by weight, the value of the cyclic temperature changes and the rate of temperature change (dT / dt) increased from 3.19 º C/s to 3.45º C/s, Figure 3. Besides, the 0.1% hBN value showed better results in the saturation and the remaining polarization. Compared to pure ceramic, the 0.1% hBN analysis indicated a 65.6% increase in maximum output power. The ceramic with an addition of 0.1% of hBN by weight has better ferroelectric and pyroelectric properties and better thermal conductivity than ceramic without addition. It shows that the addition can cause a better transfer of heat to capture pyroelectric energy [17].

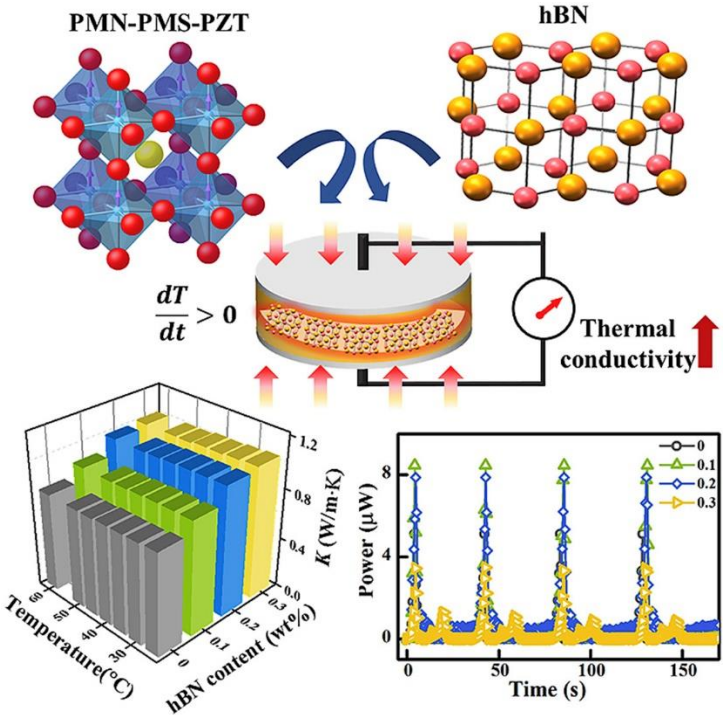

Figure 3: Harvesting of thermal energy using pyroelectric ceramics with the addition of hBN with improved heat transfer [23].

The performance of dielectric absorbers exploiting different coatings consisting of different transparent matrices (SiO 2, AlN, SiC) and metallic inclusions, Cu and Ni, combined with selective filters high-temperature applications which are necessary for solar energy. An analysis of coatings for a temperature range between 400º C and 1000º C, full recipe at an operating temperature of 850º C. The best results are coating with copper nanoparticles in a low index dielectric matrix, SiO2 [18].

In addition to ceramics, paints are ubiquitous on facades and can be a great source of energy. The new paints exposed on the surface are composed of nanocomposite films of lead and magnesium titanate (PMN-PT) to capture pyroelectric and piezoelectric energy. The films were manufactured using the conventional brush painting technique to provide low-cost benefits, thus creating multifunctional films. The increase in the films' dielectric constant occurs with the rise in the percentage of PMN-PT in the material. It was analyzed that the voltage and the power increase with the application of thermal variation [19].

In addition to ceramics and windows, many researchers bet on capturing thermal and solar energy through fabrics, which can be used both in curtains and flags. This material is extremely exposed to the sun. A new device that captures wind and solar energy through inverted flags was developed. The method consists of piezoelectric strips and photovoltaic cell strips, both flexible, thus obtaining solar and wind energy. The flags were made with materials existing in the market, without being manufactured, and for that reason, they present some geometric and mechanical limitations [20].

The tests were carried out in a wind tunnel, with a concave circular shape with an orthogonal section; the lighting was composed of two LED lamps placed at a 45º angle at the rear of the flag. The results show that the piezo strips act as cushioning, and the part of solar panels acts as an additional mass of the flags. The analysis shows that since solar panels were slightly less flexible than piezoelectric strips, solar collectors restricted the deformation of piezoelectric materials if they were located near the flag's rear edge. Even with these observations, the new piezo/solar energy collection device may generate 3 to 4 mW of energy, thus being a viable concept and anticipating that, in a real application, several inverted flags adequately adjusted to obtain the desired performance at all wind speeds [20].

In another analysis, a numerical model resulted in a calculation to obtain solar thermal collectors' performance on textiles with different layers. The model presented is based on the numerical resolution of the different elements using an algorithm capable of using each component's different simulation levels. With the model, airflow temperature profiles and useful heat gain were calculated [21].

This system of facade transfers heat through a panel on the exterior wall to a pipe that runs between the building and the panel. This water, as it passes through the pipe, is heated and then stored for use in the shower and kitchen. The heat pipe system provided a greater amount of

heat than the other passive options in all climates, with the most advantageous performances in cold and overcast weather. In addition, this type of facade helps with energy waste, because during summer, the solar radiation reaching the vertical surfaces is reduced by containing the pipes, thus avoiding overproduction of thermal energy since the building material does not overheat, and no methods for cooling the room are needed [35,36].

The market for solar thermal collectors is increasing, especially in countries like Germany and Austria, where appropriate incentives have permitted the development of energy-generating building envelopes (30). In addition to these countries, Portugal has developed an innovative technology, SENERGY FORCE, which has developed panels that heat water and also provide ventilation and air conditioning, only using the energy of the sun [36].

The project developed by the Portuguese company presents a piping system inside the panel for the circulation of water. When the panel heats up due to the action of the sun's rays, this heat is transferred to the water. In addition, through convection, the heat from the panel enters the building, keeping it warm even during the winter. In addition, it promotes the natural renewal of the air in the environment [37].

In addition to the water collection systems on the facades, there are also integrated photovoltaic/thermal systems (BIPV/T) in the buildings. In these systems, in addition to on-site passive solar thermal energy storage , heat recovery also occurs mainly through active cooling of the photovoltaic surface, using open-circuit air [38]. According to some authors [9, 39–41], BIPV/T provides an increase in electricity production, keeping the photovoltaic cell at considerably lower operating temperatures throughout the year.

2.4.2 Roofs

The buildings' roofs also receive a high incidence of sunlight, thus generating energy since they are often not used by the owners. Thus, several studies address techniques for obtaining energy in roofs from photovoltaic cells, TEGs, and materials with phase change in gutters.

The use of photovoltaic panels in the building's external area takes advantage of the buildings' innovative planning and configuration so that the performance evaluation is quite beneficial in all the exterior urban areas. The roofs have obtained benefits in cooling the building since the solar panels protect the building. Besides, the planning for the deployment of photovoltaic panels in outdoor locations with greater solar incidence reached a high value in obtaining energy, reducing the entire building's net energy costs and indicating an equivalent reduction in CO_2 emissions [5,42].

The use of a material to harvest solar energy using photovoltaics or photoelectrochemical due to the material's efficiency, Cu 2 SrSnS 4 (CSTS), can absorb light. The material was a mixed

solution of copper, tin and sulfur with a solution containing strontium. The results show that the film annealed at 600° C revealed better crystallization; however, for the control of the secondary phases, they were prepared with different atomic values of the strontium/foreign ratio, obtaining a rate of 1.15; 1.30, 1.45, and thus having the ability to convert photoelectricity [43].

In the north of Taiwan, the energy harvesting analysis from different photovoltaic sources (PV) occurs. The experiments, in the north of Taiwan, were applied with single-axis photovoltaic systems (SASTT), a dual-axis solar tracking (DASTT), and a fixed photovoltaic (FT) system; all systems with a power of 3.68 kW at different inclination angles [44].

A theoretical and an experimental method were used to obtain the analysis of energy harvesting. In the theoretical module, a formula was developed to calculate the inclination angle, the relationship between the sun's rays' angle, and each system's electrical parameters. In the experimental model, the energy capture, with an inclination angle of 23.5° from the FT system and the SASTT system, was compared over a total of 6 months. Then, the FT system was compared to two angles of inclination 0° and 23.5° for one year. The experiment was installed on the roof of a factory [44].

In the first experiment, a value of 15.1% of the SASTT was found with the FT system, both with an angle of 23.5° for six months. In the theoretical simulation calculations, 16.1% of the SASTT was obtained with the FT system. Thus, less than 1.2% is observed between the experimental and theoretical part [44].

In the second experiment, the FT system's comparison at 23.5° and 0° angles did not obtain such an explicit increase, getting a greater value at the 23.5° angle. The results of the theoretical tests also did not show a significant difference. This is because the sun in Taiwan radiates directly to the ground only in summer, so that over a year of the experiment, it did not vary much [44].

The harvesting of solar energy from ferroelectric materials obtains a high production of photovoltaic energy, getting better results than conventional photovoltaic mechanisms. The analyzes show that the $BiFeO_3$ or BFO, as a film in ferroelectric-photovoltaic applications, obtained excellent results in power generation [45]

The temperature difference at the bottom of the photovoltaic panel, where the temperature reaches 70° C, and the ambient air reaches 30° C. This difference can be used to obtain energy through TEGS. The energy captured by TEGS was 3.3 V with an intensification of around 220 mV obtained with a difference in average monthly temperature of 15° C. Besides, it has been demonstrated that 528 mV can be collected every 30 ms [46].

Also, the analysis of the temperature difference of the TEGS, using the materials, can be obtained with the hot cell in contact with the black iron roof, and the cold part which is in the

shade [34]. In turn, solar energy can be obtained using photovoltaic plates and thermoelectric sensors clicked on the roof of buildings, thus obtaining a greater use of solar incidence to capture energy [48].

The collection of ambient solar energy to charge wireless sensor networks' batteries maximizes the wireless sensor network's service life using the collection of solar energy. The simulators show that the wireless sensor network's lifespan at 25% of the duty cycle is 115.75 days longer than just 5.75 days of solar energy data collection. The use of solar energy capture can benefit an energy restriction project implemented for intelligent monitoring. With this, this network's useful life can be increased for an infinite time using solar energy capture [49].

The latent thermal energy storage method uses phase change material (PCM) at the solar plant where the concentrated parabolic gutter is located. Four different types were used (H250, NaNO 3, KNO3, and KOH). The analysis of the use of NaNO3 in the latent thermal energy storage system presented the best option with a solar fraction of 34.14% among the others analyzed. As a result, the solar fraction increased by 90.5% compared to the plant without the system [50].

2.4.3 Structural materials.

The constructions are made of different materials, having different functions in structures. Many of these constructions are in direct contact with the sun's rays, and the materials can bring more advantages to the building with the capture of energy through the high temperatures reached by the sun. With this, several authors approach new materials and additives in the components used in civil engineering that generate solar and thermal energy.

A block of bricks captures energy using electrical generators (TEG) and phase change materials. Power generation is supplied to the block using the residual heat accumulated on the building's external wall surface. The average amount of electricity generated is approximately 0.1 Wh in one block [38]. In addition, there are Fresnel lenses that concentrate the sun's rays on the hot part of thermoelectric generators based on bismuth telluride. The temperature obtained on the hot side was 140º C, and on the cold side, it was 44º C, getting a value of 0.615V and 84.9 mA with the temperature difference of a single TEG, Figure 4 [52].

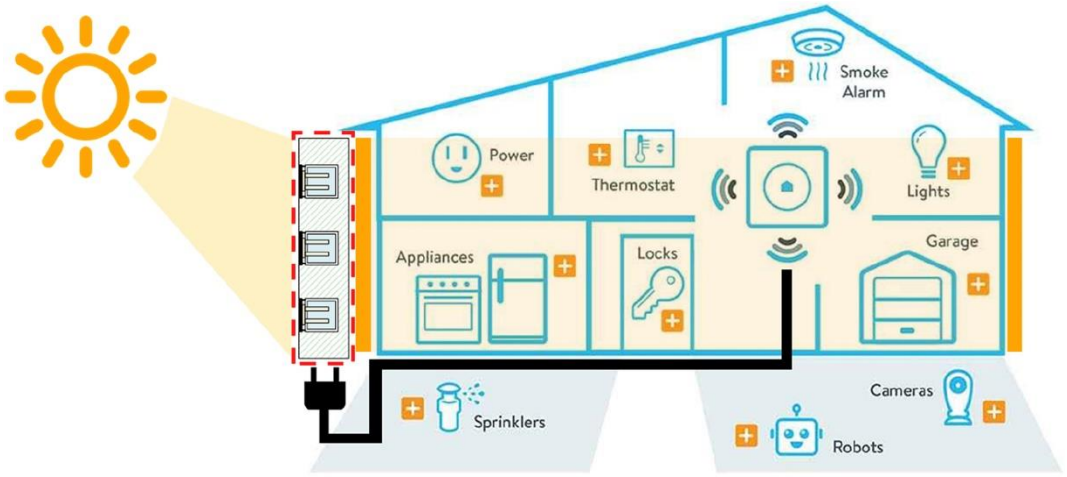

Figure 4: Application of the TEG-PCM brick wall [51].

Another way of obtaining energy from the buildings' structure is through thermoelectric materials based on cement which converts the heat absorbed by buildings' surfaces in the summer into electrical energy. These materials can improve buildings' internal climate, energy consumption with interior thermal comfort, and external energy capture. These materials can improve buildings' internal atmosphere and energy consumption with thermal comfort inside and energy capture outside [53–55].

The electrical conductivity of composites rises with the increase in the percentage of graphene (PNB). Just as the conductivity also increases with rising temperature. The addition of 20% of GNP to the cement caused a value of 16.2 Scm-1 of electrical conductivity—the Seebeck coefficient for all is positive, which confirms that composites are semiconductors. With 15% of GNP, the highest value of the Seebeck coefficient, 34 μVK-1, is obtained at a temperature of 70° C [54].

Additionally, as the carrier density of the specimens increases, the Hall coefficient decreases. The best results of mobility and density of carriers were found for the cement sample with 20% of GNP. The values of thermal conductivity increase with increasing GDP content. However, the impact of GDP content is much more significant on electrical conductivity than on thermal conductivity [54].

The thermoelectric properties of cement with the addition of expanded graphite (EGCC), whose compound has a high Seebeck temperature coefficient with a value of 30° C to 100° C as well as an electrical conductivity of 24.8 S/cm. However, the increase in the amount of graphene in the sample resulted in a reduction in compressive strength and increased apparent porosity [55].

Using cementitious materials plus electrochemically exfoliated graphene (EEG) presents better microstructure and mechanical properties and presents high workability concerning cement without EEG. The EEG presents a simple and efficient method that allows a uniform dispersion

in the cementitious matrix. It does not agglomerate in the cement's alkaline medium, improving its fluidity and workability. The cement's mechanical properties were analyzed; notably, the addition of 0.05% graphene to Portland cement presents a better result [56].

Analysis of traction results showed an increase of about 79%, as well as an 8% increase in compressive strength and 9% in Young's modulus. Besides, graphene presents a hydration reaction of calcium silicates and a compact and regular microstructure. With this, the author's results show that the compound with graphene analyzed can drive a new technology for concrete, allowing the design of lighter and more durable concrete structures [56].

The graphene-added cement used in buildings can offer an advantage not only for capturing energy but also for improving the thermal comfort of the internal atmosphere. Thus, graphene material can provide a very beneficial contribution to construction energy collection applications since it is a low ambient temperature gradient and can be used as a clean energy source to improve energy consumption in construction [54,55].

Solar concrete collectors are a very advantageous alternative for obtaining thermal energy for hot water and space heating applications. The materials used, the geometry, the material surface, and the fluid flow were used. Solar concrete collectors are simulated using a 2D finite element model with a 56% daily efficiency predicted for a clear day in Ireland. The collector covered in this research is an alternative with benefits and durability, such as applications in temperatures below 40º C, Figure 5 and 6 [57].

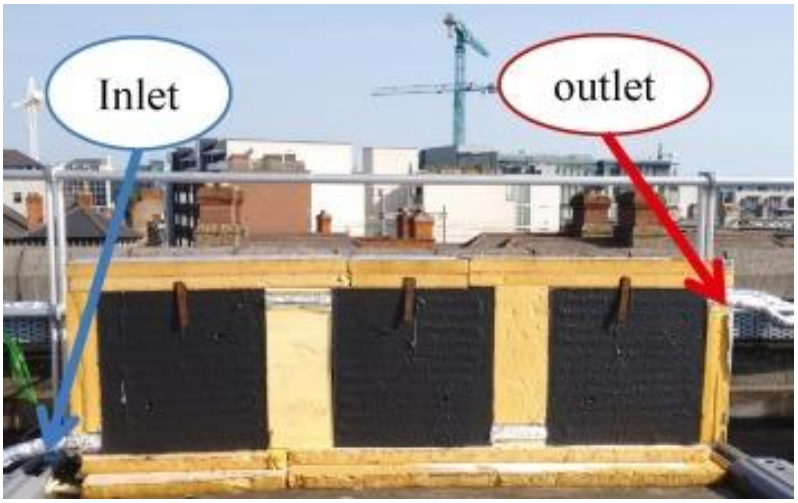

Figure 5: Construction of an experimental concrete solar collector in Ireland [57].

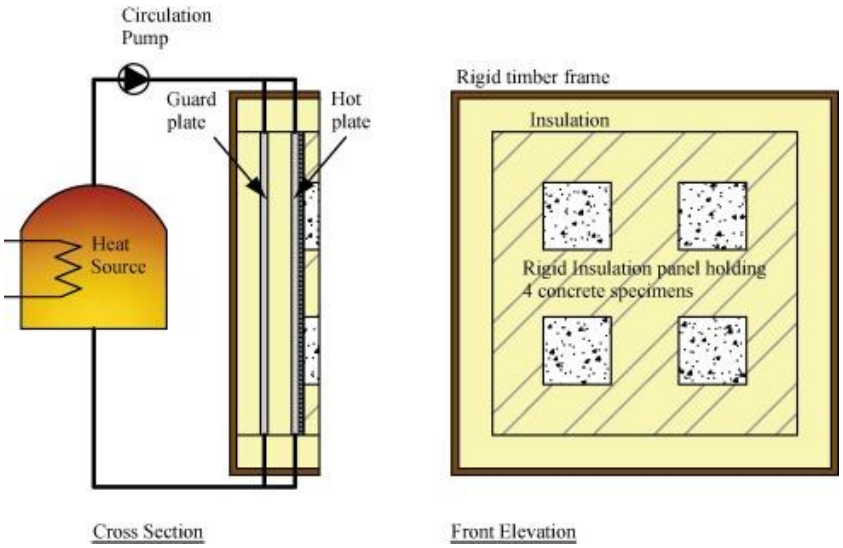

Figure 6: Concrete thermal conductivity test schematic [57].

The devices that harvest energy from the environment using thermoelectric and phase change materials (PCMs) to supply energy to various electronic devices through heat transfer were designed to improve the performance of the energy capture system. The mechanism was proposed to be built and analyzed in an environment with a temperature difference between 0° C and 40° C for three days. The entire system was placed in a simulated environment to respond to changes in temperature [58].

This device is divided into two similar modules, where the only difference is a variety of PCMs with different melting points. The PCM module uses cubic copper foam in paraffin as a thermal insulation container. This storage place is made of transparent plastic and a copper plate; the material is welded to reduce heat loss. For simulation at room temperature, heating a 0V to 30V power source was used, and dry ice cubes in the cooling condition [58].

The results presented show that the device for capturing thermoelectric energy in double PCM obtained a load resistance value 35.8% higher than that of simple PCM. Also, numerical models were performed but showed large deviations in reaction to the experimental ones. The use of the energy harvesting device based on double PCM makes the generation of energy more uniform in situations with great temperature differences, being more efficient for generating energy [58].

Another compound, nanofluids, can be used in the building structure for improved thermal absorption as properties of solar thermal conversation; the fluid contains copper (II) oxide (CuO) and antimony-doped tin oxide (ATO) prepared after surface development of CuO nanoparticles. The results show that the efficiency of solar thermal utilization of the nanofluids of two components together obtained 92.5% when compared to 81.3% of Cuo nanofluids and 80.7% of ATO [59].

However, nanofluids can be used in solar desalination equipment and steam generation equipment to obtain energy [59,60]. In addition, according to the author [47], the comparison of two different types of systems, one for surface absorption and the other for nanofluid, shows that in the absorption of cobalt oxide nanofluid, there was an increase in the average temperature around 23.3º C. This value is approximately 9.3º C higher than the surface absorption system.

The phase change through the generation of steam is a source of energy production. The materials used for this purpose were vertically oriented graphene nanofilms and highly porous graphene aerogel to obtain an ultra-fast solar thermal response. A temperature increase of 169.7 in 1 second occurs. This material is heated by the sun's rays and heat transfer; steam occurs with the water heating, thus generating energy [61].

Erythritol can cause several disadvantages for energy capture and to solve the supercooling, low conductivity, and malabsorption of solar energy from Erythritol, a low-cost commercial metal foam was used through a simple manufacturing process in one rough surface with the use of crushed graphene particles. The results show that the degree of supercooling decreased from 85.8º C to 26º C, improved the thermal conductivity from 0.7 W / m K to 4.5 W / m K, and the total absorption of sunlight, indicating a high adaptation for adaptation to solar energy [62].

The mixture of rubber tires and steel fibers presents the thermal behavior of recycled rubber tires reinforced with steel fibers with an excellent performance as solar collectors, showing that the addition of steel fibers can increase the amount of heat absorbed and heating rate of the material. However, adding more than 0.5% of the fiber does not change the temperature. With the addition of 0.5% steel fibers, rubber transmitted heat to the water, reaching 45º C [63].

2.4.4 Pavements

Pavements are components of a large city made by civil engineering. These structures occupy a large area and, consequently, receive a high incidence of sunlight. Bearing this in mind, several factors were considered by researchers to obtain energy from the pavements. The most used methods in the research are thermoelectric road systems (RTEGS) and asphalt collectors (ASCs). Several factors approached the methods with new systems and modes of execution to obtain the best harvesting energy results.

The new RTGS system was developed to supply electricity with a difference in temperature and ambient air. With a 1km long and 10m wide road, 160 kWh of energy was generated in 8 hours of exposure to the sun [64]. Another author also uses TEG to get solar energy from the pavement using the temperature difference of the pavement surface and of a lower part of the structure where there was an aluminum bar, obtaining a temperature difference of 20º C between the materials, thus being sufficient to power an LED light [65]. Besides, a thermoelectric system is used on the surface of the pavement and on the ground below the

pavement to obtain energy also from the temperature difference [65]. In South Texas, this method was tested using the real dimensions of the highway (10m wide and 1 km long), and an average of 23.2 kWh of electricity was obtained [66].

The generation of energy using the system that extracts thermoelectric energy from the asphalt pavement can have, according to research, better results by increasing the conversion efficiency of TEGs, defining the ideal system configuration, changing the thermoelectric properties of the pavement, and using the point tracking algorithm, Figure 7 [54]. Also, a new form of feedback control is required for the system, in which the Air Source Heat Pump (ASHP) ON/OFF connected to the heat storage tank (HST) is activated by comparing the temperature [68]. TEG was installed in water pipes, one heated by the sun's rays and the other cooled by water from a river. The three different temperature types were found: 40.5° C; 25.5° C; 11.5° C, thus obtaining electricity values of 5W; 2.9 W and 0.9 W [14,69,70].

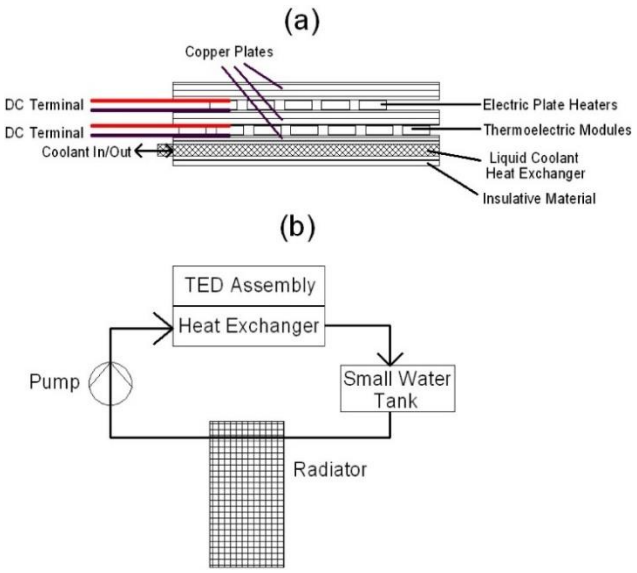

Figure 7: Details of the experimental platform (a) TED layers, (b) liquid cooling system [71].

In the networks of fluid tubes incorporated in the pavement structure, the solar asphalt collectors (ASCs), the fluid passes through the duct, which is heated along the way, as there is a transfer of heat from the surface material to the duct and, consequently, for the liquid, Figure 8. The first ASC projects involved metal pipes, but the data was considered favorable for corrosion and leakage. Subsequent projects involved plastic or polyethylene tubes and obtained better performance. The largest increase in temperature between the inlet and outlet was achieved with copper tubes, followed by the radiant PEX-AL with a difference of only 3° C, thus using cheaper materials [14,51,52,72–74].

Figure 8: Construction of a solar pavement collector near Östersund, Sweden [75].

The materials used in paving the new ASC systems have more advantageous criteria for increasing heat transfer with highly conductive materials. However, according to the documents, there was not much change in the results with graphite results. Another solution to increase the systems' efficiency is to paint the floor surface black to increase thermal conductivity [14,76].

The thermoelectric effect through piping on the asphalt pavement is a method that can lower the floor temperature and mitigate the damage caused by high temperature. The floor can also capture clean electrical energy through the piping inserted into the floor and uses the heat collected from the floor to raise the liquid's temperature in the pipe. The passive solar thermal energy storage is obtained by the temperature difference between the hot liquid and the tube's cold liquid [7,31,67,72,75].

The photovoltaic materials on the pavement were analyzed and indicate that the application of photovoltaic cells with thinner layers on the pavement presents many challenges since they are difficult to maintain their durability due to high traffic loads and the different climatic conditions floor is exposed to. However, applications of photovoltaic technology protect against noise in the surrounding areas [14,65].

2.5 Advantages and disadvantages

Each type of solar energy harvest system used in the chosen civil engineering works has its characteristics, with advantages and disadvantages depending on its performance, maintenance, and aesthetic potential. The selection of the most suitable system is directly related to the buildings' characteristics and climatic conditions. The tables indicate the advantages and disadvantages according to the place and type of harvest.

Table 1: Advantages and disadvantages of facades

Facades	
Advantages	Photovoltaic: -Use of photovoltaic cells in windows and blinds to obtain greater natural light and solar energy [27-32]. Thermal materials: -Use of window glass to heat a water pipe to provide solar energy and greater natural lighting [28]. -Use of fabrics that can be used in lighting locations to generate energy [13,32]. -Use of anchor paints with components that increase thermal conductivity [31]. Pyroelectricity: -Use of a new ceramic with components that increase the redemption of solar energy generation. In addition to increasing the breaking strength of the ceramic [28-30].
Disadvantages	Photovoltaic: -Limited architecture and aesthetics [22-27]. -Visual pollution [22-27]. Thermal materials: -Limited architecture and aesthetics [13,23,31,32]. Pyroelectricity: -Limited architecture and aesthetics [28-30].

Table 2: Advantages and disadvantages in roofs.

Roofs	
Advantages	Photovoltaic: -The use decreases the internal temperature of the building [33]. -The CSTS component in the photovoltaic cell increases energy generation [34]. -The SASTT system showed better power generation than the FT [35]. -Ferroelectric materials increased the energy generation of photovoltaic cells [36]. Thermal materials: -The increase in energy generation using $NaNO_3$ material as a phase change in a roof gutter [41]. TEGs: -Consequently, the temperature difference and energy generation increase through the photovoltaic plates' surface and the shaded part [37,38]. -The high-temperature difference between the roof and the shaded part [37,38].

Disadvantages	Photovoltaic: -Visual pollution [33-35] Thermal materials: -It was not observed TEGs: -It was not observed

Table 3 : Advantages and disadvantages in structural materials

In structural materials	
Advantages	Thermal materials: -Adding graphene and EGCC to cement increases thermal conductivity [44,45]. -It improves the internal comfort of the building [44,45]. -It presents better microstructure and mechanical properties and presents high workability concerning cement without EEG [46]. -The solar concrete collector achieves a good performance in energy generation and durability. In addition to obtaining water with a different temperature to be used in the building [47]. -The use of 2 types of phase-changing material makes the generation of energy more uniform with a large temperature difference [45,46] -The addition of 0.5% of steel fibers increases energy generation [63]. TEGs: -Get energy with materials with phase change in bricks. -Fresnel lenses concentrate the sun's rays on materials based on bismuth telluride [42]
Disadvantages	Thermal materials: -If excess graphene is added, the porosity increases and the compressive strength decreases [45]. TEGs: -It was not observed.

Table 4: Advantages and disadvantages in pavements

Paving	
Advantages	Photovoltaic: -large extension and protection against noise [18] Thermal materials and TEGS: -The floor material has high thermal conductivity [49,55]. -Dark color [31,57,58,62]. -High conductivity for water in the pipe [72]. -PEX-AL tubing performs better [18,43,59–64].
Disadvantages	Photovoltaic: -Low durability due to high traffic loads [18].

	Thermal materials: -Iron pipe showed corrosion and leakage [18,43,60–64]. TEGs: -It was not observed.

2.6 Thermal energy storage

Passive Solar Thermal Storage highlights the increasing use of technologies to efficiently store thermal energy, especially in light of the need for renewable and sustainable sources. Thermal Energy Storage is a promising approach that allows for the capture and storage of solar heat for later use, helping to regulate temperature and maintain energy supply during periods of low or no solar radiation.

In the context of passive solar energy, sensible and latent heat storage are the most commonly used approaches. Sensible heat storage is achieved through materials such as water and masonry, which absorb and release heat according to temperature variations. Technologies like water tanks and underground systems are widely used in buildings and industries. On the other hand, latent heat storage, which utilizes phase change materials and high metallic compound materials, is increasingly being explored for its high thermal storage density and ability to regulate temperature in applications such as solar heating and passive cooling of buildings [73–75].

The growth prospects for thermal storage are considerable, with the market projected to triple by 2030. Technologies such as molten salt storage, widely used in concentrated solar power plants, show great potential for expansion. Furthermore, thermal storage plays a crucial role in the transition to a renewable energy-based system, particularly by enabling the decoupling of heating and cooling demand from the availability of solar energy[74].

This evolution underscores the central role of thermal storage in energy efficiency and long-term sustainability.

2.7 Research needs

As it has been analyzed in recent years, there has been an increase in the number of articles dealing with the capture of renewable energy, thus realizing that reducing pollutants in the environment for passive solar thermal energy storage is becoming increasingly more significant. The studies also analyzed studies of different methods, therefore having different options for obtaining energy according to the construction to be carried out. According to another source of information [76], according to the assessment carried out in Portugal, there was an increase in

renewable energy generation in 2020 in Portugal. However, the percentage of solar energy is small.

Therefore, there is a need for further research in the field of harvesting solar energy. According to the analysis of this research, the most studied and relevant method was the use of materials to increase thermal conductivity in all types of energy production analyzed in this study, recognizing that the best knowledge of the materials can provide a better performance of energy. This indicates a need for further studies on the different types of materials, mainly the analysis of waste, to improve solar energy capture.

2.8 Conclusions

The sole purpose of writing this review, which addresses the harvest of solar and thermal energy, is to provide knowledge of existing methods for use in various civil engineering constructions. Our bibliographic study explicitly focused on five types of energy capture: thermoelectric generator, solar asphalt collectors, photovoltaic cells, thermal and pyroelectric materials, divided into local frameworks where they are executed: on facades, roofs, and structural materials. The following inferences can be made:

- Different methods of harvesting solar energy and thermal materials using Thermoelectric Generator (TEG), solar asphalt collectors, photovoltaic plates, pyroelectric and thermal materials were obtained through numerical simulations and/or experimental tests in climatic conditions as well as bibliographic articles.

- The number of articles on the topic found on the Science Direct database, between 2017 and 2020, was not as expected. This means that in the last four years, little attention has been given to methods of solar capture and thermal energy to use in civil engineering. The piezoelectric method of capturing energy is much more studied, according to the analyzed articles.

- It was also found that there was an increase in the number of articles on the topic of energy harvest, renewable energy, and, consequently, also an increase in the number of articles dealing with solar and thermal energy, but still in a small percentage.

- Studies with these methods are of great importance, and research on renewable energies in different parts of the world is increasingly common. However, studies on passive solar thermal energy storage from the sun and temperature are rare, which can be considered quite peculiar because the sun and high temperatures exist worldwide. These methods do not emit pollutants and ensure savings for the population if used in engineering projects, for example.

- With the large amounts of pollutant emissions emitted to the environment, it is very important to study alternative renewable energy generation methods, such as piezoelectric, solar, thermal, marine and wind power. However, like many authors mentioned in this document, it is extremely beneficial to develop new materials that provide energy for construction, as shown by

the great number of thermal materials' advantages for all energy capture types addressed in this study.

Chapter 3- Review of electric-arc furnace slag (EAF-slag) and carbonated materials

3.1 Preface

This chapter discusses the state of the art of electric arc furnace slag and carbonated material, with the aim of analyzing the origin of EAF-slag, the chemical reaction that occurs in accelerated carbonation, and an investigation of research and industries working with carbonation accelerated.

3.2 Introduction

Research and development addressing sustainable production in civil engineering are growing worldwide due to the current climate emergency to combat climate change and adapt industrial production to a more sustainable way [77]. Fossil fuel plants are the ones that produce the most CO2 (a total of 40%) [78]. As for the construction industry, Portland cement is one of the materials responsible for CO_2 emissions directly, with 15 %, and indirectly through its production process [79,80].

Besides, one of the most significant environmental problems is the mineral waste taken to landfills. These sites are potentially collapsing and can generate severe ecological impacts and health and safety problems for the local population [81]. The world production of steel slag is on a large scale, around 130 million tons, and a large part of this production is taken to landfills [82].

3.3 Electric-arc furnace slag (EAF-slag)

A steel slag is the primary byproduct of steel manufacturing and is often dumped in landfills , Figure 9. In Europe, road construction extensively uses a significant amount of slag as aggregates. In the year 2012, nearly half of the produced slag was utilized. However, there still exists a considerable amount of slag that has not been reused or subjected to recycling processes [83,84].

Figure 9: Slag manufacturing [85].

The chemical composition of steel slag depends on the steel production process, which is also a crucial factor in its reactivity to CO2. Basic oxygen furnace (BOF) slag consists mainly of calcium, iron and silica oxides. The iron oxide (FeO/Fe2O3) content can reach 38%, silica (SiO2) varies from 7 to 15% and calcium oxide (CaO) is the highest compound, ranging from 36 to 60% [86]. Electric arc furnace slag has a similar composition to basic oxygen furnace slag due to similarities in production processes. However, because recycled steel scrap is used, the chemical composition of electric arc furnace slag also depends on the properties of steel scrap. The iron content can reach 40%, SiO2 is approximately 16% and CaO is not the highest compound, as in basic oxygen furnace slag, ranging from 23 to 38% [87,88].

Steel slag has high reactivity to carbonation due to its free CaO/MgO content, making it a suitable raw material for carbonation-activated construction materials [89]. Along with free CaO/MgO, hydraulic calcium silicate (Ca3SiO5 (C3S), ß-Ca2SiO4 (C2S)), non-hydraulic calcium silicate (γ-C2S, CaSiO3 (CS)) and Portlandite (hydration products of free CaO or calcium silicate) are also reactive components for the carbonation of steel slag [78]. These reactive components contribute to the formation of calcium/magnesium carbonates and calcium silicate hydrate, which are the main phases responsible for the binding capacity and development of compressive strength [90].

3.4 Carbonated materials

Since the industrial era, the world has suffered from large amounts of CO_2 in the environment. This increase over the years is partially due to deforestation and land change activities, natural causes and mainly emissions related to the use of fossil fuels. This causes the interruption of the natural carbon cycle, altering the storage of CO_2 in terrestrial and oceanic reservoirs. The carbon cycle is the process of carbon exchange between the atmosphere, land and ocean through physicochemical and biological processes. Carbon flows within terrestrial systems involve the absorption of CO_2 by plants for photosynthesis to occur [91].

Currently, there are several CO_2 reduction schemes and technologies to limit global warming. These efforts have been proposed by governments, industry leaders and scientific institutions. One of these proposals is carbon capture and its storage strategy [92].

Initially carbon capture was requested only to eliminate high CO2 emissions. However, today, with the discoveries of the benefits that capture and utilization have obtained, they have become an alternative and sustainable resource for the energy, water and food sectors. Carbon capture and utilization is considered an important strategy for mitigating excess CO_2 in the environment. Methods that utilize CO_2 are mainly divided into five categories: conversion of CO_2 into chemicals and fuels, mineral carbonation, enhanced oil recovery, biological conversion, and direct utilization of CO_2 [93].

The mineralization process is not only considered a means of improving carbonate protection, but also of storing CO_2 in geological formations, with one ton of CO_2 being absorbed by approximately 1.6-3.7 tons of rock [94]. Carbonation occurs naturally when metal oxides, such as magnesium and calcium, react with atmospheric CO_2, however, it is a slow process. On the other hand, the occurrence of CO_2 with metal oxides found in minerals is an exothermic occurrence, due to the lower energy state of carbonates compared to CO_2 [93].

In other studies, the main compounds for the occurrence of carbonation were identified. Calcium and magnesium oxides are mainly responsible for the high capture of CO_2. According to Equations 1, 2 and 3, carbonation occurs in Mg and Ca silicate minerals with atmospheric CO_2, which results in the precipitation of carbonates [95–97].

$$Mg3Si2O5(OH)4 + 3CO2 \longrightarrow 3MgCO3 + 2SiO2 + 2H2O;\ \Delta H = +64kJ \qquad Eq(1)$$

$$Mg2SiO4 + 2CO2 \longrightarrow 2MgCO3 + SiO2;\ \Delta H = +89kJ/molCO2 \qquad Eq(2)$$

$$CaSiO3 + CO2 \longrightarrow CaCO3 + SiO2;\ \Delta H = +90kJ/molCO2 \qquad Eq(3)$$

With the discoveries made by other researchers, the carbonation process is divided into two types: direct and indirect. The direct process is carried out through a single-step process, where the degradation of the rock mineral coincides with the formation of carbonate under high pressure and requires low amounts of energy. The indirect reaction has three systematic reactions and allows for faster kinetics. The first occurrence involves removing the metal from the mineral rock using a separating agent such as molten salts. The second occurrence involves hydration of the metal to form metal hydroxides. Finally, the third occurrence is an occurrence of carbonation of CO_2 with metal hydroxides to produce carbonates [95].

One application of mineral carbonates is in the construction industry using blocks obtained by carbonation instead of Portland cement-based blocks, because of their high amount of negative carbon. In addition to natural mineral rocks, waste from the steel or cement industries, which

are rich in calcium and magnesium oxides, can also be used to form carbonates in the presence of CO_2 [83,97,98].

In block production, CO_2 collection conditions are important and must be controlled and understood, as they affect the kinetics of carbonation occurrence and have a strong influence on the development of material properties. The water content of the mixture is a critical parameter because it influences reactivity. Furthermore, the penetration of carbon dioxide into the block depends on the free water present in the matrix pores [10]. On the other hand, temperature is an important aspect for the occurrence, and it is necessary to establish an ideal temperature, as high temperatures generate the diffusion of CO_2, but accelerate the evaporation of water and protect wet solubility [82].

Carbonation also contributes to increasing the mechanical properties and durability of materials. According to various research, materials can be carbonated for different purposes, either to improve the properties of concrete, with CO_2 storage inside, or with the development of a binder activated with carbon dioxide. For materials activated with carbon dioxide, carbonation also plays a role in strength [78,96,99].

3.5 Related studies

Several studies have demonstrated great potential for using steel slag as an innovative material by accelerated carbonation. This technology does not require a high amount of water and a faster production cycling compared with cement hydration. This technology is already being studied to produce marketable construction products [78,84,100].

The C-MADE research center has been actively engaged in the DARKCO2 project since 2019, leveraging accelerated carbonation techniques to manufacture construction elements using industrial waste, by-products, wastewater, and CO2. The primary objective is to produce sustainable construction materials while mitigating the ecological impact of industrial processes.

In its commitment to environmental , CMADE is exploring the feasibility of capturing and storing CO2, treating it as a valuable resource similar to the way trees utilize greenhouse gases. This innovative approach aligns with the broader environmental goals of utilizing waste streams to create valuable building components.

Collaborating with another CMADE initiative, ECO2BLOCKS, the laboratory is actively researching the optimal formulation for creating blocks with maximal CO2 sequestration. Currently, a 25 kg block (measuring 50 x 25 x 20 cm), Figure 10, is manufactured using 23 kg of industrial waste, primarily slag, along with 1.5 kg of wastewater and 0.5 kg of CO2. Subsequently, the block an accelerated carbonation process.

Figure 10: Block made of EAF-slag [85].

At the moment, the laboratory refrains from incorporating Portland cement in any of its compositions, recognizing its significant role in the release of greenhouse gases during concrete production. This conscious decision reflects a commitment to sustainable practices and environmental responsibility.

Master's studies have extensively investigated the utilization of thermo-activated recycled cement in conjunction with construction waste aggregates, employing accelerated carbonation techniques. The outcomes have proven highly advantageous, revealing exceptional strength properties and significant CO2 absorption capabilities [101].

Ongoing studies led by doctoral students include the analysis of the thermal properties of 100% EAF-slag blocks. Additionally, there is an investigation into waste materials with high magnesium to analyze for accelerated carbonation processes. These comprehensive research endeavors underscore CMADE's dedication to advancing sustainable construction practices and minimizing environmental impact in the realm of construction materials.

3.6 Industries involved in the production of materials by accelerated carbonation

The market for CO2-absorbing materials is undergoing substantial growth, with numerous innovative ideas emanating from laboratories poised to revolutionize the construction sector and address the challenges of sustainable development. This surge in expansion reflects a dynamic landscape where advancements are continually shaping a more environmentally conscious and sustainable future for the industry.

3.6.1 Blocks -CarbiCrete

The CarbiCrete technology closely resembles the ECO2BLOCKS and DARKCO2 projects, employing slag in conjunction with an accelerated carbonation process. Established in 2016, the

Canadian company introduces carbon-negative blocks, Figure 11, capable of absorbing 3 kg of CO_2 each. The company has forged partnerships, currently collaborating with a precast concrete factory, and is successfully manufacturing hundreds of blocks daily for the construction of retaining walls and foundations [102].

Figure 11: Blocks- CarbiCrete [102].

Despite these achievements, questions persist regarding the long-term durability of the material and potential concerns about the future availability of slag resources [102]. These uncertainties highlight the need for ongoing research and development to address these aspects and ensure the sustained effectiveness and viability of this innovative carbon-negative building solution.

3.6.2 Blocks -CO2ncrEAT

The CO2ncrEAT project is the outcome of collaboration among four Belgian companies. It employs slag and accelerated carbonation techniques to craft masonry blocks, Figure 12. Securing a substantial €4 million funding grant, the initiative is poised to commence the production of their carbon-negative blocks on a local scale, starting from 2025 [103,104].

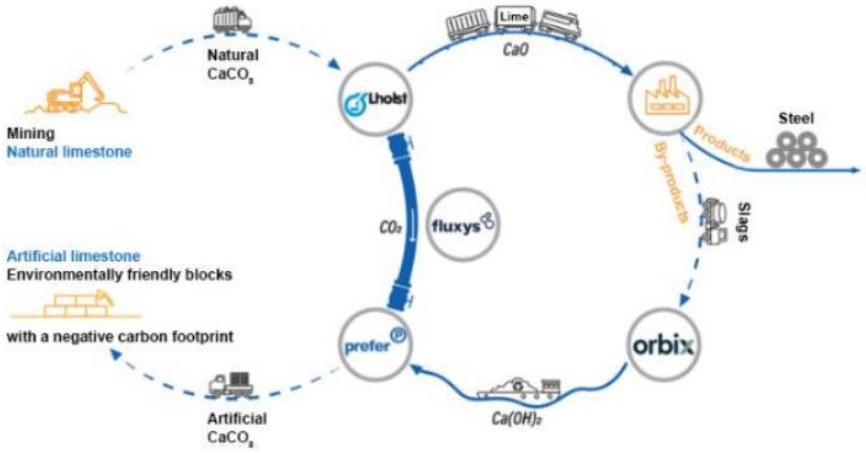

Figure 12: The block process – CO2ncrEAT [104]

3.6.3 Concrete - CO2-SUICOM

The CO2-SUICOM Japanese technology stands as the pioneering example of commercially available carbon-negative concrete, Figure 13. By incorporating cement, coal ash, and a special admixture, this innovative approach slashes CO2 emissions by half in comparison to traditional concrete production methods. Further enhancing its environmental impact, a forced carbonation curing process enables the capture of more carbon dioxide than is initially emitted. The CO2SUICOM has undergone testing for foundations, blocks, and building elements, showcasing its versatility. While there have been notable advancements, the technology currently grapples with cost challenges, and a thorough assessment of its long-term durability is necessary [105].

Figure 13: Concrete - CO2-SUICOM [105].

3.6.4 Mycelium Insulation-Biohm

The Mycelium Insulation-Biohm, derived from mushrooms grown on agricultural waste, possesses natural fire resistance, excellent insulation, and acoustic properties. Additionally, it exhibits carbon dioxide storage capabilities. Notably, it is biodegradable and non-toxic, with the potential for cost-effective production in custom-made bioreactors. The English company Biohm is poised to establish a mass production factory in the coming years. Beyond insulation panels, mycelium holds promise for diverse applications across various materials and products , Figure 14 [106].

Figure 14: Mycelium Insulation-Biohm [106].

3.6.5 Concrete/Plasterboard -Mineral Carbonation International

The Mineral Carbonation International, Australian company, captures and stores industrial and atmospheric CO2. It subsequently uses the captured carbon dioxide to develop new construction materials, agricultural products, fuels and chemicals. While many of its projects remain commercially confidential, MCI has already unveiled some innovative carbon-negative solutions for the construction sector, including cement/concrete and plasterboard, Figure 15. The company aims to store approximately 1 billion tons of CO2 in building materials by 2040, reflecting a significant commitment to carbon capture and sustainable practices in the construction industry [107].

Figure 15: Concrete/Plasterboard -Mineral Carbonation International [107].

3.6.6 3D printedhouses/Panels-Mirreco

The Mirreco, another Australian company, innovatively blends hemp biomass with geopolymer to capture CO2 in the realm of 3D printing for the construction industry, Figure 16. This groundbreaking technology aims to facilitate the printing of walls, roofs, and floors, while also producing panels for both residential and commercial applications. Despite its versatility and rapid production capabilities, it's worth noting that this material remains the subject of some controversy [108].

Figure 16: 3D printedhouses/Panels-Mirreco [108].

3.7 Advantages and disadvantages

The Electric arc furnace slag (EAF- slag), a by-product of steelmaking, has attracted attention due to its potential applications in several industries, mainly in civil construction. Its abundance as waste makes it an attractive resource for sustainable waste management practices. By diverting EAF-slag from landfills, its use contributes to environmental conservation efforts. However, a significant challenge lies in the variability of their composition, which can affect the properties and consistency of materials in construction applications. Careful evaluation and processing are necessary to resolve this issue and ensure the suitability of EAF slag-based materials [78,90,109].

One of the advantages of EAF-slag is its potential to increase the strength and durability of construction materials. With proper processing and incorporation into mixtures, EAF-slag can contribute to the performance of concrete and other construction materials. Furthermore, its thermal properties, including high thermal mass and conductivity, are promising for improving energy efficiency and thermal comfort in buildings. Despite these advantages, concerns remain regarding the chemical reactivity and leaching behavior of EAF-slag. Comprehensive assessment and management strategies are crucial to mitigate potential environmental risks associated with their use [83,84].

Accelerated carbonation, a process involving the absorption of carbon dioxide (CO_2) into materials, has emerged as an innovative curing method for cementitious materials. This technique holds the promise of enhancing both the mechanical and chemical properties of materials by facilitating the formation of stable carbonate minerals within the matrix. Notably, it requires a minimal amount of water compared to traditional hydration curing methods and boasts a relatively short curing time of 24 hours. Furthermore, carbonation actively sequesters CO_2, thereby contributing to global efforts aimed at mitigating climate change by reducing greenhouse gas emissions. However, it's worth noting that the amount of CO_2 used in the process is relatively small [83,99,101].

However, the adoption of accelerated carbonation does introduce certain challenges, particularly in terms of equipment requirements. The need for new equipment can pose logistical and financial hurdles, especially when scaling up production for larger materials. Ensuring the feasibility and profitability of implementing this process on an industrial scale remains a crucial consideration [78,95].

Despite these challenges, the environmental benefits of carbonation are substantial. Its ability to enhance the environmental performance of materials by sequestering CO_2 underscores its potential in advancing sustainable construction and waste management practices. However, it's imperative to carefully weigh the benefits against the associated challenges, particularly those related to equipment dimensions and profitability [83,101,102,105].

3.8 Conclusion

The use of electric arc furnace slag (EAF-slag) and carbonate materials represents a significant step towards advancing sustainable construction and waste management practices. EAF slag, as a readily available byproduct of steel production, offers abundant potential for reuse in diverse construction applications. Their incorporation into construction materials not only diverts waste from landfills, but also increases the strength, durability and thermal properties of these materials.

Additionally, the integration of accelerated carbonation techniques adds another layer of environmental benefits by actively sequestering carbon dioxide (CO_2) and reducing greenhouse gas emissions. Carbonated materials have improved mechanical and chemical properties, contributing to their suitability for sustainable construction projects.

Despite the promising benefits of EAF-slag and carbonated materials, challenges remain, particularly with regard to the variability in the composition of slag and other residues, the need for specialized equipment for carbonation processes, and the challenge of further improving the characteristics of carbonated cementitious material. However, ongoing research and development efforts aim to overcome these challenges and optimize production processes to maximize the sustainability and viability of these materials.

Chapter 4 -Research program

4.1 Research methodology

The methodology used in this Phd study was divided into three stages, Figure 17. The first stage involved a literature review, the second comprised a preliminary study of the thermal properties of EAF-slag powder and its chemical composition, and the third focused on investigating the thermal properties and microstructure of mortars made with EAF-slag.

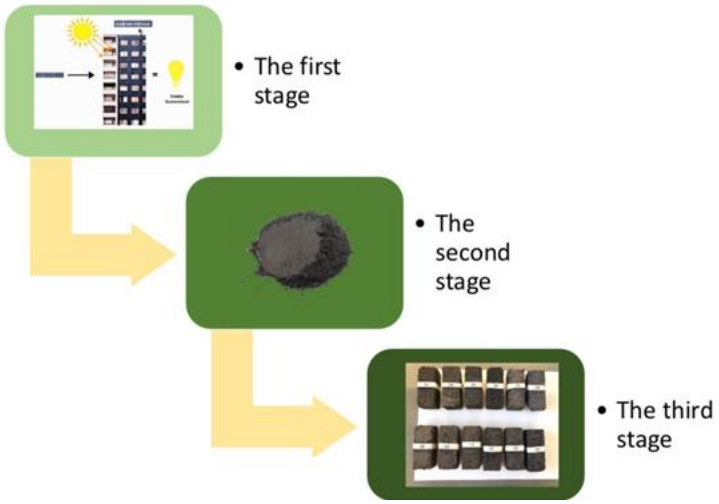

Figure 17: The stage of the methodology

The study began with a literature review on types of solar energy collectors in civil construction, with specific emphasis on passive solar energy. Upon completion of the literature review, a review article titled “Review of Energy Harvesting for Buildings Based on Solar Energy and Thermal Materials” was prepared and submitted to the journal Renewable and Sustainable Energy Reviews. The review article addressed various types of solar and thermal energy capture in buildings and infrastructures. He identified studies highlighting phase change materials and high conductivity materials as advantageous for achieving superior performance in various solar energy harvesting methods, including photovoltaic cells, pyroelectricity, thermoelectric generators and thermal materials. These solutions were found to be applicable in different locations, including building facades, roofs and structures. Furthermore, the review revealed that extensive research on solar energy is relatively limited compared to other studies on renewable energy.

The slag was chemically analyzed and mixtures were developed for preliminary experimental study. The initial proposal compared mixtures containing slag and Portland cement obtained by molding, activated by CO2 and cured by hydration. The thermal capacitance of the material with particle size less than 63 μm was then calculated using the DSC test. One result indicated that blast furnace slag exhibited higher thermal capacitance than Portland cement, as carbonation curing also produced positive results. Based on the results of the preliminary study, an article

entitled "Feasibility of using electric arc furnace slag mortars to improve passive solar energy collection performance" was prepared.

The subsequent phase involved the experimental study of mortars made entirely with EAF slag activated by CO2, analyzing their microstructure and thermal properties. The specimens made of different particle sizes were created to obtain a more comprehensive analysis of the microstructure and thermal properties. The analyzes were carried out at the University of Beira Interior and in collaboration with the University of Leida, including MIP, TGA tests, thermal conductivity tests, compressive strength, thermal response, thermal expansion and Test Box experiments. The results indicate that the materials which incorporate EAF slag have superior thermal properties compared to those conventional materials used by industries, which contain Portland cement.

The results obtained were highly satisfactory for the use of 100% recycled material for passive solar thermal energy storage in civil construction, two articles were published entitled "thermal expansion/energy storage characteristics of eaf-slag mortars for passive solar energy" and "Thermal properties and porosities of 100% electric arc furnace-slag mortars for passive solar energy applications in the construction industry".

4.2 Experimental program

This study endeavors to investigate the microstructure and thermal characteristics of Electric Arc Furnace slag (EAF-slag) activated by CO2, encompassing analysis of prototype specimen composition, aggregate granulometry, additives, and response to thermal property assessments. The primary aim is to scrutinize and characterize CO2-activated EAF-slag specimens for potential application in passive solar thermal energy storage. The CO2-cured specimens comprise EAF-slag, abundant in metallic components, activated calcium, within a controlled CO2-rich atmosphere (accelerated carbonation).

The experimental program unfolds across six distinct phases, with prototypes tailored to achieve acceptable compressive strength as a substitute for Portland cement in construction and infrastructure, particularly for passive solar energy projects. Parameters including EAF-slag fineness, water-to-solids ratio, static compression process, furnace temperature, and carbonation duration are meticulously adjusted to achieve optimal outcomes. The impact of additives and complementary curing processes on CO2 activation is evaluated, while comparative analysis with Portland cement specimens is conducted to discern thermal properties.

The experimental regimen involves scrutinizing the microstructure and thermal characteristics of EAF-slag under carbonation, employing a 99.9% carbon dioxide atmosphere, juxtaposed with Portland cement specimens cured via hydration and carbonation. The utilization of 100% slag material exhibits superior performance, earmarking it for civil construction projects geared

towards passive solar thermal energy storage. Comparative assessments with Portland cement, specifically CEM II/B-L 32.5 N from Cimpor, are also employed.

Varied parameters include binder type, aggregate particle size, aggregate types, water-to-solid ratio, and utilization of biochar. Each parameter is systematically manipulated, while maintaining fixed values for others as a default condition. EAF-slag is sourced from Indústria Siderúrgica Nacional in Maia and Seixal, Portugal, and both EAF-slag and Portland cement powders undergo comprehensive characterization to ascertain reactivity with CO2 and fundamental characteristics.

4.3 Carbonation tests

Each step in the accelerated carbonation testing process is crucial for achieving accurate and meaningful results. Adherence to the specified criteria is paramount, and each step must be executed with meticulous attention to detail and precision.

Chemical and mineralogical analyses were conducted to identify the compounds present in both EAF slag and Portland cement binders. EAF-slag, characterized by its dark color and high metallic content, plays a crucial role in achieving enhanced thermal properties in the specimens.

The particle size of aggregates was carefully selected to compare the thermal and microstructural properties of the specimens. River sand and EAF-slag served as aggregates, with the inclusion of biochar in select specimens. All materials underwent a drying process.

Mixtures were meticulously prepared following accelerated carbonation and pro-hydration curing specifications. The freshly mixed materials were compacted into cubic molds as per test requirements.

The compacted molded specimens were subjected, some to the accelerated carbonation chamber and then 24 hours in the oven to stabilize the chemical reaction. Other specimens were subjected to a hydration curing chamber for 28 days.

For thermal property assessments, specimens were sent to the University of Lleida in Spain, where tests on thermal conductivity, thermal capacity, and response to thermal inertia were conducted. Additionally, compressive strength tests were carried out, and smaller dimensions were sent for Mercury Intrusion Porosimetry (MIP) analysis, while the powdered material underwent testing using Differential Scanning Calorimetry (DSC) and Thermogravimetric Analysis (TGA).

All obtained results were meticulously analyzed and subsequently discussed in detail.

Chapter 5-Materials and methods

5.1 Materials

5.1.1 EAF-Slag

Electric arc furnace slag (EAF- slag) was obtained by Indústria Siderúrgica Nacional in Maia and Seixal, Portugal, Figura 18. It currently serves as a sustainable alternative to traditional aggregates in a variety of construction applications, including compacted soils, floor bases, sub-bases, floor bases, parking lots, landfills, gardens, green areas, railway lines and even football pitches [78]. Previous studies explored the use of EAF slag from the National Steel Industry for alkaline activation [109]. Additionally, other research developed its potential as a Portland cement substitute through accelerated carbonation, producing promising results and even securing a patent[84].

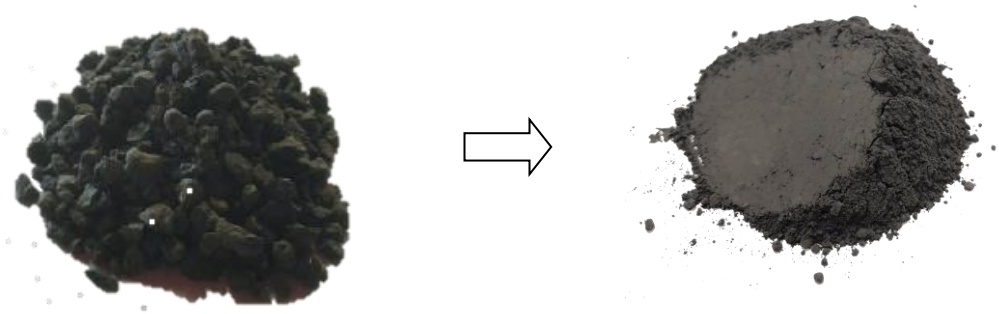

Figure 18: EAF-slag as produced and as powder

The chemical compositions of the EAF slag was determined by energy dispersive spectroscopy (EDS) analysis. Through the analyzes it was possible to notice that the slag is rich in calcium (Ca), iron (Fe) and silica (Si) with some other minor oxides in its composition. Chemical compositions of steel slag are shown in Table 5. EDS analysis was done using a Hitachi S-4800 scanning electron microscope. The microscope was operated at 15 kV at a working distance of 7.1 mm. Specimens were examined for EDS using a cooled Bruker Xflash 5010 with Peltier resolution ≤ 129 eV of Mn.

Table 5: EAF-slag chemical compositions

Oxides	Oxides percentage by mass (%wt)
CaO	34,2
SiO2	13,9
Al2O3	12,0
MgO	4,1
Cr2O3	2,7
MnO	4,0
Fe2O3	29,1
Density (g/cm3)	3,82

5.1.2 Portland cement

The chemical compositions of Portland cement were determined by energy dispersive spectroscopy (EDS) analysis. Through the analyzes it was possible to confirm that Portland cement is also rich in calcium (Ca) and silica (Si) with some other minor oxides in its composition including iron (Fe). Chemical composition of Portland cement is shown in Table 6. EDS analysis was done using a Hitachi S-4800 scanning electron microscope. The microscope was operated at 15 kV at a working distance of 7.1 mm. Specimens were examined for EDS using a cooled Bruker Xflash 5010 with Peltier resolution ≤ 129 eV of Mn.

Table 6: Portland cement chemical compositions

Oxides	Oxides percentage by mass (%wt)
CaO	62,20
SiO2	12,31
Al2O3	3,08
MgO	1,27
SO3	4,33
Fe_2O_3	2,42
Density (g/cm3)	3,06

5.1.3 Biochar

Biochar is a type of charcoal produced from organic materials such as agricultural waste, wood chips, or other biomass through a process called pyrolysis. Pyrolysis involves heating the organic material in the absence of oxygen, resulting in the production of a stable form of carbon known as biochar, along with other byproducts such as bio-oil and syngas [110–112].

In the context of the study on CO2-activated EAF slag, biochar could serve as an additive aimed at enhancing certain properties of the mixture. Biochar is known for its high porosity and large surface area, which can potentially improve the overall porosity and water retention capacity of the composite material when added in appropriate proportions. Additionally, biochar may contribute to carbon sequestration when incorporated into construction materials, aligning with sustainability goals [110,113].

It originates from the pyrolysis of biomass under low or anaerobic conditions. Biochar typically exhibits a low H/C and O/C ratio, which serves as an indicator of its high chemical stability and extensive carbonization. Furthermore, it has substantial specific surface areas, large pore volumes and excellent absorption capacity [110–112].

Its inherent potential for carbon sequestration positions it as an appealing additive with the capacity to make a significant contribution to climate change mitigation. Consequently, it holds considerable promise for use in the construction industry [110]. Studies have shown that the addition of biochar to Portland cement mortar significantly increases compressive strength, as well as other characteristics such as reduced thermal conductivity [110–112].Based on these

findings, this research incorporates biochar in a small portion, in some specimens, to analyze the CO2 absorption and thermal conductivity of the specimens.

5.1.4 River Sand

The chemical compositions of river sand were determined by energy dispersive spectroscopy (EDS) analysis. The chemical compositions of river sand are shown in Table 7. EDS analysis was performed using a Hitachi S-4800 scanning electron microscope. The microscope was operated at 15 kV at a working distance of 7.1 mm. Specimens were examined for EDS using a cooled Bruker Xflash 5010 with Peltier resolution ≤ 129 eV of Mn.

Table 7: River sand chemical compositions

Oxides	Oxides percentage by mass (%wt)
CaO	1,4
SiO2	76,5
Al2O3	13,2
MgO	0,7
Na2O	3,3
Fe2O3	1,6
Density (g/cm3)	2,6

5.2 Methods

5.2.1 Sample manufacturing

The EAF slag was finely ground to a particle size of 125 micrometers in order to serve as a binder. Additionally, for its use as an aggregate, the EAF slag was sieved and categorized into three distinct particle size ranges: 0.5 to 1 mm (fine grain size A), 1 to 2 mm (medium grain size C), and 2 to 4 mm (large grain size B).

The river sand to be used as aggregate was sieved and categorized into three different particle size ranges: 0.5 to 1 mm (fine grain A), 1 to 2 mm (medium grain C) and 2 to 4 mm. (large grain size B).

The mixtures were prepared with the materials mentioned in topic 1 of this chapter, according to the table 8, 9 e 10.

Table 8: Composition of mortars cured at 100% relative humidty (wt.%)

Mortar	Portland Cement (wt.%)	EAF-Slag (wt.%)	Coarse Sand (wt.%)	Water (wt.%)
HC15 (Portland cement with 15% water.)	34.32	0	52.63	13
HC12 (Portland cement with 12% water.)	29.17	0	60.10	10.73
HCE (Portland cement and EAF slag.)	13.18	16.57	60.15	10,10

Table 9: Composition of mortars cured by accelerated carbonation- 2 stage (wt.%)

Mortar	Portland Cement (wt.%)	EAF-Slag (wt.%)	Coarse Sand (wt.%)	Water (wt.%)
CE (EAF slag)	0	30	63	7.0
CEC (EAF slag and Portland cement)	14.3	16.7	60.0	8.0

Table 10: Composition of mortars cured by accelerated carbonation- 3 stage (wt.%)

Material	Biochar	EAF-Slag	EAF aggregates	River Sand	Water
1	-	36,82	-	55,77	7,41
2	0,16	36,76	-	55,68	7,40
3	-	28,98	63,61	-	7,41
4	0,13	28,95	63,52	-	7,40

The materials were mechanically mixed for approximately 3 minutes in a mechanical mixer, as shown in Figure 19, resulting in a homogeneous mixture and, subsequently, placed in cubic molds, according to the test measurements.

Figure 19: mechanical mixer

Five specimens were manufactured for each mixture through a static compression process. During this process, a constant compaction pressure of 30 MPa was applied to the upper surface of each specimen. Once the target pressure was reached, it was maintained for a period of 60 seconds. This step was performed to optimize the arrangement of particles within the specimens, following the static matching sequence illustrated in Figure 20.

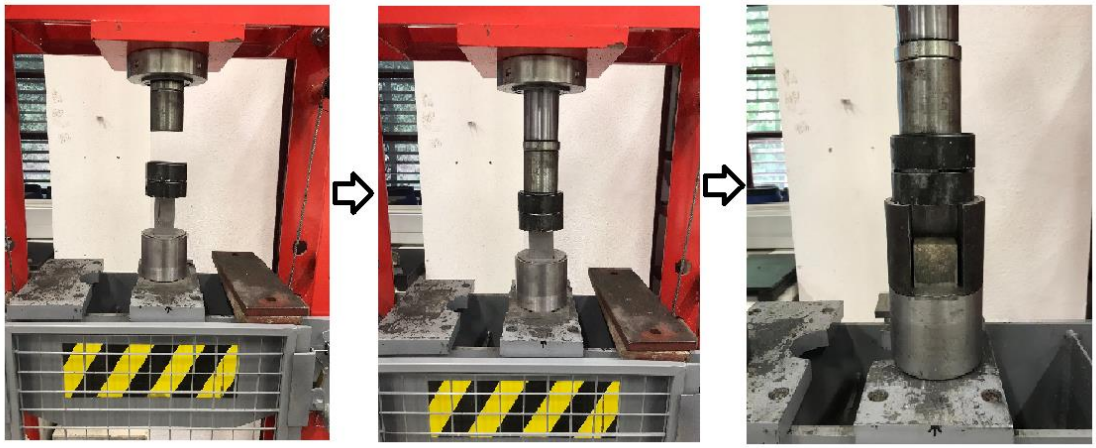

Figure 20: The static compression process.

The table 11 shows the size and shape of the specimens used for each test in this research.

Table 11: The size and shape of the specimens

Specimens size (cm)	Test
4 x 10 x 4	Thermal conductivity Thermal expansion Thermal energy storage
18.7 x 4 x 19	Dynamics thermal response and Thermal capacitance - (Test Box)
4 x 4 x 4	Compressive strength

For the Mercury Intrusion Porosimetry (MIP) test, cubic specimens (edges = 40 mm) were used. For Thermogravimetric Analysis (TGA) and Differential Scanning Calorimetry (DSC), specimens were sieved to obtain a finer material with particle sizes smaller than 63 micrometers.

5.2.2 Curing process

After static compression, specimens of the HC12, HC15 and HCE mixtures were taken to the hydration curing chamber for 28 days with a relative humidity of 90% and a temperature around 20°C. The other specimens were subjected to a 24-hour curing period with CO_2 in a controlled atmosphere inside a carbonation chamber, Figure 21 , which had a concentration CO_2 of 99% and partial pressure of 0.9 bar, with a temperature of 60°C and also relative humidity of 80%.

Figure 21: The accelerated carbonation chamber developed at UBI.

After curing, the specimens were placed in an oven for 24 hours at a temperature of 60˚C, Figure 22. This procedure was implemented to stabilize the chemical reaction that occurs during the accelerated carbonation process.

Figure 22: Oven used for stabilization of cured specimens.

5.2.3 Differential scanning calorimetry (DSC)

The differential scanning calorimeter (DSC) experiment was performed using the Netzsch brand and the model DSC 204 Phoenix, which allows temperature measurements between 0 ºC and 500 ºC. The experiment was conducted in the Opticar Center at UBI, Figure 23.

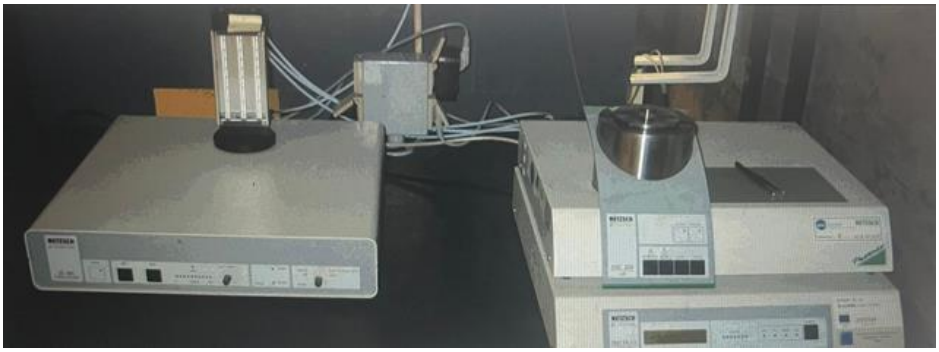

Figure 23: DSC 204 Phoenix at Opticar Center of UBI

Throughout the experiment, all specimens of the four mortars were tested in aluminum crucibles with a nitrogen atmosphere that had a flow rate of 50 mL/min. To perform the thermal cycles and the heating, three different heating rates were considered: 2°C/min, 4°C/min, and 6°C/min.

To perform the DSC test procedure, four steps were followed for each of the four specimen types (CE, CEC, HCE, HC12, and HC15). The first step is the initial isothermal period at 5°C, lasting 5 minutes. The second step is the dynamic heating up to 40°C according to the previously determined rates. The third step is stabilization at 40°C for 5 minutes [114,115].

5.2.4 Compressive strength

The compressive strength tests were carried out after curing. The tests were carried out in the construction technology laboratory of UBI in an ELE 3000kN hydraulic press with Digital Reading, Figure 24. Test specimens with dimensions of 4×4×4 cm were subjected to compression and were tested in accordance with the standard EN 1015-1 [116].

Figure 24: ELE 3000kN hydraulic press at construction technology laboratory of UBI

The specimens were placed on the lower plate of the press, centered, ensuring the perpendicularity of the compression forces applied to the upper face of the specimen in contact with the mold. The load rate used in the tests was 0.05 kN/s and the compressive strength values were obtained by the formula: $\sigma = F/A$, where σ is the rupture stress in MPa, F is the compression force that the body test resists in kN and , A, the area of the sample in mm2.

5.2.5 Mercury intrusion porosimetry (MIP)

The mercury intrusion porosimetry test determines the volume and distribution of the average diameter of the mortar pores. This analysis was carried out using the “Micromeritics AutoPore IV 9500” equipment from the materials characterization and evaluation (MCE) laboratory of UBI, Figure 25. This instrument allows the determination of void volumes corresponding to average pores between 6 and 0.01 μm, and pressure variation from atmospheric pressure values up to 33000 psi (228 MPa). In each measurement, the test was carried out in two stages. The

first stage is the low pressure stage with the pressure ranging from 0 to 0.14 MPa. The second stage is the high pressure stage. Testing was carried on according to ASTM D4404 standard.

Figure 25: Micromeritics AutoPore IV 9500" of MCE laboratory

5.2.6 Thermogravimetric analysis (TGA)

The Thermogravimetric analysis or TGA (Thermogravimetric Analysis) aims to analyze the mass losses of each specimens when subjected to high temperatures. In this research, the equipment used was the TGA Q50 from TA Instruments, which is located in the construction laboratories of MCE laboratory at UBI, Figure 26.

Figure 26: TGA Q50 from TA Instruments of MCE laboratory

This test consists of subjecting a small amount of powder from a specimen, between 5-8 mg, to an increasing temperature until reaching 1000 ^{0}C, with a constant temperature increase of 20 ^{0}C/min. In the end, of test the results come in the form of a graph showing the total loss of mass, as well as the variations in mass over time. Testing was carried on according to ASTM E1131 standard.

The thermal behavior of the specimens allows the identification and quantification of the dehydration, dehydroxylation and decarbonation processes, as well as mass gain (for example, carbonation and oxidation), obtaining additional information about the carbonation products[117].

The TGA test determined the amount of CO2 adsorbed during accelerated carbonation. The TGA test results were used to calculate the degree of carbonation (CD) representing the amount of CO2 adsorbed by the specimens. The calculation used Eq (4) based on the mass loss observed in the temperature range from 550 to 1000°C.

$$CD(\%) = \frac{[C - C_0]}{[C_{max} - C_0]} \text{ x } 100 \qquad \text{Eq(4)}$$

In Eq (1), C represents the amount of CO2 present in the carbonated specimens, Co denotes the initial amount of CO2 in the specimens before carbonation, and Cmax corresponds to the theoretical amount of CO2 needed to react with all the CaO present in the specimens, resulting in the formation of CaCO3.

Eq (5) [118] describes how to obtain the Cmax. The amount of adsorbed CO2 was determined based on the mass loss observed in the temperature range from 550 to 1000°C [119][120].

$$C_{max}(\%) = 0{,}785CaO - 0{,}56\text{CaCO3} - 0{,}7SO3 + 1{,}091MgO + 0{,}71Na2O + 0{,}468K2O \qquad \text{Eq(5)}$$

The equation assumes that all compounds present in the cementitious matrix (such as CaO, MgO, Na2O, and K2O) undergo reactions with CO2, leading to the formation of carbonates [118,120].

5.2.7 Thermal expasion

The expansion coefficient test of the specimens was carried out in the MCE laboratories of UBI, Figure 27. The specimens that were subjected to this test were the 100% EAF-slag specimens and the specimens with Portland cement and river sand, with a particle size of 2 to 4 mm. Thos test was carried on according to ASTM E831 standard.

Figure 27: Thermal expansion test of MCE laboratory

The specimens were measured in length, width and height using a millimeter ruler and then placed in an oven at 60°C for 24 hours. After the set time, the specimens were removed from the oven and the dimensions were measured again with a millimeter ruler. With the measurements obtained, the coefficient of thermal expansion (CT) was calculated using Equation 6, which considers the variation in the length of the specimens as a function of temperature.

$$\mathbf{CT} = \frac{\frac{(\Delta \mathbf{L})}{\mathbf{L0}}}{(\Delta \mathbf{T})} \qquad \text{(Eq 6)}$$

Where ΔL is the length variation, L0 is the initial length and ΔT is the room temperature variation.

5.2.8 Thermal energy storage

The thermal energy storage test of the specimens was carried out in the MCE laboratories of UBI. The specimens that were subjected to this test were the 100% EAF-slag specimens and the specimens with Portland cement and river sand, with a particle size of 2 to 4 mm.

To determine the temperatures of the specimens, an ETEKCITY Lasergrio 774 infrared thermometer (-50°C to 389°C range) was utilized, Figure 28. Temperature measurements were taken for each specimens before it entered the oven, at the conclusion of the oven cycle, and at intervals of 15, 30, 45, and 60 minutes after removal from the oven.

Figura 28: ETEKCITY Lasergrio 774 infrared thermometer of MCE laboratory.

5.2.9 Thermal conductivity

The thermal conductivity of the small specimens (4 x 10 x 4 cm) was measured using the selected Transient Line Heat Source method, using the KD2 Pro equipment from METER GROUP (Pullman, USA) at the University of Lleida in Spain, Figure 29.

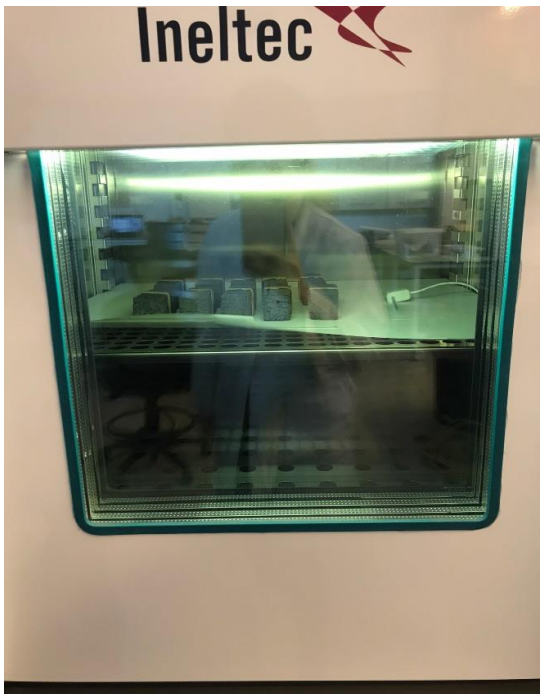

Figure 29: KD2 Pro equipment from METER GROUP of UDL laboratory.

The RK-3 needle was used, which has a diameter of 3.9 mm and a length of 60 mm. Measurements were carried out keeping the specimens at different temperatures: 20 ºC, 30 ºC, 40 ºC and 50 ºC, Figure 30. At least six repetitions were made at each temperature for each sample, and the average of the 4th, 5th and 6th measurements was calculated in all cases. Each

measurement lasted 1 minute and the time interval between two consecutive measurements was 15 minutes. This test was carredi on according to ASTM E1530 standard.

Figure 30: Thermal conductivity test of UDL laboratory.

5.2.10 Dynamics thermal response and thermal capacitance - (Test Box)

The characterization of the thermal behaviour of the large specimens (18.7 x 4 x 19 cm) was performed using a home-made thermal behaviour analyser, also known as Test Box, developed at the University of Lleida [121]. This test was carried on according to ISO 13786 standard.

A schematic view of the equipment is shown in Figure 31.

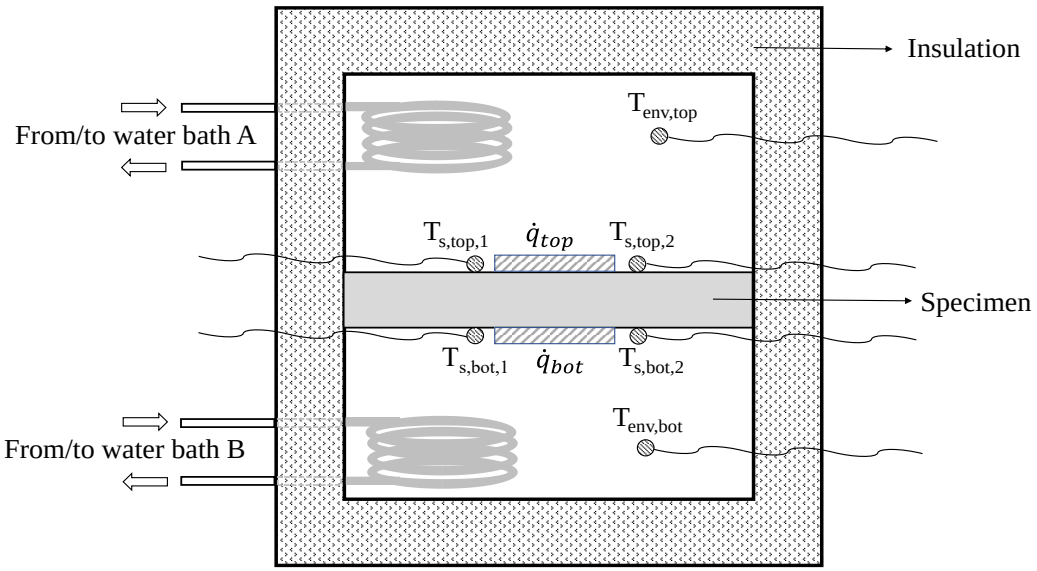

Figure 31: Schematic of the Test Box equipment of UDL laboratory.

The sample is placed horizontally inside the Text Box and it separates two spaces that can be heated or cooled using one water bath connected to each space. Two temperature sensors and one heat flux sensor were located in close contact with each of the two surfaces of the sample. This allowed measuring the average surface temperature and heat flux through the sample.

Depending on the temperature profile applied in each water bath, the sample can be subjected to a constant temperature gradient, it can be heated from both surfaces, or it can be subjected to variable temperature conditions at one side. Therefore, the device allows calculating the thermal transmittance, the specific heat capacity, and analyse the dynamic thermal response of the sample, through dedicated experiments as explained below.

5.2.10.1 Thermal transmittance in steady-state conditions 1 Thermal transmittance in steady-state conditions -state conditions

The water baths connected to the top and bottom spaces were kept at constant temperatures of 20 ºC, and 50 ºC, respectively. When steady-state conditions are achieved, the temperature gradient through the sample is constant, which allows calculating the thermal transmittance of the sample (U, in W/m2·K) using Eq. (7):

$$U = \frac{\dot{q}}{T_{s,bot} - T_{s,top}} \qquad \text{Eq. (7)}$$

where $\dot{q}$ (in W/m2) is the average heat flux through the sample (calculated as the average of the values measured at the two surfaces) and $T_{s,bot}$ (in ºC) and $T_{s,top}$ (in ºC) are the average temperatures of the bottom and top surfaces, respectively (calculated as the average of the values measured by the two temperature sensors located at each surface).

5.2.10.2 Heat storage capacity

The water baths connected to the top and bottom spaces were kept at constant temperatures of 60 ºC and 50 ºC, respectively. In this way, a uniform heating of the sample was achieved, from an initial temperature of around 20 ºC up to around 45 ºC. This test was carried on according to ISO 13786 standard. The specific heat capacity of the sample (c_p, in J/kg·K) can be calculated using Eq. (8):

$$c_p = \frac{Q_{acc}}{m \cdot (T_f - T_i)} \qquad \text{Eq. (8)}$$

where Q_{acc} (in J) is the amount of heat accumulated in the sample, m (in kg) is the mass of the sample, and T_i (in ºC) and T_f (in ºC) are the initial and final temperatures of the sample,

calculated as the average of the values measured by the four temperature sensors in contact with the two surfaces of the sample.

The heat accumulated in the sample was obtained as shown in Eq. (9):

$$Q_{acc} = \Sigma(\dot{q}_{top} + \dot{q}_{bot}) \cdot A_s \cdot \Delta t \quad \text{Eq. (9)}$$

where $\dot{q}_{top}$ (in W/m2) and $\dot{q}_{bot}$ (in W/m2) are the heat fluxes that go into the sample from the top and bottom surfaces, respectively, A_s (in m2) is the area of the sample surface (18.7 cm × 19 cm), and $\Delta t = 1$ s is the time step between two consecutive measurements.

5.2.10.3 Dynamic thermal response

In this experiment, the water bath connected to the top space was programmed in such a way as to create high temperature variations along one day. With this, temperature oscillations between 15 ºC and 40 ºC could be achieved in the top space, similar to typical daily ambient temperature oscillations in summer. The lower space was kept under free floating conditions (the water bath was disconnected). Two complete daily cycles (i.e. 48 h) were performed for each sample. In this case, the delay between the peaks of the top space temperature and the heat flux at the bottom surface (time lag) was evaluated (Figure 33 (a)). In addition, the dampening of the temperature wave was also assessed in terms of the thermal stability coefficient, which was calculated as the ratio between the amplitudes of bottom (ΔTbot) and top (ΔTtop) surface temperatures (Figure 32(b)).

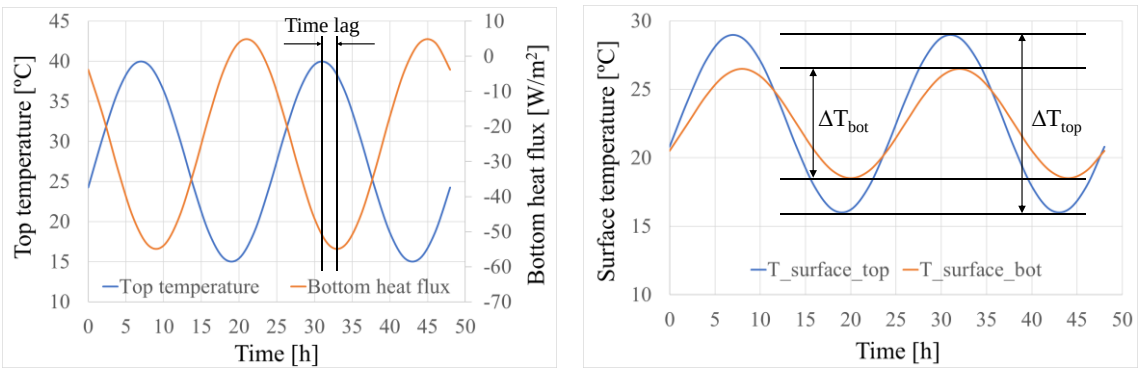

(a) (b)

Figure 32 :Schematic of the definition of (a) thermal lag and (b) thermal stability coeficiente.

Chapter 6-Results and discussion

6.1 Differential scanning calorimetry (DSC)

The DSC calorimeter test was carried out, which was used to subject the powders of CE (100% slag, cured by carbonation), CEC (50% slag and 50% cement, cured by carbonation), HCE (50 % slag and 50% cement, cured at 100% relative humidity), specimens HC12 (100% cement, 12% water and cured at 100% relative humidity) and HC15 (100% cement, 15% water and cured at 100% relative humidity) at three different temperature rates: 2°C/min, 4°C/min and 6°C/min. The graphs obtained show endothermic and exothermic peaks of each sample with the corresponding rate of temperature increase.

Starting with the CE specimen, the DSC graph (Figure 33) shows a variation of the DSC heat flux from 0.10 to -0.15 mW/mg at the three rates (2, 4, and 6 °C / min) obtained by this research up to the temperature of 40°C. The curves remained stable without much variation, with few endothermic and exothermic peaks. In contrast, the graph of the CEC specimen (Figure 34) showed a greater variation from 0.20 to -0.40 mW / mg at the three heating rates up to a temperature of 40°C. The graph showed more endothermic and exothermic curves compared to the CE sample.

The CE specimen's DSC graph showed a stable and less pronounced variation of heat flux, with few endothermic and exothermic peaks. On the other hand, the CEC specimen's DSC graph showed a more pronounced variation with more endothermic and exothermic peaks than the CE specimen.

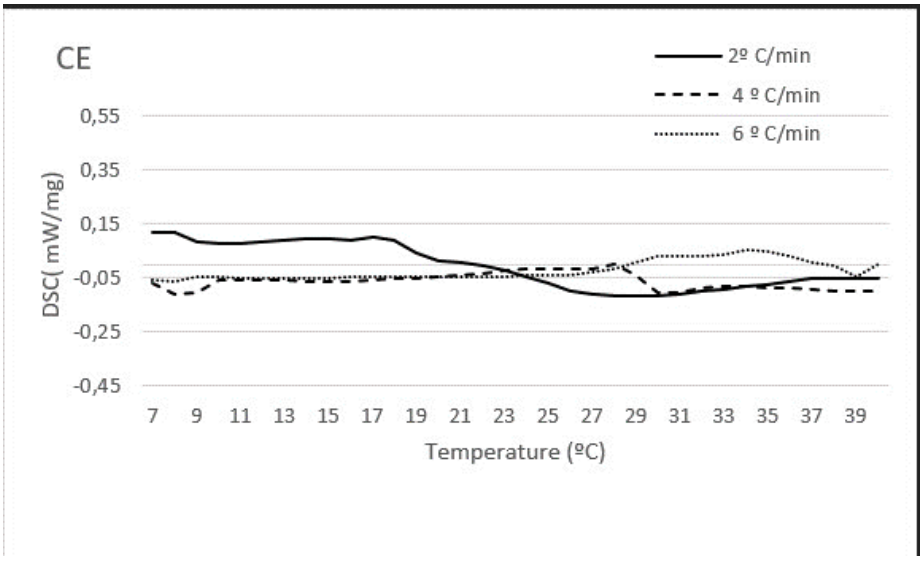

Figure 33: CE specimen DSC graph; 2°C/min (____), 4°C/min (-----), 6°C/min (.....).

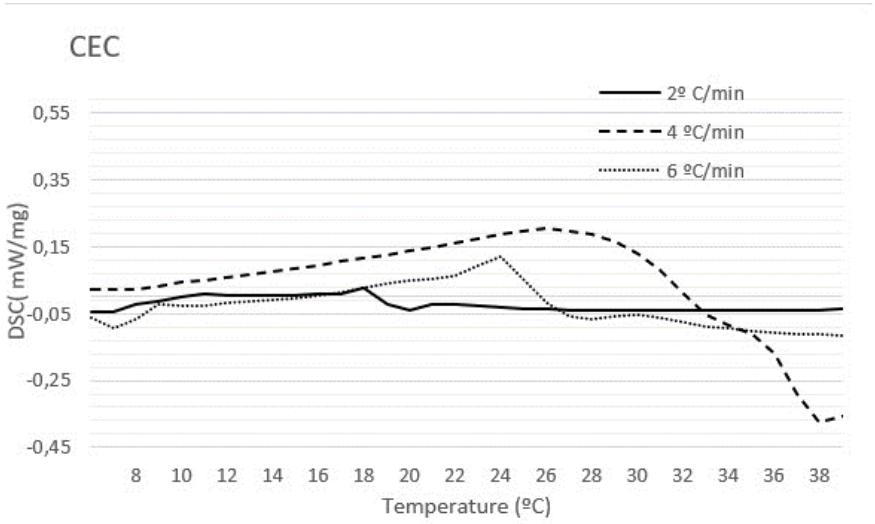

Figure 34: CEC specimen DSC graph; 2ºC/min (____), 4ºC/min (-----), 6ºC/min (.....).

The DSC graph of the HCE specimen (Figure 35) shows a variation of 0.08 to -0.13 mW/mg at all three heating rates up to 40ºC, like the CE sample. The curves remained stable, similar to the CE specimens. The graph of specimen HC12 (Figure 36) shows a variation of 0.40 to -0.20 mW/mg at all three rates up to 40ºC. The curves did not show much constancy, exhibiting endothermic and exothermic curves greater than the CE sample. Both DSC graphs of HCE and HC12 specimens showed greater variation than the CE sample with more endothermic and exothermic peaks.

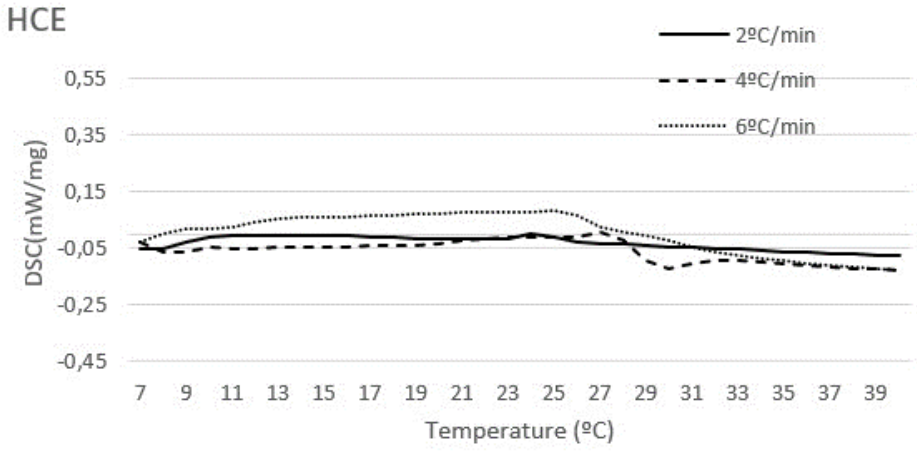

Figure 35: HEC specimen DSC graph; 2ºC/min (____), 4ºC/min (-----), 6ºC/min (.....).

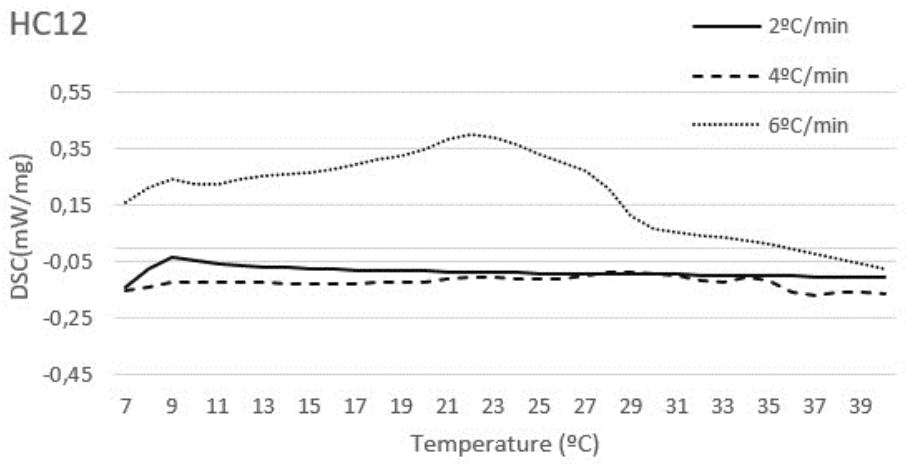

Figure 36: HC12 specimen DSC graph; 2ºC/min (____), 4ºC/min (-----), 6ºC/min (.....).

The DSC graph of the HC15 specimen (Figure 37) shows a variation of 0.60 to -0.20 mW / mg at the three rates up to the temperature of 40ºC. The curves showed a greater variation with a high exothermic peak.

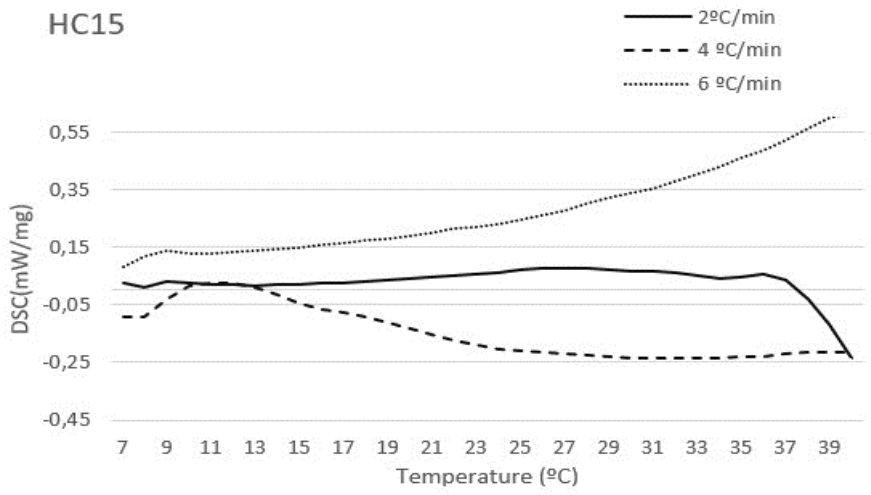

Figure 37: HC15 specimen DSC graph. ;2ºC/min (____), 4ºC/min (-----) 6ºC/min (.....).

When comparing all DSC graphs of all specimens at the heating rate of 2ºC/min (Figure 38), the curves varied from 0.10 to -0.30 mW/mg. The DSC graphs of HCE and HC12 specimens remained constant. The DSC graphs of the CE and HC15 specimens exhibited more variation, but the DSC graphs of the CE specimen with slag had an endothermic peak, while the CEC with slag and cement and the cement specimen (HC12) had an exothermic peak.

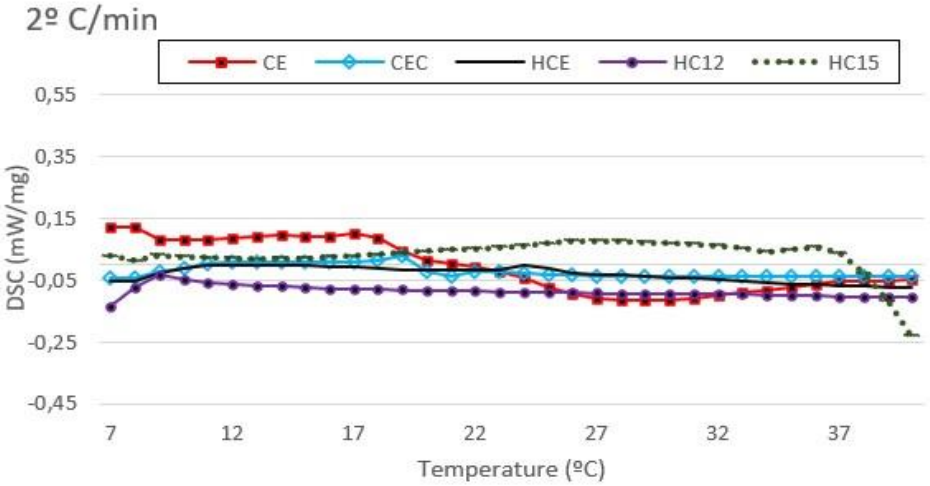

Figure 38: DSC graphs of all specimens at the heating rate of 2°C/min.

At the heating rate of 4°C/min (Figure 39), the DSC curves varied from 0.20 to -0.40 mW/mg. The DSC curves of the HCE and CE specimens were quite similar and constant. The DSC curve of the HC12 specimen was constant, and the DSC curve of the HC15 specimen obtained a small decline and then remained constant. The DSC curve of the CEC specimen obtained a more accentuated variation. The DSC curves of HCE and CE specimens, which contain slag, presented exothermic peaks from 25°C to 32°C. However, the DSC curves of the HCE and CE remained constant, and the DSC curve of the HCE specimen obtained an endothermic decline until -0.40 mW/mg.

Overall, the DSC analysis at a heating rate of 4°C/min indicated that the HCE and CE specimens containing slag had exothermic peaks in the temperature range of 25°C to 32°C, but their curves remained constant throughout the analysis. The HC12 sample had a constant curve, while the HC15 sample showed a small decline and then remained constant. The DSC graph of the CEC specimen had a more pronounced variation.

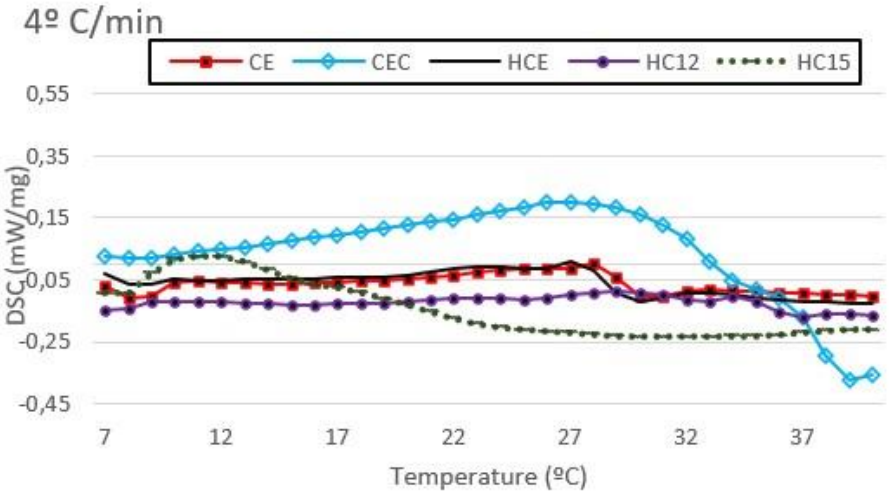

Figure 39: DSC graphs of all specimens at the heating rate of 4°C/min.

At a heating rate of 6°C/min in all specimens (Figure 40), the DSC heat flux curves showed variations ranging from 0.60 to -0.10 mW/mg. The DSC curves for the HCE, CEC, and CE specimens were similar and remained constant. Only the DSC curve of the CEC specimen obtained an exothermic peak at 25°C. On the other hand, the DSC curves of the HC12 and HC15 specimens showed greater variations, reaching 0.4 mW/mg for HC12 and 0.6 mW/mg for HC15. The slag specimens (HCE, CEC, and CE) showed constant DSC curves, while the cement specimens (HC12 and HC15) presented exothermic peaks.

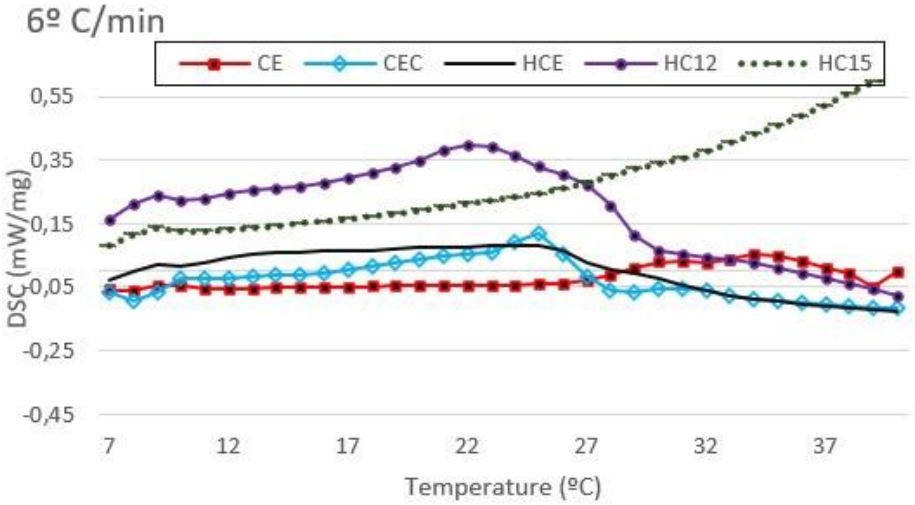

Figure 40: DSC graphs of all specimens at the heating rate of 6°C/min.

The graph in Figure 41 compares the DSC curves of the HCE and CEC specimens, showing that the DSC of the HCE specimen exhibited greater constancy than the DSC of the CEC specimen. At a temperature rate of 2 °C/min, the DSc curve of the HCE specimen remained stable while the DSC curve of the CEC specimen exhibited an exothermic peak of 0.04 mW/mg between 17-22°C. Similarly, at 4°C/min, the DSC curve of the HCE specimen remained stable, with only a small peak of 0.4 mW/mg at 26-29°C. In contrast, the DSC curve of the CEC specimen displayed an exothermic peak exceeding 0.20 mW/mg followed by an endothermic decline to -0.40 mW/mg. At a temperature rate of 6°C/min, both specimens obtained similar DSC results, but the DSC curve of the CEC sample exhibited a higher exothermic peak of 0.18mW/mw at 25°C.

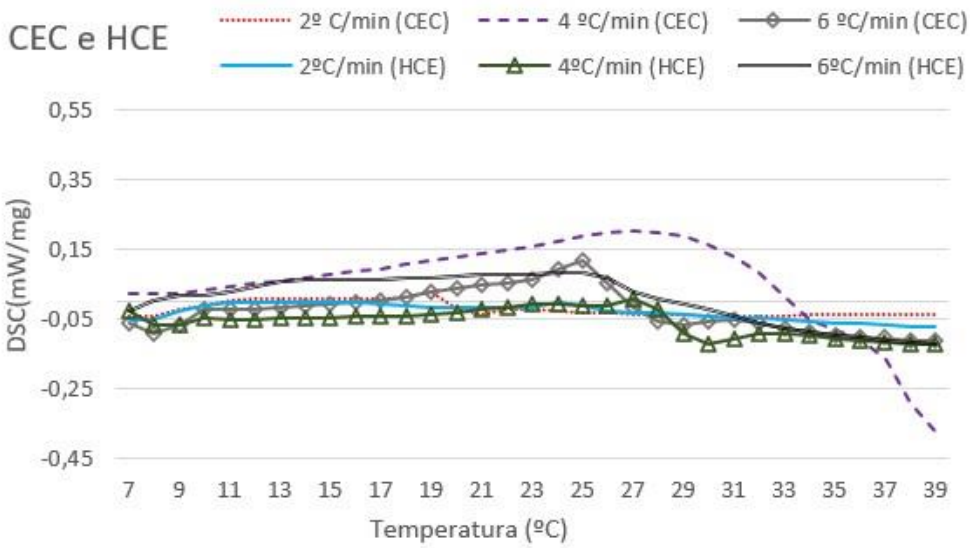

Figure 41: DSC graphs of HCE and CEC specimens.

The graph comparing the DSC curve of the HC12 and HC15 specimens (Figure 42) showed that the DSC curves for the HC12 specimen were constant at 2°C/min and 4°C/min, while those of the HC15 specimen showed less constancy and had a greater decline at 4°C/min compared to 2°C/min. At the rate of 6°C/min, the DSC curve of the HC12 specimen had a peak of up to 0.40 mW/mg and then remained constant, while the DSC curve of the HC15 sample continued to grow until reaching 0.6 mW/mg.

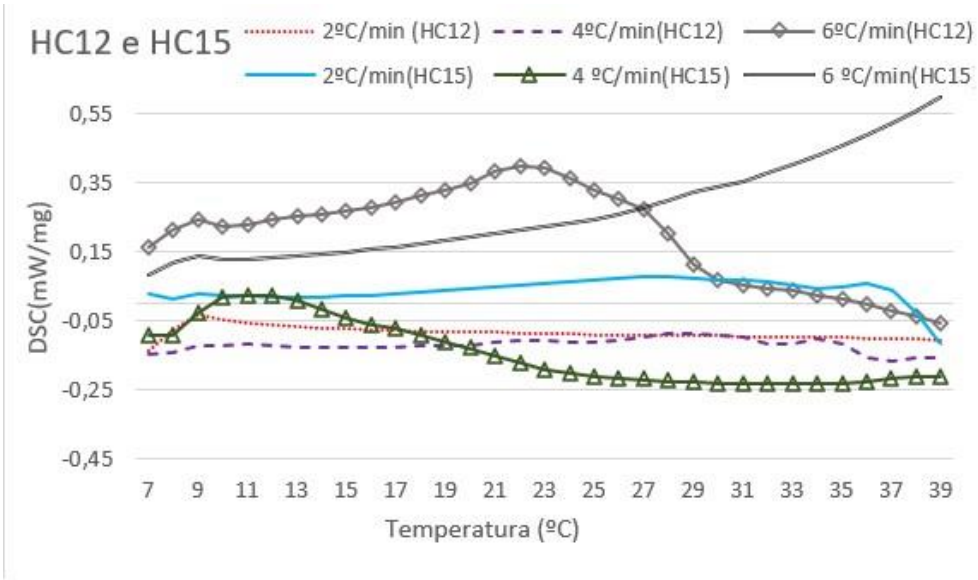

Figure 42: DSC graphs of HC12 and HC15 specimens

The Differential Scanning Calorimetry (DSC) results for five distinct powder specimens extracted from each mortar mix—CE (100% slag, accelerated carbonation), CEC (50% slag and 50% cement, accelerated carbonation), HCE (50% slag and 50 % cement, cured at 100% relative humidty), HC12 (100% cement, 12% water and cured at 100% relative humidty), and HC15 (100% cement, 15% water and cured at 100% relative humidty) —have been meticulously

presented and scrutinized. These specimens underwent heating at three different rates (2°C/min, 4°C/min, and 6°C/min), with their DSC heat fluxes recorded and compared.

The DSC graph of the CE specimen showed a stable and less pronounced variation of heat flux, with few endothermic and exothermic peaks. On the other hand, the DSC graph of the CEC specimen exhibited a more pronounced variation with more endothermic and exothermic peaks than the CE specimen. The DSC graphs of HCE and HC12 specimens showed greater variation than the CE specimen, with more endothermic and exothermic peaks. The DSC graph of the HC15 specimen exhibited a greater variation with a high exothermic peak.

Comparing all the DSC graphs of all specimens at a heating rate of 2°C/min, the DSC graphs of HCE and HC12 specimens remained constant. The DSC graphs of the CE and HC15 specimens exhibited more variation, but the DSC graphs of the CE specimen with slag had an endothermic peak, while the CEC with slag and cement and the cement specimen (HC12) had an exothermic peak.

At the heating rate of 4°C/min, the DSC curves of HCE and CE specimens, which contain slag, presented exothermic peaks from 25°C to 32°C. However, their curves remained constant throughout the analysis. The DSC curve of the HC12 specimen was constant, while the HC15 specimen showed a small decline and then remained constant. The DSC graph of the CEC specimen exhibited a more pronounced variation.

At a heating rate of 6°C/min in all specimens, the slag specimens (HCE, CEC, and CE) showed constant DSC curves, while the cement specimens (HC12 and HC15) presented exothermic peaks.

In terms of the endothermic and exothermic peaks observed in the DSC analysis, these represent the absorption or release of heat energy during heating or cooling, respectively. Endothermic peaks indicate energy absorption, while exothermic peaks indicate energy release.

The endothermic peaks observed in the DSC analysis of slag specimens may correspond to processes such as melting or phase transitions. For example, if the slag contains minerals that undergo a phase transition at a certain temperature, this may be reflected in an endothermic peak in the DSC analysis. Similarly, if the slag melts at a certain temperature, this may also result in an endothermic peak.

Differential Scanning Calorimetry (DSC) analysis of the mortar specimens revealed interesting insights into their thermal behavior. The DSC graph of the CE specimen, which contains 100% slag and was carbonation cured, showed a stable and less pronounced variation of heat flux, with few endothermic and exothermic peaks. This could be due to the slag phase transition temperature related to the amount of silica, alumina, and other oxides present. The stable DSC graph suggests that the slag has undergone its phase transition, and no further changes occurred.

The DSC graph of the CEC specimen, which contains 50% slag and 50% cement and was carbonation cured, exhibited a more pronounced variation with more endothermic and exothermic peaks than the CE specimen. This suggests that the carbonation process has caused more changes in the cementitious matrix of the CEC specimen compared to the CE specimen.

The DSC graphs of HCE and HC12 specimens, which contain 50% slag and 50% cement and were cured at 100% relative humidty, showed greater variation than the CE specimen, with more endothermic and exothermic peaks. This suggests that the cured at 100% relative humidty process has caused more changes in the cementitious matrix of HCE and HC12 specimens compared to CE specimen.

The DSC graph of the HC15 specimen, which contains 100% cement and was cured at 100% relative humidty, exhibited a greater variation with a high exothermic peak. This suggests that the cementitious matrix of the HC15 specimen is undergoing a significant change during the heating process, which could be due to the formation of new phases.

Since the DSC test data in the temperature range of 7°C to 29°C did not show many peaks, which are essential for determining thermal capacity, we used these analyses to evaluate the behavior of both the more stable and less stable samples as a preliminary study for future tests.

6.2 Compressive strength development

The Table 12 present the compressive strength results of specimens with EAF slag under all conditions studied.

The specimens with different types of aggregate and particle size were subjected to the compressive strength test after a period of 24 hours in the oven and subsequent cooling at room temperature. The results of this test are presented in Table 12, revealing that the greatest resistance was observed in specimens with particle sizes ranging from 1 to 2 mm, mainly in specimens made of 100% EAF material.

Table 12: Compressive strength results (MPa) for mortars with different granulometry

Granulometry (mm)	Specimens			
	1 (EAF slag and river sand.)	2 (EAF slag, river sand and biochar.)	3 (100% EAF slag)	4 (100% EAF slag and biochar)
A (0,5 to 1)	12,71	12,52	13,15	12,93
B (2 to 4)	16,55	17,25	11,20	13,90
C (1 to 2)	17,82	17,82	17,91	18,01

The compressive strength results indicate that mortar specimens with a 1 to 2 mm granulometry showed the highest strength values across all mixtures. Notably, the specimens containing 100% EAF material and EAF with biochar (specimens 3 and 4) exhibited enhanced compressive strength compared to the others, suggesting the potential of EAF material as a key contributor to improved mechanical properties.

These findings suggest that adjusting the granulometry of the aggregates and optimising the EAF material content could lead to even further improvements in the compressive strength of the mortar mixtures. There was no big difference in compressive strength with the addition of biochar to the specimens.

6.3 Mercury intrusion porosimetry (MIP)

The porosity assessment of all mortar specimens, subjected to accelerated carbonation, was carried out using MIP analysis. The results obtained for mortars with granulometry ranging from 0.5 mm to 1 mm (A) are summarised in Table 13.

Table 13: MIP results of granulometry 0,5 mm to 1 mm.

Mixture Label		1A	2A	3A	4A
Porosity (%)		25,32	28,15	32,16	33,18
Bulk Density at 14.50 psi (g/mL)		2,81	2,86	3,41	3,52
Apparent (skeletal) Density (g/mL)		3,34	3,44	4,31	4,36
Average Pore Diameter (μm)		0,15	0,15	0,15	0,16
Critical diameter (μm)		120,33	90,40	90,25	72,39
Pores typology	Mesopores (0.002 – 0.05 μm)	7,16 %	6,86 %	7,43%	7,09 %
	Macropores (0.05 μm – 10 μm)	47,52 %	44,32%	47,08%	39,84 %
	Air voids/cracks (> 10 μm)	45,32 %	48,82 %	45,49%	53,07 %

The test results revealed that mixtures containing 100% EAF-slag (specimens 3A and 4A) exhibited higher porosity than mixtures including river sand as an aggregate (specimens 1A and

2A). Adding biochar in certain mixtures increased porosity (specimens 2A and 4A) compared to specimens without this additive. Consequently, the utilisation of biochar and EAF-slag aggregate proved beneficial in producing cementitious matrices with a higher porosity index.

According to the International Union of Pure and Applied Chemistry (IUPAC) guidelines [122], the pore size diameter in a cementitious matrix can be classified as follows: (i) micropores (≤0.002 μm); (ii) mesopores (0.002 – ≤ 0.05 μm); (iii) macropores (0.05 μm – ≤ 10 μm); and (iv) voids/cracks (≥10 μm). Figure 43 depicts the curves illustrating the relationship between cumulative mercury intrusion (CMI) and pore size distribution for all the specimens. Remarkably, all the specimens exhibited a similar pore size distribution, indicating consistent porosity characteristics across the mixtures.

The critical pore diameter has direct implications for the material's permeability. When the larger interconnected pores have a considerable diameter, the material tends to be more permeable. Additionally, the critical diameter may be correlated with the effective porosity, which represents the fraction of pores contributing to fluid flow.

The critical pore diameter is essential for understanding the durability, permeability, and corrosion resistance of the material. A larger critical pore diameter can negatively impact durability, allowing greater penetration of aggressive agents, increasing susceptibility to freeze-thaw cycles, and promoting the formation of microcracks. Moreover, a larger critical pore diameter can affect corrosion resistance by facilitating the ingress of oxygen and chloride ions, reducing reinforcement protection, and accelerating carbonation.

Therefore, a larger critical pore diameter tends to negatively impact the material's durability, permeability, and corrosion resistance, ultimately leading to a reduced service life in aggressive environments.

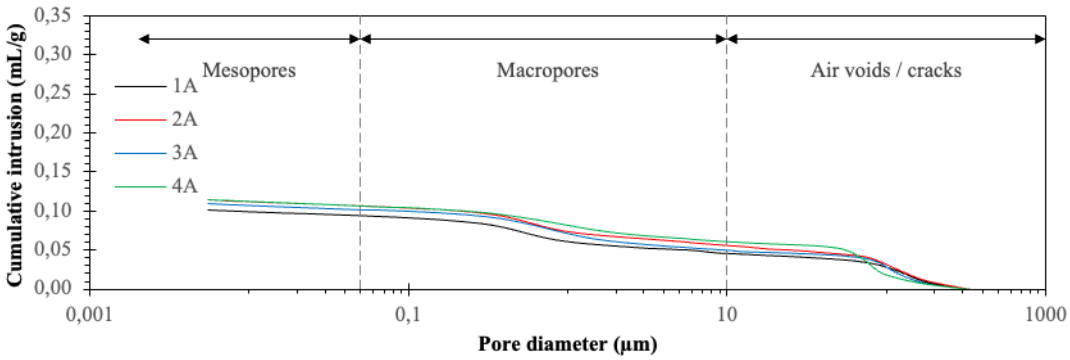

Figure 43: Cumulative mercury intrusion vs pore size diameter (mL/g) of granulometry 0,5 mm to 1 mm.

Based on these latest findings, the percentage of pores within specific diameter ranges (mesopores, macropores, or voids/cracks) was calculated for each aggregate mixture ranging

from 0,5 mm to 1 mm, as depicted in Figure 44. Interestingly, mixtures without the biochar, specifically 1A (7.16%) and 3A (7.43%), exhibited a higher percentage of mesopores compared to mixtures with biochar, namely 2A (6.86%) and 4A (7.09%). However, specimens containing 100% EAF-slag material demonstrated a higher percentage of mesopores, specifically 3A (7.43%) and 4A (7.09%).

These findings suggest that the presence of biochar in the mixtures can influence the pore distribution, leading to a slight decrease in the percentage of mesopores. On the other hand, using 100% EAF-slag as the binder and aggregate resulted in a higher proportion of mesopores, indicating a potential advantage regarding pore characteristics when using EAF-slag in the mixtures.

Conversely, when considering the pore typology of specimens with biochar , they displayed higher voids/cracks, with values of 2A (48.82%) and 4A (53.07%). Conversely, specimens without biochar exhibited a higher percentage of macropores, with 1A (47.52%) and 3A (47.08%). Notably, the specimens containing 100% EAF-slag material with biochar presented higher voids/cracks. The higher percentage of voids/cracks observed in the specimens containing 100% EAF-slag material with biochar can be attributed to biochar's internal porosity. The biochar itself is known to possess a unique internal porous structure. Introducing biochar likely creates a network of internal pores within the mortar, leading to a higher percentage of voids/cracks in the overall structure. These internal voids can provide additional pathways for CO2 permeability but enhance the overall porosity of the material. These internal voids serve as additional pathways for CO2 absorption, making the mixture more effective in capturing and retaining CO2.

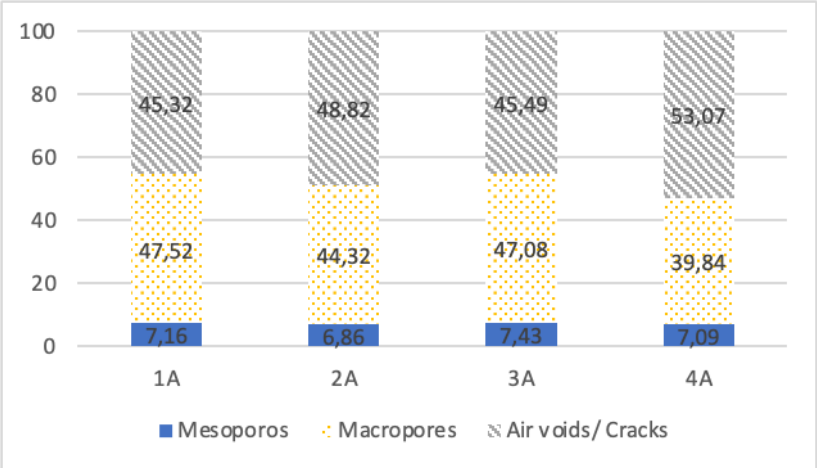

Figure 44: Pores typology (%) of specimens with granulometry 0,5 mm to 1 mm.

Regarding the critical diameter (Figure 45), All specimens with granulometry ranging from 0.5 mm to 1 mm displayed peaks within a similar range of pore diameters. The results indicate that the mixture of EAF-slag and river sand (1A) exhibited a higher value compared to the other mixtures (1A = 120.3 µm; 2A = 90.4 µm; 3A = 90.3 µm; 4A = 72.4 µm). The higher critical

diameter observed in the mixture containing EAF-slag and river sand (1A) could be attributed to the specific particle sizes and their distribution within the mixture.

The critical diameter refers to the diameter of the largest pores within the material, which is crucial in determining the material's permeability and transport properties. The composition of the EAF-slag and river sand (1A) mixture might have favoured the formation of larger pores compared to the other mixtures with different aggregate combinations.

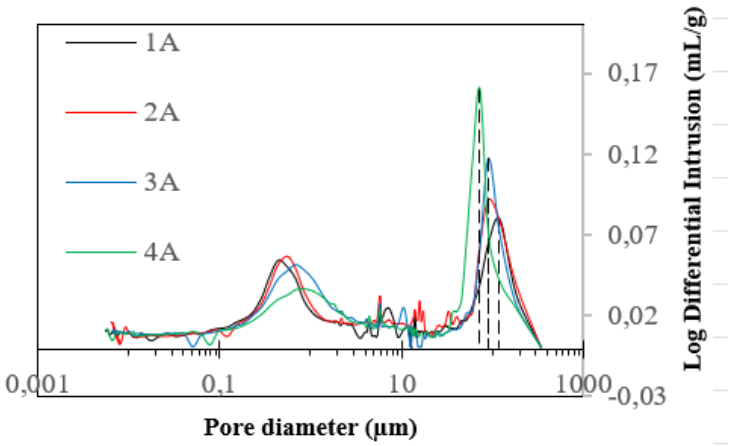

Figure 45: Specimens ' differential intrusion (mL/g) with granulometry 0,5 mm to 1 mm versus Pore diameter (µm).

The test results for mortars with granulometry ranging from 1 mm to 2 mm (C) are presented in Table 14. The table shows that mixtures containing 100% EAF-slag (3C and 4C) exhibited higher porosity than mixtures with river sand as an aggregate (1C and 2C). However, unlike the results observed for specimens with 0.5 mm to 1 mm granulometry, including biochar in certain mixtures (2C and 4C) led to reduced porosity compared to specimens without biochar (1C and 3C). This indicates that the effect of biochar on porosity can vary depending on the specific granulometry and composition of the mixture.

Table 14: MIP results of granulometry 1 mm to 2 mm.

Mixture Label	1C	2C	3C	4C
Porosity (%)	21,19	18,17	24,01	23,65
Bulk Density at 14.50 psia (g/mL)	2,87	2,93	3,53	3,52
Apparent (skeletal) Density (g/mL)	3,45	3,48	4,36	4,39
Average Pore Diameter (µm)	0,11	0,09	0,11	0,11

Critical diameter (µm)		0,43	0,35	0,43	0,55
Pores typology	Mesopores (0.002 – 0.05 µm)	9,48%	11,57%	9,79%	9,70%
	Macropores (0.05 µm – 10 µm)	62,68%	71,81%	61,98%	68,84%
	Air voids/cracks (> 10 µm)	27,84%	16,62%	28,23%	21,46%

The Figure 46 depicting the curves illustrating the relationship between cumulative mercury intrusion (CMI) and pore size distribution for all specimens with granulometry ranging from 1 mm to 2 mm (C) shows a striking similarity to what was observed in the graph of specimens with granulometry 0.5 mm to 1 mm (A). This similarity in pore size distribution curves suggests that the presence of biochar in the mixtures did not significantly affect the formation of pores within this granulometry range.

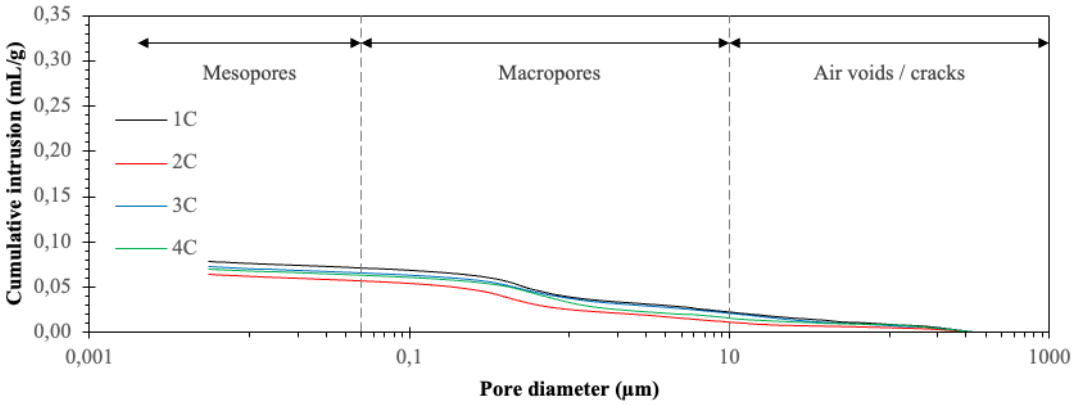

Figure 46: Cumulative mercury intrusion vs. pore size diameter (mL/g) of granulometry 1 mm to 2mm.

The analysis of the percentage of pores within specific diameter ranges (mesopores, macropores, or voids/cracks) for mortar mixtures with granulometry ranging from 1 mm to 2 mm (C), as depicted in Figure 47, revealed interesting trends. The mixtures containing the biochar and river sand aggregate, specifically 2C (11.57%), exhibited a higher percentage of mesopores compared to the other mixtures, namely 1C (9.48%), 3C (9.79%), and 4C (9.70%). This indicates that adding biochar led to an increase in the mesopore content of the mortar, potentially contributing to its improved properties and performance.

Conversely, the specimens without biochar, both the specimens with river sand aggregate (1C) and the sample with 100% EAF-slag material (3C), displayed a higher percentage of

voids/cracks, with values of 27.84% and 28.23%, respectively. In addition, the specimens with biochar (2C and 4C) exhibited a higher percentage of macropores, specifically 71.81% and 68.84%, respectively. This suggests that the presence of biochar in the mixture may have contributed to the formation of larger macropores.

These findings contrast the results obtained for specimens with a granulometry range of 0.5 mm to 1 mm (A), where a higher percentage of voids/cracks was observed. In the case of specimens with a granulometry range of 1 mm to 2 mm (C), they demonstrated a higher percentage of macropores in all the specimens. These differences in pore typology between the two granulometry ranges may be attributed to the variation in particle sizes and distribution within the mixtures, influencing the formation of different pore structures.

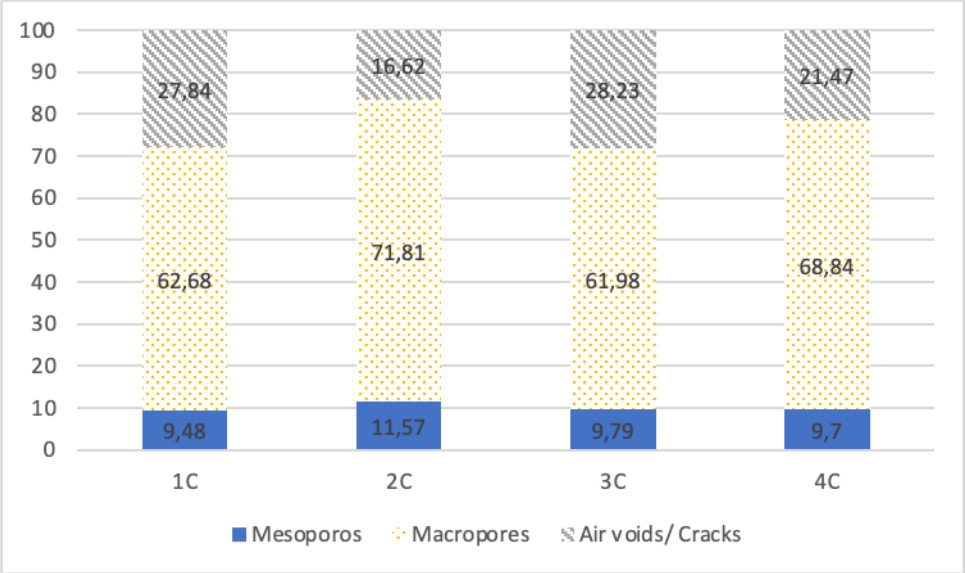

Figure 47: Pores typology (%) of specimens with granulometry 1 mm to 2mm.

The critical diameter analysis (Figure 48) reveals interesting findings for the mortar mixtures with granulometry ranging from 1 mm to 2 mm (C). The specimens consisting of 100% EAF-slag (4C) demonstrated a higher critical diameter compared to the other mixtures, with values of 0.55 µm, whereas the critical diameter values for the other mixtures were 0.43 µm for 1C, 0.35 µm for 2C, and 0.43 µm for 3C. This suggests that the mortar mixture with 100% EAF-slag material exhibited larger pore sizes than the other mixtures in this granulometry range.

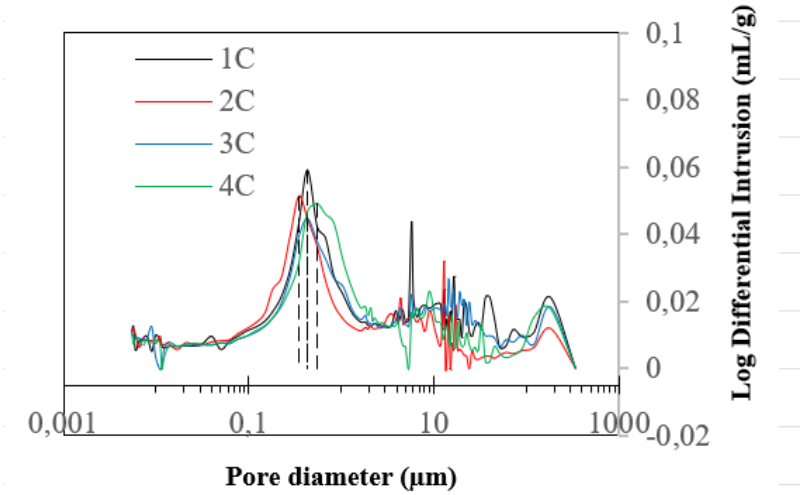

Figure 48: Specimens ' differential intrusion (mL/g) with granulometry 1 mm to 2 mm versus Pore diameter (µm).

Notably, all the specimens with grain sizes ranging from 1 mm to 2 mm displayed peaks within a similar range of pore diameters. However, these ranges were different compared to the specimens with grain sizes ranging from 0.5 mm to 1 mm. The specimens with the smallest granulometry (0.5 mm to 1 mm) obtained an interval between the diameters of the larger portions, indicating a variation in the pore size distribution between the two granulometry ranges. This difference in pore diameter distribution may be attributed to the varying particle sizes and packing characteristics of the aggregates used in the mixtures.

Table 15 summarizes the porosity and other parameters obtained for mortars with granulometry ranging from 2 mm to 4 mm (B). The results indicate notable variations in porosity among the different mixtures studied.

Table 15: MIP results of granulometry 2 mm to 4mm.

Mixture Label		1B	2B	3B	4B
Porosity (%)		20.00	16.09	21,15	22,85
Bulk Density at 14.50 psi (g/mL)		2,99	2,95	3,63	3,56
Apparent (skeletal) Density (g/mL)		3,50	3,42	4,38	4,42
Average Pore Diameter (µm)		0,12	0,08	0,10	0,11
Critical diameter (µm)		0,43	0,35	0,55	0,55
Pores typology	Mesopores (0.002 – 0.05 µm)	8,94%	13,23%	10,20%	9,97%

	Macropores (0.05 µm – 10 µm)	56,78%	66,81%	64,24%	70,50%
	Air voids/cracks (> 10 µm)	34,28%	19,96%	25,56%	19,53%

Mortar mixes containing 100% EAF-slag (3B and 4B) displayed slightly higher porosity values compared to mixes with river sand as the aggregate (1B and 2B). Specifically, specimens 3B and 4B exhibited porosity values of 21.15% and 22.82% porosity values, respectively, while specimens 1B and 2B had 20.00% and 16.09% porosity values, respectively.

Interestingly, the specimens with river sand aggregate and biochar (2B) demonstrated the lowest porosity among all the specimens investigated in this research, with a porosity value of 16.09%.

Figure 49 illustrates the relationship between cumulative mercury intrusion and pore diameter for all specimens with granulometry ranging from 2 mm to 4 mm. The specimens' curves exhibit a remarkable similarity, mirroring the trends observed in the graphs of the other specimens sets (A and C).

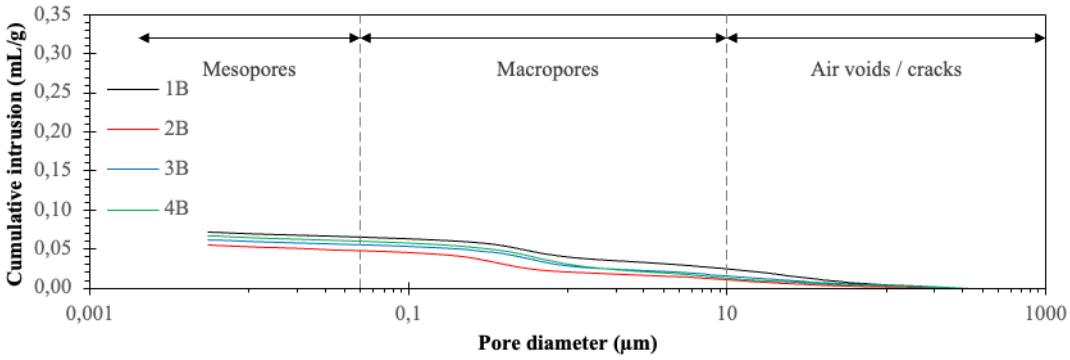

Figure 49: Cumulative mercury intrusion vs pore size diameter (mL/g) of granulometry 2 mm to 4 mm.

The consistent trends in the percentage of pores within specific diameter ranges across different granulometry ranges (1 mm to 2 mm and 2 mm to 4 mm) suggest that the composition of the mortar mixtures plays a significant role in determining pore characteristics. In both granulometry ranges, mixtures containing the biochar additive and river sand aggregate exhibited a higher percentage of mesopores than other mixtures.

The analysis of pore distribution within specific diameter ranges for each aggregate mixture ranging from 2 mm to 4 mm, as illustrated in Figure 50, revealed interesting trends like those observed in the granulometry range of 1 mm to 2 mm (C). Specifically, the mixture containing the biochar additive and river sand aggregate (2B) exhibited a notably higher percentage of

mesopores (13.23%) compared to the other mixtures, namely 1B (8.94%), 3B (10.20%), and 4B (9.97%).

Conversely, all specimens within the granulometry range of 2 mm to 4 mm demonstrated a higher percentage of macropores: 1B (56.78%), 2B (66.8%), 3B (64.24%), and 4B (70.5%). These results align with the findings obtained for specimens within the granulometry range of 1 mm to 2 mm (C), where a higher percentage of macropores was also consistently observed across all specimens.

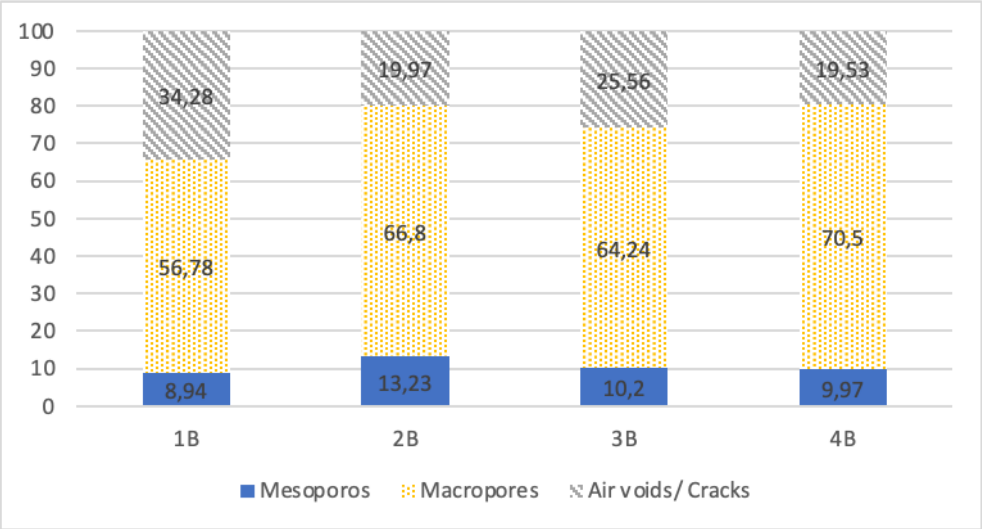

Figure 50: Pores typology (%) of specimens with granulometry 2 mm to 4 mm.

Concerning the critical diameter (Figure 51) obtained from the granulometry measurements between 2 mm to 4 mm, the results reveal that mixtures comprising 100% EAF-slag (3C) and 100% EAF-slag with biochar additive (4C) displayed higher values compared to the other mixtures (1C = 0.43 µm; 2C = 0.35 µm; 3C = 0.55 µm; 4A = 0.55 µm).

Additionally, the peak values of the pore diameters observed in the grain sizes from 2 mm to 4 mm were found to be in the same range as those in the grain sizes of 1 mm to 2 mm, further emphasising the consistency of these findings. However, it is noteworthy that the pore diameter ranges differed from the specimens with grain sizes ranging from 0.5 mm to 1 mm, indicating significant variations in pore structures between these two sets of specimens.

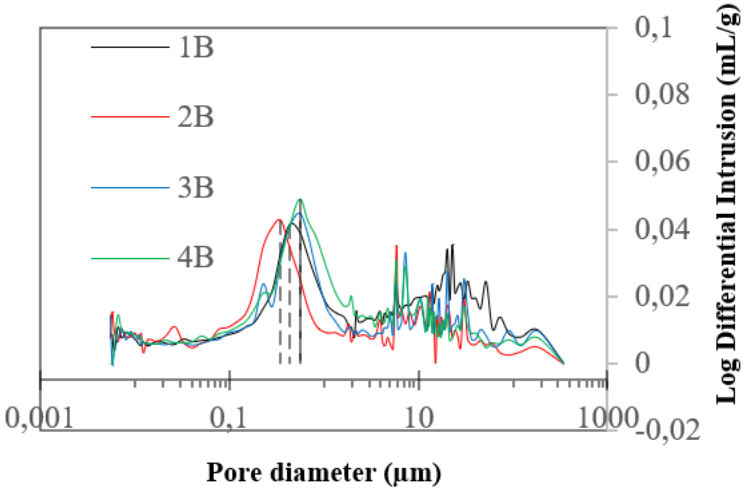

Figure 51: Specimens ' differential intrusion (mL/g) with granulometry 2 mm to 4 mm versus Pore diameter (µm).

6.4 Thermogravimetric (TGA) - CO2 absorption

The thermogravimetric test was conducted to measure the mass loss of each mixture when exposed to temperatures up to 1000 °C. The degree of carbonation (DC) was determined using the calculation method presented by Matsushita et al. [123]. This method utilizes the amount of CO2 in the carbonated sample (C), the amount of CO2 in the sample before carbonation (Co), and the theoretical amount of CO2 (Cmax) required to react with all the CaO in the mixtures, forming CaCO3 [118]. The amount of adsorbed CO2 (DC) was determined based on the mass loss observed between 550 and 1000°C [119][120].

It is important to note that while mortar, binder, and aggregate were used in this research to assess CO2 absorption, the specimens material with dimensions below 63 µm was predominantly composed of the binder. Since the aggregate's granulometry ranged from 0.5 mm to 4 mm, it can be assumed that the material below 63 µm is mainly EAF. Therefore, for the purpose of determining CO2 absorption, the majority of the powder obtained for testing originated from the binder. Consequently, Co, representing the initial amount of CO2 in the EAF-slag, was determined specifically for the EAF material.

The Co(%) value of the EAF-slag was obtained from the TGA graph before carbonation, and with these values, it was possible to calculate the Cmax (%) for each mixture, as presented in Table 16.

Table 16: CO2 Absorption Parameters

Mixture	Co(%)	Cmax(%)
EAF-Slag (specimens 1,2,3 and 4)	0.43	31.30

The determined Co(%) values for each EAF-Slag specimens are essential for understanding the CO_2 absorption process in the mixtures.

The thermogravimetric analysis (TGA) results indicate that the mass loss curves for all specimens exhibit a similar trend. The mass remained relatively constant with a small mass loss until reaching temperatures close to 450 °C. Afterwards, there was a sharp drop in the mass loss for all specimens, suggesting a common mechanism of decomposition.

Further examination of the differential thermogravimetric (DTG) graphs revealed that the highest peaks occurred at the same temperature of 727.94 °C for all specimens. This temperature corresponds to the decarbonisation of calcite ($CaCO_3$), a common occurrence within the temperature range of 700-900 °C [124]. Notably, the highest peaks were observed in specimens with 100% recycled content, combined with adding biochar. This finding indicates that the mixture containing 100% recycled material and biochar had the highest CO_2 absorption capacity.

Building on the TGA results, we could quantify the amount of CO_2 absorbed by the specimens after accelerated carbonation, utilising the method developed by Matsushita et al. [123]. This information provides valuable insights into the CO_2 absorption potential of the different mortar mixtures.

The DTG graphs revealed that the highest peaks, occurring at the temperature of 727.94 °C, were consistent across all specimens. This temperature corresponds to the decarbonisation of calcite ($CaCO_3$), a common occurrence in the temperature range of 700-900 °C [124]. Notably, the specimens containing 100% recycled material and the biochar exhibited the most prominent peaks, indicating a higher concentration of $CaCO_3$ and potentially a greater CO_2 absorption capacity. Through the TGA results, we could quantify the amount of CO_2 absorbed by the specimens after accelerated carbonation, employing the method introduced by Matsushita et al. [123].

Figure 52 displays the results for specimens with granulometry between 0.5 mm and 1 mm. The 100% recycled specimens, comprising EAF-slag as both binder and aggregate (specimens 3A and 4A), exhibited higher peaks in the DTG curve and more substantial mass loss in the TG curve. The highest peak was obtained by Sample 4A, which included the biochar.

These findings suggest that incorporating biochar and using 100% recycled materials, specifically EAF-slag as binder and aggregate, positively influence the CO_2 absorption capacity of the mortar mixtures.

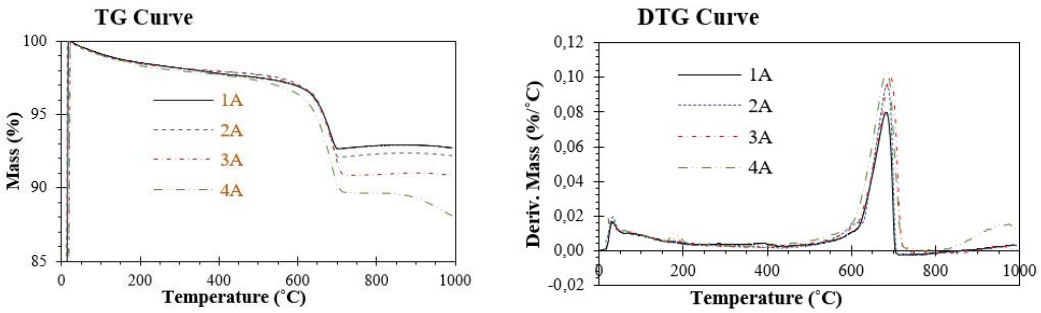

Figure 52: TG and DTG Curve of the granulometry 0.5 mm to 1 mm (A)

The TGA graphs of the mixtures provide valuable insights into their CO2 absorption behaviour. By analysing these graphs, we obtained the C (%) and DC (%) values for each sample, presented in Table 17. Among the specimens with granulometry ranging from 0.5 mm to 1 mm, the highest CO2 absorption capacity was observed in the sample containing 100% recycled materials and biochar (sample 4A).

Table 17: The values of C (%) and DC (%) of the granulometry 0.5 mm to 1 mm (A).

Specimens	C (%)	DC (%)
1A	7,98	24,45
2A	9,57	29,64
3A	10,05	31,16
4A	10,35	32,13

These results highlight the CO2 absorption potential of the mixtures containing 100% recycled materials, with EAF-slag serving as binder and aggregate. Adding the biochar additive further amplified the CO2 absorption capacity, leading to the highest absorption rate within this particular granulometry range (specimens 4A).

The TGA graphs for specimens with granulometry ranging from 1 mm to 2 mm (C) provided valuable insights into their CO2 absorption behaviour. As seen in Figure 53, the 100% recycled specimens with EAF-slag as binder and aggregate (specimens 3C and 4C) also exhibited higher peaks in the DTG curve and more substantial mass loss in the TG curve. The highest peak was observed in Sample 4C, which included the biochar, although the difference was insignificant compared to Sample 3C without biochar.

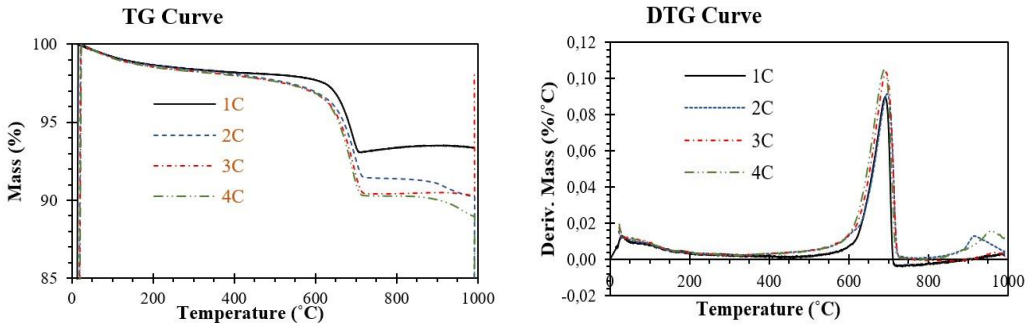

Figure 53: TG and DTG Curve of the granulometry 0.5 mm to 1 mm (A)

With the TGA graphs of the mixtures, we obtained essential parameters such as C (%) and DC (%), presented in Table 18. Among the specimens with granulometry ranging from 1 mm to 2 mm, the highest CO2 absorption capacity was observed in the 100% recycled sample with the biochar additive (sample 4C).

Table 18: The values of C (%) and DC(%) of the granulometry 1 mm to 2 mm (C).

Specimens	C (%)	DC (%)
1C	8,95	27,59
2C	9,16	28,27
3C	10,35	32,13
4C	10,50	32,62

The TGA graphs for specimens with granulometry ranging from 2 mm to 4 mm (B) provided valuable insights into their CO2 absorption behaviour. As depicted in Figure 54, the 100% recycled specimens with EAF-slag as binder and aggregate (specimens 3B and 4B) also displayed higher peaks in the DTG curve and more substantial mass loss in the TG curve. However, like previous observations, the highest peak was achieved in sample 4B, which included the biochar, although the difference compared to sample 3B without biochar was not substantial.

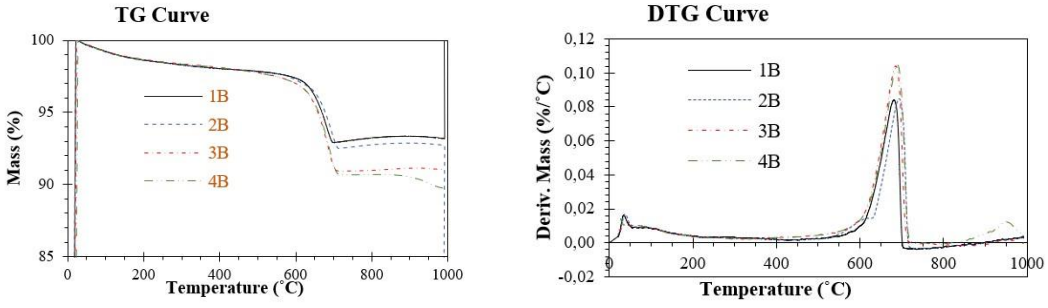

Figure 54: TG and DTG curve of the granulometry 2 mm to 4 mm (B).

The results from the granulometry range between 2 mm and 4 mm, shown in Table 19, further validate the significant CO2 absorption potential of the 100% recycled mixtures, especially those containing EAF-slag as both binder and aggregate. Once again, the inclusion of the biochar (sample 4B) resulted in the highest CO2 absorption rate within this specific granulometry range.

Table 19: The values of C (%) and DC(%) of the granulometry are 2 mm to 4 mm (B).

Specimens	C (%)	DC (%)
1B	8,40	25,82
2B	8,47	26,04
3B	10,41	32,33
4B	10,47	32,52

In summary, our analysis of the TGA test results and CO2 absorption calculations clearly indicates that the mortar specimens composed of 100% EAF-slag combined with biochar demonstrated the highest levels of CO2 absorption across all granulometry ranges. Notably, among the different granulometry sizes, the specimens with a size range of 1 to 2 mm exhibited the highest amount of absorbed CO2.

6.5 Thermal expasion.

Thermophysical characteristics of the mortars were investigated through material thermal expansion tests, which allowed the determination of the expansion and coefficient of thermal expansion of the specimens and their heat absorption capacity. The average dimensions of the specimens (length, width, and height) before and after 24 hours in the oven, as well as the linear thermal expansions, were recorded and presented in Table 20. Notably, the EAF-slag specimens showed a greater expansion compared to Portland cement specimens.

Table 20: Specimens' length, width and height due to thermal expansion.

Mortar	Length (cm)			Width (cm)			Height (cm)		
	Lo	L	ΔL	Wo	W	ΔW	Ho	H	ΔH
EAF1	15,93	16,05	0,12	4,10	4,16	0,06	4,40	4,45	4,45
EAF2	15,95	15,95	15,95	15,95	15,95	15,95	15,95	15,95	15,95
EAF3	15,94	15,94	15,94	15,94	15,94	15,94	15,94	15,94	15,94
PC1	15,93	15,93	15,93	15,93	15,93	15,93	15,93	15,93	15,93
PC2	15,85	15,85	15,85	15,85	15,85	15,85	15,85	15,85	15,85
PC3	15,88	15,88	15,88	15,88	15,88	15,88	15,88	15,88	15,88

Note: Lo, Wo and Ho represent the initial length, width and height of the specimens before the test, while L, W and H represent the specimens' length, width and height after the test. The notation $^{\Delta}$L, $^{\Delta}$W and $^{\Delta}$H represent the specimens' length, width and height change due to thermal expansion.

To calculate the coefficient of thermal expansion, we used the initial length of the specimens, the variation of their length, the ambient temperature before the oven, and the oven temperature. Table 21 shows the Coefficient of Thermal Expansion (CT) calculated for both EAF-slag and Portland cement mortars. The EAF-slag mortar presented a higher CT value than the Portland cement mortar, indicating that the former is more susceptible to thermal expansion upon exposure to high temperatures.

Table 21: Coefficient of thermal expansion.

Mortar	Lo (cm)	ΔL (cm)	To (°C)	CT (cm/cm °C)
EAF	15,94	0,11	22	18,16 10-5
PC	15,85	0,05	22	8,30 10-5

The results of the experiments showed that the thermal expansion characteristics of EAF-slag mortars are higher than those of Portland cement mortars. Specifically, the 100% EAF-slag mortars have more than double the expansion of Portland cement mortars, with EAF at 0.11 cm and PC at 0.05 cm. The coefficient of thermal expansion was also higher for EAF-slag at 18.16 10-5 (cm/cm °C) compared to Portland cement at 8.30 10-5 (cm/cm °C). These findings were expected, as the chemical composition of EAF contains a greater amount of metallic materials and has a darker colour, which allows for greater heat absorption.

6.6 Thermal energy storage.

The thermal energy storage of the specimen was also investigated by measuring their temperatures before and after 24 hours in the oven. Table 22 shows the data obtained in the first, second, and third cycles of the specimens. The EAF-slag specimens consistently presented a higher temperature than the Portland cement specimens, both before being placed in the oven and after 24 hours of exposure. Furthermore, the EAF-slag specimens could absorb more heat from the environment than the Portland cement specimens, as evidenced by their higher temperature rise. Notably, the EAF-slag specimens reached a temperature closer to the temperature of the kiln (60 °C), whereas the Portland cement specimens showed a lower temperature increase.

Table 22: temperature of the specimens before and after 24 hours in the oven.

Mortar	To 1C (°C)	Tf 1C (°C)	To 2C (°C)	Tf 2C (°C)	To 3C (°C)	Tf 3C (°C)
EAF1	21,5	57,0	22,0	57,0	22,2	57,1
EAF2	20,9	57,5	21,6	57,4	21,8	57,5
EAF3	21,0	57,3	21,4	57,4	21,4	57,3
PC1	19,6	51,5	20,1	51,4	20,6	51,5
PC2	19,7	51,7	19,9	51,8	20,2	51,8
PC3	20,1	52,0	20,3	52,1	20,4	52,0

Table 23 presents the average temperatures of three cycles for 15, 30, 45, and 60 minutes. The data shows that the EAF cement specimens had higher temperatures than the Portland cement specimens in all circumstances, indicating that EAF-slag is a material that absorbs more heat for temperature rise. Additionally, both cement and EAF-slag specimens experienced a greater temperature drop in the first 15 minutes, with the temperature drop decreasing as the specimens approached room temperature.

Table 23: the average temperatures of the 3 cycles for 15, 30, 45 and 60 minutes

Mortar	TF (°C)	T15 (°C)	T30 (°C)	T45 (°C)	T60 (°C)
EAF1	57,0	40,5	33,4	29,3	26,3
EAF2	57,5	41,0	33,7	29,6	26,4
EAF3	57,3	40,8	33,8	29,6	26,5
PC1	51,5	33,9	27,7	24,5	23,3
PC2	51,7	34,1	28,2	26,2	24,2
PC3	52,0	34,3	28,2	26,2	24,2

In Figure 55 displays the average temperature of the EAF-slag and Portland cement specimens measured at different time intervals after they were subjected to 60 °C for 24 hours in the oven. As previously mentioned, the data clearly indicate that the EAF-slag specimens consistently exhibited higher temperatures than the Portland cement specimens across all time points.

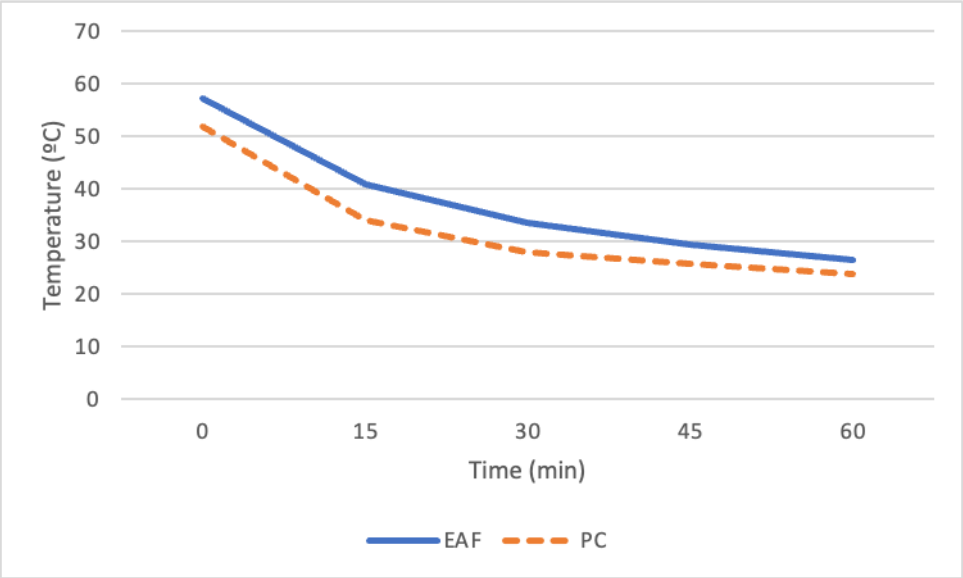

Figure 55: The average temperature of the EAF-slag and Portland cement specimens measured at different time intervals after they were subjected to 60 °C for 24 hours in the oven.

Furthermore, the EAF-slag mortars showed higher temperatures than Portland cement at room temperature in spring, with EAF-slag specimens recording temperatures of 20.9 °C and Portland cement specimens recording temperatures of 18.8 °C at an ambient temperature of 22 °C. These results suggest that EAF mortar is worth further research on its thermal insulation properties.

In summary, the results of our study suggest that EAF-slag mortars have a higher coefficient of thermal expansion and heat absorption capacity compared to Portland cement mortars. These discoveries have important implications for the use of EAF-slag in passive solar energy storage applications in buildings, where knowledge of the thermophysical properties of the material is essential to ensure its greater performance, durability and reliability in various environmental conditions.

6.7 Thermal conductivity and thermal transmittance.

The values of the thermal conductivity obtained using the small specimens and the Transient Line Heat Source method are summarised in Table 24.

Table 24: Thermal conductivity according to the Transient Line Heat Source method (values in J/m·K).

		Granulometry		
Material	Temperature (ºC)	A (0,5 to 1 mm)	C (1 to 2 mm)	B (2 to 4mm)
(EAF slag and river sand.)	20	0.650	1.365	1.784
	30	0.624	1.377	1.768
	40	0.609	1.387	1.747
	50	0.615	1.379	1.654
(EAF slag, river sand and biochar.)	20	0.371	1.180	1.481
	30	0.380	1.197	1.560
	40	0.377	1.173	1.626
	50	0.372	1.183	1.584
(100% EAF slag)	20	0.696	0.757	0.876
	30	0.706	0.793	0.893
	40	0.709	0.800	0.941
	50	0.712	0.804	0.969
(100% EAF slag and biochar)	20	0.337	0.663	0.856
	30	0.330	0.669	0.856
	40	0.332	0.668	0.877
	50	0.334	0.669	0.861

The data reveals an interesting trend in thermal conductivity in some specimens as a function of temperature. Notably, in some specimens, as the temperature increases, the thermal conductivity of the specimens decreases, with 20°C exhibiting higher conductivity than 50°C.

The results are in line with the results of previous research, in which it was consistently observed that thermal conductivity tends to be higher in specimens with lower porosity. Data analysis indicates that specimens with particle sizes of 0.5 to 1 mm (A) present greater porosity, coinciding with the lowest thermal conductivity among all tested specimens. On the other hand, specimens with particle sizes ranging from 2 to 4 mm, which presented lower porosity, demonstrated greater thermal conductivity [125].

Furthermore, in line with results from previous studies, the introduction of biochar into specimens has been shown to lead to a reduction in thermal conductivity, as is evident from our

analyses. Sample 2B, which contains biochar, demonstrated lower thermal conductivity than sample 1B, without biochar, even though it had lower porosity. This discovery highlights the thermal insulation properties that biochar imparts, regardless of particle size [110].

The values of the thermal transmittance obtained using the bigger specimens and the Test Box equipment are summarised in Table 25.

Table 25: Thermal transmittance according to the Test Box equipment (values in W/m2·K).

	A (0,5 to 1 mm)	C (1 to 2 mm)	B (2 to 4mm)
1 (EAF slag and river sand.)	19.35	27.61	30.14
2 (EAF slag, river sand and biochar.)	18.02	15.49	28.27
3 (100% EAF slag)	18.00	16.59	18.58
4 (100% EAF slag and biochar)	11.17	15.49	13.63

The specimens analyzed in this research have high thermal conductivity and high thermal transmittanc, they have the characteristics of conducting heat more quickly, compared to conventional concrete blocks [126]. The sample that presented the highest value is the sample with EAF-slag, river sand and with a content of 2 to 4 mm (1B).

6.8 Specific heat capacity

The values of the specific heat capacity obtained using the bigger specimens and the Test Box equipment are summarised in table 26.

Table 26: Specific heat capacity according to the Test Box equipment (values in J/kg·K).

	A (0,5 to 1 mm)	C (1 to 2 mm)	B (2 to 4mm)
1 (EAF slag and river sand.)	937	874	923
2 (EAF slag, river sand and biochar.)	891	932	824
3 (100% EAF slag)	897	884	866
4 (100% EAF slag and biochar)	806	1074	839

The sample with the highest thermal capacity was the one with 100% EAF slag, biochar and with a particle size of 1 to 2 mm (4C), the sample has the capacity to absorb a greater amount of heat than the other specimens analyzed. Sample 4C was also the sample that showed the highest CO2 absorption.

6.9 Dynamic thermal response

The dynamic thermal response corresponds to the measurement of temperature and heat flux as a function of time of the specimens when subjected to temperature variation. The values of the delay between the peaks of the top space temperature and the heat flux at the bottom surface (thermal lag) are summarised in Table 27.

Table 27: Thermal lag according to the Test Box equipment (values in hrs).

	A (0,5 to 1 mm)	C (1 to 2 mm)	B (2 to 4mm)
1 (EAF slag and river sand.)	0.49	0.61	0.54
2 (EAF slag, river sand and biochar.)	0.76	0.55	0.61
3 (100% EAF slag)	1.20	1.22	0.61
4 (100% EAF slag and biochar)	1.00	1.06	1.02

Thermal delay measures the delay in the heat wave to propagate from the outer surface (top surface) to the inner surface (bottom surface) of the material. The specimens of 100% EAF slag without biochar and with a particle size of 1 to 2 mm (3C) showed a longer thermal delay time, absorbing and releasing heat more slowly. The sample absorbs heat slowly and releases it slowly, being beneficial for generating energy over a longer period of time, whether due to the material's longer time at high temperature for heating water or the heat difference for thermoelectric energy generators (TEGs).

The values of the thermal stability coefficient of the bigger specimens are summarised in Table 28.

Table 28: Thermal stability coefficient according to the Test Box equipment.

	A (0,5 to 1 mm)	C (1 to 2 mm)	B (2 to 4mm)
1 (EAF slag and river sand.)	0.77	0.87	0.88
2 (EAF slag, river sand and biochar.)	0.80	0.86	0.88
3 (100% EAF slag)	0.77	0.78	0.81
4 (100% EAF slag and biochar)	0.69	0.75	0.74

The analyzed specimens have a high thermal stability value. The sample with 100% EAF, biochar slag with a particle size of 2 to 4 mm (4B) showed greater thermal stability, while the

sample with 100% EAF slag, biochar and particle size of 0.5 to 1 mm (1A) showed a lower stability coefficient thermal.

The material that has high thermal stability is of great importance for the passive solar thermal energy storage, as it has a greater capacity to maintain its mechanical properties such as resistance, tenacity or elasticity at the temperature to which it is subjected.

Chapter 7- Conclusions and recommendations

7.1 Conclusions

This research sought to investigate whether mortars with 100% electric arc furnace slag obtained by accelerated carbonation have ideal microstructure and thermal properties to be used in the construction industry and generate passive solar energy.

Preliminary studies demonstrate DSC results that the thermal behavior of cementitious mixtures is affected by the type of curing process, the composition of the mixture and the presence of slag. The presence of metals such as iron, chromium and manganese in the slag could also affect the formation of new phases and their crystalline structure, as seen in the exothermic peak observed in cement specimens containing these metals.

Furthermore, the DSC results indicate that the heat flux response of the EAF-slag binders was regular and small, indicating that they have suitable thermal properties for passive solar thermal energy storage. The irregular and greater variation in heat flow response of Portland cement-based binders suggests that they may not be as suitable for passive solar energy as EAF slag binders.

Based on the experiments carried out to measure the thermal expansion behavior of EAF slag mortars compared to Portland cement mortars.The results of the experiments showed that the thermal expansion characteristics of EAF slag mortars are superior to those of Portland cement mortars. Specifically, 100% EAF-slag mortars show more than twice the expansion of Portland cement mortars with EAF.

These findings were expected, as the chemical composition of EAF contains a greater quantity of metallic materials and has a darker color, which allows greater heat absorption. Furthermore, the results of the experiments showed that the temperatures of the EAF slag specimens were consistently higher than those of the Portland cement specimens at all times.

Furthermore, specimens with biochar demonstrated reduced thermal conductivity and thermal transmittance compared to specimens without biochar. However, it is important to note that all specimens in this study exhibited higher thermal conductivity than conventional Portland cement specimens.

With comprehensive data analysis, the sample with the best characteristics for the use of passive solar energy in civil construction emerged as the composition of particle sizes ranging from 1 mm to 2 mm containing 100% EAF slag without biochar (3C).

These findings highlight a potential for 100% EAF slag specimens in passive solar thermal applications. Their superior thermal conductivity, substantial thermal capacitance, gradual heat

absorption and heat release characteristics, and resilience to the effects of thermal energy position them as materials that perform well in maintaining mechanical stability even under extreme summer conditions.

Furthermore, this research highlights the feasibility of 100% recycled specimens for construction, offering a sustainable solution that mitigates the environmental impacts associated with waste and conventional energy generation. This study is an important step toward innovative and sustainable civil engineering and construction practices.

7.2 Recommendations

The study of the microstructure and thermal properties of 100% EAF slag mortar produced promising results for its application in the construction industry, particularly in the field of passive solar thermal energy storage. After comprehensive experiments, analysis of results and an understanding of their potential, a compelling case for future research in this domain emerges.

• Investigate potential applications both in new construction projects and in the restoration of existing buildings.

• Explore the use of various industrial waste enriched with metallic materials as raw material to evaluate their thermal efficiency.

• Consider incorporating various additives into mortars to improve their characteristics, particularly those with a high metallic content in their composition.

• Use the same experimental framework to examine the thermal insulation capabilities of different mortars, with the aim of developing efficient thermal insulation materials for the construction industry.

7.3 Summary of publications and conferences

Luciana Sucupira
University of Beira Interior;
Calçada Fonte do Lameiro Edifício II das Engenharias, 6201-001 Covilhã, Portugal
E-mail: Luciana.sucupira.cristino@ubi.pt

7.3.1 Published Articles in International Refereed Journals

1. Luciana Sucupira and João Castro-Gomes,(2021). Review of Energy Harvesting for Buildings Based on Solar Energy and Thermal Materials, CivilEng. https://doi.org/10.3390/civileng2040046.

2. Luciana Sucupira and João Castro-Gomes. Preliminary study of heat flow response of electric-arc furnace slag binders aiming generation of passive solar energy in buildings (The document is under review at Cleaner Engineering and Technology)

3. Luciana Sucupira and João Castro-Gomes, (2024). Thermal Expansion/Energy Storage Characteristics of EAF-Slag Mortars for Passive Solar Energy. In: Lanzinha, J.C.G., Qualharini, E.L. (eds) Proceedings of CIRMARE 2023. CIRMARE 2023. Lecture Notes in Civil Engineering, vol 444. Springer, Cham.
https://doi.org/10.1007/978-3-031-48461-2_19

4. Luciana Sucupira, Gabriel Zsembinszki, Sara Risco Amigó, João Castro-Gomes and Luisa F. Cabeza. Thermal properties and porosities of 100% electric arc furnace-slag mortars for passive solar energy applications in the construction industry.
(The document is under review at Construction and Building Materials)

The complete articles are in the annex

References

[1] H. Du, P. Huang, P. Jones, Modular facade retrofit with renewable energy technologies: The definition and current status in Europe, Energy Build. 205 (2019). https://doi.org/10.1016/j.enbuild.2019.109543.

[2] European Commission, 2030 Climate & Energy Framework, 2014. https://doi.org/10.1007/s13398-014-0173-7.2.

[3] República Portuguesa, Plano Nacional Integrado Energia e Clima 2021-2030, (2018) 1–11.

[4] H. Haarstad, M.W. Wathne, Are smart city projects catalyzing urban energy sustainability?, Energy Policy. 129 (2019) 918–925. https://doi.org/10.1016/j.enpol.2019.03.001.

[5] M. Gholikhani, H. Roshani, S. Dessouky, A.T. Papagiannakis, A critical review of roadway energy harvesting technologies, Appl. Energy. 261 (2020) 114388. https://doi.org/10.1016/j.apenergy.2019.114388.

[6] H. Wang, A. Jasim, X. Chen, Energy harvesting technologies in roadway and bridge for different applications – A comprehensive review, Appl. Energy. 212 (2018) 1083–1094. https://doi.org/10.1016/j.apenergy.2017.12.125.

[7] M. Shen, Z. Hu, Y. Qiu, S. Qiu, M. yu Li, G. Zhang, S. Zhang, Z. Yang, F. Kagawa, S. Jiang, Thermal energy harvesting performance in 0.94Bi0.5Na0.5TiO3-0.06BaZr0.2Ti0.8O3: AlN composite ceramics based on the Olsen cycle, J. Eur. Ceram. Soc. 39 (2019) 5243–5251. https://doi.org/10.1016/j.jeurceramsoc.2019.09.003.

[8] iberdrola, WHAT PHOTOVOLTAIC ENERGY IS, Iberdrola. (2021). https://www.iberdrola.com/environment/what-is-photovoltaic-energy (accessed February 4, 2021).

[9] J. Duan, Y. Zhao, B. He, Q. Tang, Efficiency enhancement of bifacial dye-sensitized solar cells through bi-tandem carbon quantum dots tailored transparent counter electrodes, Electrochim. Acta. 278 (2018) 204–209. https://doi.org/10.1016/j.electacta.2018.05.057.

[10] Y. Cai, Z. Guo, Spectral investigation of solar energy absorption and light transmittance in a water-filled prismatic glass louver, Sol. Energy. 179 (2019) 164–173. https://doi.org/10.1016/j.solener.2018.12.066.

[11] C. Wang, S. Yu, X. Guo, T. Kearney, P. Guo, R. Chang, J. Chen, W. Chen, C. Sun, Maximizing Solar Energy Utilization through Multicriteria Pareto Optimization of Energy Harvesting and Regulating Smart Windows, Cell Reports Phys. Sci. 1 (2020) 100108. https://doi.org/10.1016/j.xcrp.2020.100108.

[12] T. Liu, Y. Zhao, J. Duan, B. He, J. Zheng, Q. Tang, Transparent ternary alloy counter electrodes for high-efficiency bifacial dye-sensitized solar cells, Sol. Energy. 170 (2018) 762–768. https://doi.org/10.1016/j.solener.2018.06.037.

[13] M. Alva, A. Vlachokostas, N. Madamopoulos, Experimental demonstration and performance evaluation of a complex fenestration system for daylighting and thermal harvesting, Sol. Energy. 197 (2020) 385–395. https://doi.org/10.1016/j.solener.2020.01.012.

[14] Y. Dai, Y. Bai, Performance improvement for building integrated photovoltaics in practice: A review, Energies. 14 (2021). https://doi.org/10.3390/en14010178.

[15] Q. Lin, Y. Zhang, A. Van Mieghem, Y.C. Chen, N. Yu, Y. Yang, H. Yin, Design and experiment of a sun-powered smart building envelope with automatic control, Energy Build. 223 (2020) 110173. https://doi.org/10.1016/j.enbuild.2020.110173.

[16] W.T. Sheikh, Q. Asghar, Adaptive biomimetic facades: Enhancing energy efficiency of highly glazed buildings, Front. Archit. Res. 8 (2019) 319–331. https://doi.org/10.1016/j.foar.2019.06.001.

[17] M. Talaei, M. Mahdavinejad, R. Azari, Thermal and Energy Performance of Algae Bioreactive Façades : A Review, J. Build. Eng. 28 (2019) 101011. https://doi.org/10.1016/j.jobe.2019.101011.

[18] V.S. Romero, Fachada biosensible, Arquitecturayempresa. (2015). https://www.arquitecturayempresa.es/noticia/fachada-biosensible (accessed December 4, 2019).

[19] J. Bartolacci, Why Building Facades Are the Future of Clean Energy Farms, Architizer. (2019). https://architizer.com/blog/inspiration/stories/energy-harvesting-facades/ (accessed December 4, 2019).

[20] Voltimum, Edifício Solar XXI – Edifício energeticamente eficiente, (n.d.). https://www.voltimum.pt/artigos/noticias-do-sector/edificio-solar-xxi (accessed December 5, 2019).

[21] Construible, Investigadores alemanes diseñan fachadas solares que aportan un 50% más de energía que otros sistemas, Construible. (n.d.). https://www.construible.es/2020/03/17/investigadores-alemanes-disenan-fachadas-

solares-aportan-50-energia-edificio#.XnDC553epPI.email (accessed April 22, 2020).

[22] M. Shen, Z. Hu, Y. Qiu, S. Qiu, M. Li, G. Zhang, Thermal energy harvesting performance in 0.94Bi0.5Na0.5TiO3- 0.06BaZr0.2Ti0.8O3: AlN composite ceramics based on the Olsen cycle, J. Eur. Ceram. Soc. 39 (2019) 5243–5251. https://doi.org/10.1016/j.jeurceramsoc.2019.09.003.

[23] Q. Wang, C.R. Bowen, R. Lewis, J. Chen, W. Lei, H. Zhang, M.Y. Li, S. Jiang, Hexagonal boron nitride nanosheets doped pyroelectric ceramic composite for high-performance thermal energy harvesting, Nano Energy. 60 (2019) 144–152. https://doi.org/10.1016/j.nanoen.2019.03.037.

[24] D. V. Bellas, E. Lidorikis, Design of high-temperature solar-selective coatings for application in solar collectors, Sol. Energy Mater. Sol. Cells. 170 (2017) 102–113. https://doi.org/10.1016/j.solmat.2017.05.056.

[25] B.B. Bohara, A.K. Batra, Development of multi-functional nano-paint for energy harvesting applications, Prog. Nat. Sci. Mater. Int. 28 (2018) 1–6. https://doi.org/10.1016/j.pnsc.2018.01.005.

[26] J. Silva-Leon, A. Cioncolini, M.R.A. Nabawy, A. Revell, A. Kennaugh, Simultaneous wind and solar energy harvesting with inverted flags, Appl. Energy. 239 (2019) 846–858. https://doi.org/10.1016/j.apenergy.2019.01.246.

[27] H. Jia, X. Cheng, J. Zhu, Z. Li, J. Guo, Mathematical and experimental analysis on solar thermal energy harvesting performance of the textile-based solar thermal energy collector, Renew. Energy. 129 (2018) 553–560. https://doi.org/10.1016/j.renene.2018.05.097.

[28] A. Gagliano, S. Aneli, F. Nocera, Analysis of the performance of a building solar thermal facade (BSTF)for domestic hot water production, Renew. Energy. 142 (2019) 511–526. https://doi.org/10.1016/j.renene.2019.04.102.

[29] M. Velho, Empresa portuguesa quer pôr painéis solares térmicos nas fachadas de edifícios, Dinheirovivo. (2019). https://www.dinheirovivo.pt/fazedores/empresa-portuguesa-quer-por-paineis-solares-termicos-nas-fachadas-de-edificios/ (accessed December 5, 2019).

[30] Atsolar, O PRIMEIRO PAINEL SOLAR TÉRMICO QUE FAZ TUDO, (2019). https://atsolar.pt/pt/senergy-force-pt/ (accessed December 5, 2019).

[31] E.D. Rounis, A. Athienitis, T. Stathopoulos, Review of air-based PV/T and BIPV/T systems - Performance and modelling, Renew. Energy. 163 (2021) 1729–1753. https://doi.org/10.1016/j.renene.2020.10.085.

[32] Z. Nagy, B. Svetozarevic, P. Jayathissa, M. Begle, J. Hofer, G. Lydon, A. Willmann, A. Schlueter, The Adaptive Solar Facade: From concept to prototypes, Front. Archit. Res. 5 (2016) 143–156. https://doi.org/10.1016/j.foar.2016.03.002.

[33] S. Freitas, M.C. Brito, Solar façades for future cities, Renew. Energy Focus. 31 (2019) 73–79. https://doi.org/10.1016/j.ref.2019.09.002.

[34] T. Zhang, M. Wang, H. Yang, A review of the energy performance and life-cycle assessment of building-integrated photovoltaic (BIPV) systems, Energies. 11 (2018). https://doi.org/10.3390/en11113157.

[35] T. Matuska, Simulation study of building integrated solar liquid PV-T collectors, Int. J. Photoenergy. 2012 (2012). https://doi.org/10.1155/2012/686393.

[36] J. Zhang, L. Xu, V. Shabunko, S.E.R. Tay, H. Sun, S.S.Y. Lau, T. Reindl, Impact of urban block typology on building solar potential and energy use efficiency in tropical high-density city, Appl. Energy. 240 (2019) 513–533. https://doi.org/10.1016/j.apenergy.2019.02.033.

[37] H. Xiao, Z. Chen, K. Sun, C. Yan, J. Xiao, L. Jiang, X. Hao, Sol-gel solution-processed Cu 2 SrSnS 4 thin films for solar energy harvesting, Thin Solid Films. 697 (2020) 137828. https://doi.org/10.1016/j.tsf.2020.137828.

[38] K. Kuo, M. Liao, J. Wang, Y. Lee, C. Huang, C. Chou, C. Liu, H. Hsu, P. Chen, Comprehensive assessment of the long-term energy harvest capabilities for PV systems with di ff erent tilt angles : Case study in Taiwan, Renew. Sustain. Energy Rev. 97 (2018) 74–89. https://doi.org/10.1016/j.rser.2018.08.024.

[39] S. Lamichhane, S. Sharma, M. Tomar, V. Gupta, Effect of laser fluence on multiferroic BiFeO3 ferroelectric photovoltaic cells, J. Phys. Chem. Solids. 146 (2020) 109602. https://doi.org/10.1016/j.jpcs.2020.109602.

[40] R.I.S. Pereira, M.M. Camboim, A.W.R. Villarim, C.P. Souza, S.C.S. Jucá, P.C.M. Carvalho, On harvesting residual thermal energy from photovoltaic module back surface, AEU - Int. J. Electron. Commun. 111 (2019) 152878. https://doi.org/10.1016/j.aeue.2019.152878.

[41] H. Fathabadi, Solar energy harvesting in buildings using a proposed novel electrochemical device as an alternative to PV modules, Renew. Energy. 133 (2019) 118–125. https://doi.org/10.1016/j.renene.2018.10.010.

[42] Y. Cai, L. Wang, W.W. Wang, D. Liu, F.Y. Zhao, Solar energy harvesting potential of a photovoltaic-thermoelectric cooling and power generation system: Bidirectional modeling and performance optimization, J. Clean. Prod. 254 (2020) 120150.

https://doi.org/10.1016/j.jclepro.2020.120150.

[43] H. Sharma, A. Haque, Z.A. Jaffery, Maximization of wireless sensor network lifetime using solar energy harvesting for smart agriculture monitoring, Ad Hoc Networks. 94 (2019) 101966. https://doi.org/10.1016/j.adhoc.2019.101966.

[44] H. Jafari Mosleh, R. Ahmadi, Linear parabolic trough solar power plant assisted with latent thermal energy storage system: A dynamic simulation, Appl. Therm. Eng. 161 (2019) 114204. https://doi.org/10.1016/j.applthermaleng.2019.114204.

[45] Y.S. Byon, J.W. Jeong, Phase change material-integrated thermoelectric energy harvesting block as an independent power source for sensors in buildings, Renew. Sustain. Energy Rev. 128 (2020) 109921. https://doi.org/10.1016/j.rser.2020.109921.

[46] Y. Jeyashree, Y. Sukhi, A. Vimala Juliet, S. Lourdu Jame, S. Indirani, Concentrated solar thermal energy harvesting using Bi2Te3based thermoelectric generator, Mater. Sci. Semicond. Process. 107 (2020) 104782. https://doi.org/10.1016/j.mssp.2019.104782.

[47] S. Ghosh, S. Harish, M. Ohtaki, B.B. Saha, Enhanced figure of merit of cement composites with graphene and ZnO nanoinclusions for efficient energy harvesting in buildings, Energy. 198 (2020) 117396. https://doi.org/10.1016/j.energy.2020.117396.

[48] S. Ghosh, S. Harish, K.A. Rocky, M. Ohtaki, B.B. Saha, Graphene enhanced thermoelectric properties of cement based composites for building energy harvesting, Energy Build. 202 (2019) 1–7. https://doi.org/10.1016/j.enbuild.2019.109419.

[49] J. Wei, L. Zhao, Q. Zhang, Z. Nie, L. Hao, Enhanced thermoelectric properties of cement-based composites with expanded graphite for climate adaptation and large-scale energy harvesting, Energy Build. 159 (2018) 66–74. https://doi.org/10.1016/j.enbuild.2017.10.032.

[50] and P.S. Małgorzata Krystek, Dawid Pakulski, Violetta Patroniak, Marcin Górski, Leszek Szojda, Artur Ciesielski, High-Performance Graphene-Based Cementitious Composites, Adv. Sci. (2019).

[51] R. O'Hegarty, O. Kinnane, S.J. McCormack, Parametric investigation of concrete solar collectors for façade integration, Sol. Energy. 153 (2017) 396–413. https://doi.org/10.1016/j.solener.2017.05.092.

[52] X. Liao, Y. Liu, J. Ren, L. Guan, X. Sang, Investigation of a double-PCM-based thermoelectric energy- harvesting device using temperature fl uctuations in an ambient environment, Energy. 202 (2020) 117724. https://doi.org/10.1016/j.energy.2020.117724.

[53] N. Chen, H. Ma, Y. Li, J. Cheng, C. Zhang, D. Wu, H. Zhu, Complementary optical

absorption and enhanced solar thermal conversion of CuO-ATO nanofluids, Sol. Energy Mater. Sol. Cells. 162 (2017) 83–92. https://doi.org/10.1016/j.solmat.2016.12.049.

[54] V. Bhalla, H. Tyagi, Solar energy harvesting by cobalt oxide nanoparticles, a nanofluid absorption based system, Sustain. Energy Technol. Assessments. 24 (2017) 45–54. https://doi.org/10.1016/j.seta.2017.01.011.

[55] S. Wu, G. Xiong, H. Yang, Y. Tian, B. Gong, H. Wan, Y. Wang, T.S. Fisher, J. Yan, K. Cen, Z. Bo, K. (Ken) Ostrikov, Scalable Production of Integrated Graphene Nanoarchitectures for Ultrafast Solar-Thermal Conversion and Vapor Generation, Matter. 1 (2019) 1017–1032. https://doi.org/10.1016/j.matt.2019.06.010.

[56] X. Li, J. Zhang, B. Fu, C. Song, W. Shang, P. Tao, T. Deng, Erythritol impregnated within surface-roughened hydrophilic metal foam for medium-temperature solar-thermal energy harvesting, Energy Convers. Manag. 222 (2020) 113241. https://doi.org/10.1016/j.enconman.2020.113241.

[57] J. Norambuena-Contreras, J.L. Concha, R. Borinaga-Treviño, Evaluation of the thermophysical and heating properties of a composite rubber membrane with energy harvesting purposes, Polym. Test. 64 (2017) 145–155. https://doi.org/10.1016/j.polymertesting.2017.09.042.

[58] W. Jiang, D. Yuan, S. Xu, H. Hu, J. Xiao, A. Sha, Y. Huang, Energy harvesting from asphalt pavement using thermoelectric technology, Appl. Energy. 205 (2017) 941–950. https://doi.org/10.1016/j.apenergy.2017.08.091.

[59] N. Zabihi, M. Saafi, Recent developments in the energy harvesting systems from road infrastructures, Sustain. 12 (2020). https://doi.org/10.3390/SU12176738.

[60] S.A. Tahami, M. Gholikhani, R. Nasouri, S. Dessouky, A.T. Papagiannakis, Developing a new thermoelectric approach for energy harvesting from asphalt pavements, Appl. Energy. 238 (2019) 786–795. https://doi.org/10.1016/j.apenergy.2019.01.152.

[61] X. Zhu, Y. Yu, F. Li, A review on thermoelectric energy harvesting from asphalt pavement: Configuration, performance and future, Constr. Build. Mater. 228 (2019) 116818. https://doi.org/10.1016/j.conbuildmat.2019.116818.

[62] Y. Wang, Z. Rao, J. Liu, S. Liao, An optimized control strategy for integrated solar and air-source heat pump water heating system with cascade storage tanks, Energy Build. 210 (2020) 109766. https://doi.org/10.1016/j.enbuild.2020.109766.

[63] M.S. Hasebe M, Kamikawa Y, Thermoelectric generators using solar thermal energy in heated road pavement, 2006 ICT'06 25th international conference on. IEEE, 2006.

[64] Y. Zhou, S. Zhang, X. Xu, W. Liu, S. Zhang, G. Li, J. He, Dynamic piezo-thermoelectric generator for simultaneously harvesting mechanical and thermal energies, Nano Energy. 69 (2020) 104397. https://doi.org/10.1016/j.nanoen.2019.104397.

[65] T.H. Kwan, X. Wu, Q. Yao, Complete implementation of the combined TEG-TEC temperature control and energy harvesting system, Control Eng. Pract. 95 (2020) 104224. https://doi.org/10.1016/j.conengprac.2019.104224.

[66] A. Chiarelli, A. Al-Mohammedawi, A.R. Dawson, A. García, Construction and configuration of convection-powered asphalt solar collectors for the reduction of urban temperatures, Int. J. Therm. Sci. 112 (2017) 242. https://doi.org/10.1016/j.ijthermalsci.2016.10.012.

[67] V. Bobes-Jesus, P. Pascual-Muñoz, D. Castro-Fresno, J. Rodriguez-Hernandez, Asphalt solar collectors: A literature review, Appl. Energy. 102 (2013) 962–970. https://doi.org/10.1016/j.apenergy.2012.08.050.

[68] S.K. Verma, N.K. Gupta, D. Rakshit, A comprehensive analysis on advances in application of solar collectors considering design, process and working fluid parameters for solar to thermal conversion, Sol. Energy. 208 (2020) 1114–1150. https://doi.org/10.1016/j.solener.2020.08.042.

[69] J. Johnsson, B. Adl-Zarrabi, A numerical and experimental study of a pavement solar collector for the northern hemisphere, Appl. Energy. 260 (2020) 114286. https://doi.org/10.1016/j.apenergy.2019.114286.

[70] R.B. Mallick, B.L. Chen, S. Bhowmick, Harvesting energy from asphalt pavements and reducing the heat island effect, Int. J. Sustain. Eng. 2 (2009) 214–228. https://doi.org/10.1080/19397030903121950.

[71] R. Mirzanamadi, C.E. Hagentoft, P. Johansson, Numerical investigation of harvesting solar energy and anti-icing road surfaces using a hydronic heating pavement and borehole thermal energy storage, Energies. 11 (2018) 1–23. https://doi.org/10.3390/en11123443.

[72] S.A. Tahami, M. Gholikhani, R. Nasouri, S. Dessouky, A.T. Papagiannakis, Developing a new thermoelectric approach for energy harvesting from asphalt pavements, Appl. Energy. 238 (2019) 786–795. https://doi.org/10.1016/j.apenergy.2019.01.152.

[73] I. Sarbu, C. Sebarchievici, A comprehensive review of thermal energy storage, Sustain. 10 (2018). https://doi.org/10.3390/su10010191.

[74] I. (International R.E. Agency), Innovation Outlook: Thermal Energy Storage., (2020). https://www.irena.org/.

[75] Y. Cui, R. Gulfam, Y. Ishrat, S. Iqbal, F. Yao, Recent Progress of Phase Change Materials and Their Applications in Facility Agriculture and Related-Buildings — A Review, (2024) 1–25.

[76] apren, Production, (2021). https://www.apren.pt/en/renewable-energies/production/.

[77] D. Kannan, Role of multiple stakeholders and the critical success factor theory for the sustainable supplier selection process, Int. J. Prod. Econ. 195 (2018) 391–418. https://doi.org/10.1016/j.ijpe.2017.02.020.

[78] P.S. Humbert, J. Castro-Gomes, CO2 activated steel slag-based materials: A review, J. Clean. Prod. 208 (2019) 448–457. https://doi.org/10.1016/j.jclepro.2018.10.058.

[79] Eurostat, Greenhouse gas emission statistics - emission inventories, (n.d.).

[80] L. Huang, G. Krigsvoll, F. Johansen, Y. Liu, X. Zhang, Carbon emission of global construction sector, Renew. Sustain. Energy Rev. 81 (2018) 1906–1916. https://doi.org/10.1016/j.rser.2017.06.001.

[81] Eurostat, Waste statistics, Eurostat- Stat. (n.d.). https://ec.europa.eu/eurostat/statistics-explained/index.php?title=Waste_statistics#Further_Eurostat_information (accessed November 11, 2021).

[82] M. Abdullahi, J.O. Odigure, A.S. Kovo, A.S. Abdulkareem, Characterization and predictive reaction model for cement-sand-kaolin composite for CO2 sequestration, J. CO2 Util. 16 (2016) 169–181. https://doi.org/10.1016/j.jcou.2016.06.008.

[83] P.S. Humbert, Synthesis and Characterisation of CO 2 Activated Binders and Concretes using Industrial Wastes for Precast Buildings Applications, (2020).

[84] P.S. Humbert, J.P. Castro-Gomes, H. Savastano, Clinker-free CO 2 cured steel slag based binder: Optimal conditions and potential applications, Constr. Build. Mater. 210 (2019) 413–421. https://doi.org/10.1016/j.conbuildmat.2019.03.169.

[85] H. Oliveira, Grande Entrevista Administrador da Fundínio João Meireles CONTRIBUIÇÕES TÉCNICAS Os Desafios da Mobilidade Fundição de Precisão por Modelo Perdido de Ligas de Magnésio em Moldação Cerâmica : Influência do Revestimento dos Modelos Reutilização de Escórias , (n.d.).

[86] J. Waligora, D. Bulteel, P. Degrugilliers, D. Damidot, J.L. Potdevin, M. Measson, Chemical and mineralogical characterizations of LD converter steel slags: A multi-analytical techniques approach, Mater. Charact. 61 (2010) 39–48. https://doi.org/10.1016/j.matchar.2009.10.004.

[87] M.P. Luxán, R. Sotolongo, F. Dorrego, E. Herrero, Characteristics of the slags produced in the fusion of scrap steel by electric arc furnace, Cem. Concr. Res. 30 (2000) 517–519. https://doi.org/10.1016/S0008-8846(99)00253-7.

[88] M. Tossavainen, F. Engstrom, Q. Yang, N. Menad, M. Lidstrom Larsson, B. Bjorkman, Characteristics of steel slag under different cooling conditions, Waste Manag. 27 (2007) 1335–1344. https://doi.org/10.1016/j.wasman.2006.08.002.

[89] P. Nielsen, M.A. Boone, L. Horckmans, R. Snellings, M. Quaghebeur, Accelerated carbonation of steel slag monoliths at low CO2 pressure - Microstructure and strength development, J. CO2 Util. 36 (2020) 124–134. https://doi.org/10.1016/j.jcou.2019.10.022.

[90] D. Höllen, I. Berneder, F. Capo Tous, M. Stöllner, K. Philipp Sedlazeck, T. Schwarz, A. Aldrian, M. Lehner, Stepwise treatment of ashes and slags by dissolution, precipitation of iron phases and carbonate precipitation for production of raw materials for industrial applications, Waste Manag. 78 (2018) 750–762. https://doi.org/10.1016/j.wasman.2018.06.048.

[91] D.Z. C. Le Quéré , RM Andrew , P. Friedlingstein , S. Sitch , J. Pongratz , AC Manning , JI Korsbakken , GP Peters , JG Canadell , RB Jackson , TA Boden , PP Tans , OD Andrews , VK Arora , DCE Bakker , L. Barbero , M. Becker, RA Betts , L. Bopp , F. Chevallier, Global Carbon Budget 2017, Earth Syst. Sci. (2018) 405–448. https://essd.copernicus.org/articles/10/405/2018/.

[92] F. Nocito, A. Dibenedetto, Atmospheric CO2 mitigation technologies: carbon capture utilization and storage, Curr. Opin. Green Sustain. Chem. 21 (2020) 34–43. https://doi.org/10.1016/j.cogsc.2019.10.002.

[93] I. Ghiat, T. Al-Ansari, A review of carbon capture and utilisation as a CO2abatement opportunity within the EWF nexus, J. CO2 Util. 45 (2021) 101432. https://doi.org/10.1016/j.jcou.2020.101432.

[94] E. Alper, O. Yuksel Orhan, CO2 utilization: Developments in conversion processes, Petroleum. 3 (2017) 109–126. https://doi.org/10.1016/j.petlm.2016.11.003.

[95] R.M. Cuéllar-Franca, A. Azapagic, Carbon capture, storage and utilisation technologies: A critical analysis and comparison of their life cycle environmental impacts, J. CO2 Util. 9 (2015) 82–102. https://doi.org/10.1016/j.jcou.2014.12.001.

[96] WardaAshraf, Carbonation of cement-based materials: Challenges and opportunities, Construction and Building Materials, 2016.

[97] K.L. Scrivener, V.M. John, E.M. Gartner, Eco-efficient cements: Potential economically

viable solutions for a low-CO2 cement-based materials industry, Cem. Concr. Res. 114 (2018) 2–26. https://doi.org/10.1016/j.cemconres.2018.03.015.

[98] A. Di Maria, R. Snellings, L. Alaert, M. Quaghebeur, K. Van Acker, Environmental assessment of CO2 mineralisation for sustainable construction materials, Int. J. Greenh. Gas Control. 93 (2020) 102882. https://doi.org/10.1016/j.ijggc.2019.102882.

[99] J.G. Jang, G.M. Kim, H.J. Kim, H.K. Lee, Review on recent advances in CO2 utilization and sequestration technologies in cement-based materials, Constr. Build. Mater. 127 (2016) 762–773. https://doi.org/10.1016/j.conbuildmat.2016.10.017.

[100] P. Nielsen, M.A. Boone, L. Horckmans, R. Snellings, M. Quaghebeur, Accelerated carbonation of steel slag monoliths at low CO2 pressure - Microstructure and strength development, J. CO2 Util. 36 (2020) 124–134. https://doi.org/10.1016/j.jcou.2019.10.022.

[101] L.S. Cristino, E. Civil, Materiais produzidos com cimento reciclado e RCD por carbonatação acelerada, (2021).

[102] Carbicrete, (2023). https://carbicrete.com/ (accessed February 3, 2024).

[103] CO2ncrEAT: Cement-free building products with negative carbon footprints by using CO2 gas and by- product from respectively Lime and stainless steel plants, (n.d.).

[104] Be.redaction, Planet Future, CO2ncrEAT Un Proj. Circ. Unique En Son Genre. (2022). https://fr.planet-future.be/innovation/co2ncreat-un-projet-circulaire-unique-en-son-genre/# (accessed February 11, 2024).

[105] Challenge zero, Carbon Negat. Concr. “CO2 SUICOM.” (n.d.). https://www.challenge-zero.jp/en/casestudy/616.

[106] Biohm, (2016). https://www.biohm.co.uk/mycelium (accessed February 3, 2024).

[107] M. Carbon, Mineral carbonation, (2023). https://www.mineralcarbonation.com/ (accessed February 3, 2024).

[108] D. Sher, MIRRECO promises to store CO2 in CAST® 3D printed hemp houses, Voxelmatters. (n.d.). https://www.voxelmatters.com/mirreco-promises-they-can-store-co2-in-cast-3d-printed-hempcrete-houses/ (accessed February 3, 2024).

[109] N. Sedira, J. Castro-Gomes, Effects of EAF-Slag on alkali-activation of tungsten mining waste: mechanical properties, MATEC Web Conf. 274 (2019) 01003. https://doi.org/10.1051/matecconf/201927401003.

[110] P.K. Gunasekaran, S. Choo, Performance of bamboo biochar as partial cement

replacement in mortar, Mater. Today Proc. (2023). https://doi.org/10.1016/j.matpr.2023.06.322.

[111] A. Sirico, P. Bernardi, C. Sciancalepore, F. Vecchi, A. Malcevschi, B. Belletti, D. Milanese, Biochar from wood waste as additive for structural concrete, Constr. Build. Mater. 303 (2021) 124500. https://doi.org/10.1016/j.conbuildmat.2021.124500.

[112] L. Ye, J. Zhang, J. Zhao, Z. Luo, S. Tu, Y. Yin, Properties of biochar obtained from pyrolysis of bamboo shoot shell, J. Anal. Appl. Pyrolysis. 114 (2015) 172–178. https://doi.org/10.1016/j.jaap.2015.05.016.

[113] H. Maljaee, R. Madadi, H. Paiva, L. Tarelho, V.M. Ferreira, Incorporation of biochar in cementitious materials: A roadmap of biochar selection, Constr. Build. Mater. 283 (2021) 122757. https://doi.org/10.1016/j.conbuildmat.2021.122757.

[114] M. Kheradmand, M. Azenha, J.L.B. De Aguiar, K.J. Krakowiak, Thermal behavior of cement based plastering mortar containing hybrid microencapsulated phase change materials, Energy Build. 84 (2014) 526–536. https://doi.org/10.1016/j.enbuild.2014.08.010.

[115] B. Xu, Z. Li, Paraffin/diatomite composite phase change material incorporated cement-based composite for thermal energy storage, Appl. Energy. 105 (2013) 229–237. https://doi.org/10.1016/j.apenergy.2013.01.005.

[116] NP EN 206-1, Betão - Parte 1: Especificação, desempenho, produção e conformidade, Concrete. (2007).

[117] W. Deboucha, N. Leklou, A. Khelidj, M.N. Oudjit, Hydration development of mineral additives blended cement using thermogravimetric analysis (TGA): Methodology of calculating the degree of hydration, Constr. Build. Mater. 146 (2017) 687–701. https://doi.org/10.1016/j.conbuildmat.2017.04.132.

[118] M.S. Kim, Y. Jun, C. Lee, J.E. Oh, Use of CaO as an activator for producing a price-competitive non-cement structural binder using ground granulated blast furnace slag, Cem. Concr. Res. 54 (2013) 208–214. https://doi.org/10.1016/j.cemconres.2013.09.011.

[119] G.H.D. Tonoli, G.F. Carmello, C.A. Fioroni, T. de L. Pereira, G. Rocha, R.B. de Souza, V.M. John, H. Savastano, Influence of the initial moisture content on the carbonation degree and performance of fiber-cement composites, Constr. Build. Mater. 215 (2019) 22–29. https://doi.org/10.1016/j.conbuildmat.2019.04.159.

[120] I. Leber, F.A. Blakey, Acción del anhídrido carbónico sobre los morteros y el hormigón; Some effects of carbon dioxide on mortars and concrete, 7 (1957) 0–1.

[121] C. Barreneche, M.E. Navarro, A.I. Fernández, L.F. Cabeza, Improvement of the thermal inertia of building materials incorporating PCM. Evaluation in the macroscale, Appl. Energy. 109 (2013) 428–432. https://doi.org/10.1016/j.apenergy.2012.12.055.

[122] D.H. Everett, L. Butterworths, International union of pure and applied chemistry division of physical chemistry. Manual of symbols and terminology for physicochemical quantities and units . Appendix II: Definitions, Terminology and Symbols in Colloid and Surface Chemistry PART I, (1972) 579–638.

[123] D.N. Huntzinger, J.S. Gierke, S.K. Kawatra, T.C. Eisele, L.L. Sutter, Carbon dioxide sequestration in cement kiln dust through mineral carbonation, Environ. Sci. Technol. 43 (2009) 1986–1992. https://doi.org/10.1021/es802910z.

[124] M. Chromá, D. Vo, P. Bayer, Concrete Rehydration after Heating to Temperatures of up to 1200 ° C, Int. Conf. Durab. Build. Mater. Components. (2011) 1633–1639. http://www.irbnet.de/daten/iconda/CIB22528.pdf.

[125] I. Asadi, P. Shafigh, Z.F. Bin Abu Hassan, N.B. Mahyuddin, Thermal conductivity of concrete – A review, J. Build. Eng. 20 (2018) 81–93. https://doi.org/10.1016/j.jobe.2018.07.002.

[126] P. Shafigh, I. Asadi, N.B. Mahyuddin, Concrete as a thermal mass material for building applications - A review, J. Build. Eng. 19 (2018) 14–25. https://doi.org/10.1016/j.jobe.2018.04.021.